Investigation of effect of deposition parameters on composition, structure, and properties of plasma deposited boron carbide thin films

By

Arundhati Bute

(PHYS 01201504007)

Homi Bhabha National Institute, Mumbai
Constituent Institution: Bhabha Atomic Research Centre

A thesis submitted to the
Board of Studies in Physical Sciences

In partial fulfillment of requirements
For the Degree of

DOCTOR OF PHILOSOPHY
of
HOMI BHABHA NATIONAL INSTITUTE

October, 2020

STATEMENT BY AUTHOR

This dissertation has been submitted in partial fulfillment of requirements for an advanced degree at Homi Bhabha National Institute (HBNI), and is deposited in the Library to be made available to borrowers under rules of the HBNI.

Brief quotations from this dissertation are allowable without special permission, provided that accurate acknowledgement of source is made. Requests for permission for extended quotation from or reproduction of this manuscript in whole or in part may be granted by the Competent Authority of HBNI when in his or her judgment the proposed use of the material is in the interests of scholarship. In all other instances, however, permission must be obtained from the author.

(Arundhati Bute)

List of Publications arising from the thesis

Journal:

1. "Effect of self-bias on the elemental composition and neutron absorption of boron carbide films deposited by RF plasma enhanced CVD", **A. Bute**, Jagannath, R. Kar, S.S. Chopade, S.S. Desai, M.N. Deo, PrittyRao, N. Chand, S. Kumar, K.Singh, D.S. Patil, S. Sinha, ***Materials Chemistry and Physics*, 2016, *Vol. 182, 62-71***.

2. Composition Dependent Microstructure and Optical Properties of Boron Carbide (B_xC) Thin Films Deposited by Radio Frequency-Plasma Enhanced Chemical Vapor Deposition Technique, **A. Bute**, S. Jena, D. Bhattacharya, S. Kumar, N. Chand, N. Keskar and S. Sinha, ***Materials Research Bulletin*, 2019, *Vol. 109 175–182.***

3. Tribological properties of hydrogenated boron carbide (B_xC: H_y) thin films on stainless steel deposited by RF-PECVD technique, **Arundhati Bute**, Neelima Khare, Sanjiv Kumar, Debarati Bhattacharya, Kulwant Singh, Ashok Kumar Sahu, Namita Maiti, Naresh Chand and Sucharita Sinha, ***The European Physical Journal Applied Physics, 2020, Vol. 91(2), 21301.***

4. Comparative study of structure, optical properties and residual stress of boron carbide thin films deposited by RF-PECVD and PLD technique, **A. Bute**, S. Jena, S. Kedia, D.V. Udupa, K. Singh, D. Bhattacharya, M. H. Modi, N. Maiti, N. Chand and S. Sinha, ***Materials Chemistry and Physics 258 (2021) 123860.***

Conferences:

1. Variation of Elemental Composition in Boron Carbide Coatings with RF Self-Bias During Deposition by RF PECVD, **A. Bute**, Jagannath, M.N. Deo, Pritty Rao, D.S. Patil, S. Sinha, 30th National Symposium on Plasma Science & Technology (PLASMA 2015), December, 2015, Saha Institute For Nuclear Physics (SINP) Kolkata.

2. Optical Properties of RF-PECVD Deposited Boron Carbide films: Dependence on RF Self-Bias, **Arundhati Bute**, Shuvendu Jena, Naresh Chand, Sucharita Sinha, 31st National Symposium on Plasma Science & Technology (PLASMA 2016), December, 2016, Bharathiar University, Coimbatore.

Others: NA

(Arundhati Bute)

Dedicated to my parents,

Mr. Nibaran Chandra Bute,

Mrs. Shanti Rani Bute and

My brother Rakesh, My husband Biplab,

and my baby girl Aarin

ACKNOWLEDGEMENTS

This work would not be possible without the constant encouragement and support from many wonderful people. I therefore take this opportunity to extend my sincere thanks and gratitude towards them. However, there is a possibility that I might unintentionally miss to mention each and every person who has helped me in some way or other during the course of my Ph.D. I sincerely apologize to them in advance.

First and foremost, I would like to express my honest and sincere gratitude to my guide Dr. Sucharita Sinha for her continuous motivation, support, patience, and invaluable suggestions. Her guidance helped me in all the time of research and writing of this thesis.

Beside my guide, I would also like to express my deepest appreciation to Dr. D.S. Patil, my very first mentor who introduced me to the field of plasma material processing and is also a member of my doctoral committee.

I would like to convey my thanks to the other doctoral committee members: Dr. Saibal Basu, Dr. Dinesh V Udupa, and Dr. Pradip Roy Choudhury, who devoted their precious time for my periodic review and provided their insightful comments and encouragement.

During the course of my Ph.D., I've receive generous help from many senior employees and young colleagues in BARC. I would like to extend my gratitude towards Dr. M. N. Deo, Dr. Jagannath, Dr. Kulwant Singh, Dr. Debarati Bhattachraya, Dr. A.K. Sahu, Dr. D.V. Udupa, Mr. Nachiket Keskar, Mrs. Neelima Khare and Dr. Nagaraj Alangi who let me use their characterization facility. I would also like to thank Dr. Shuvendu Jena for his help in spectrophotometry and other general scientific discussions and motivations.

I am also grateful for the opportunity to be associated with Dr. Archana Sharma, Mr. Martin Mascarenhas, Dr. Namita Maity, Dr. Rajib Kar, Dr. Nirupama Tiwari, Mrs. Vandana Chaturvedi Mishra, Dr. Supriya Chopade and Dr. Gayatri Dhamale. I wish to continue these associations in future.

I really appreciate the help extended by different researchers of Indira Gandhi Centre for Atomic Research (IGCAR), Raja Ramanna Center for Advanced Technology (IGCAR) and IIT- Bombay.

It gives me great pleasure to extend my thanks to Mr. Naresh Chand, Ms. Vanita Sekhar and Mr. Sankalp Thakur for their tireless help in organization and execution of our experiments and solution of several critical technical problems. Without their help it would have been almost impossible to run the experiments. Mr. D. P. Chopade and Mr. Tushar Hire are other persons whose has provided technical support during the period of my research.

My B. Sc. (Physics) professor Dr. Ashim Kumar Mukhopadhyay needs a special mention for showing us the magic of physics and always encouraging for being a better version of our self professionally, and personally.

I can't express my gratitude enough towards my parents and my brother for all the selfless love, care and sacrifices they have made to sustain and shape my life. Their constant support and enthusiasm have helped me to create a balance between my work life, personal life and my ambition for higher education. My loving husband needs a special mention; he provided me strength in the moments of weakness, and self-doubt and helped me endure this saga. Lastly, I owe thanks to my sweet little baby girl for being a wonderful teacher of many important life lessons. She has made me humble, thankful, and taught me to be resilient and patient.

Contents

Page No.

List of Figures

List of Tables

Summary

Boron carbide and its allotropes have gained huge attention of physicists, chemists and material scientists in last few decades. It is a network covalent solid and highly refractory non-metallic, super-hard material having extreme fracture toughness, low density, high melting point, high Seebeck co-efficient, high neutron absorption cross section, good semi-conducting response, and chemical inertness [1-3]. This rare blend of functional properties makes it an ideal candidate for several important scientific and technological applications and has propelled the scientific community to investigate the material further.

In this work, capacitively coupled Radio Frequency Plasma Enhanced Chemical Vapor Deposition (RF-PECVD) technique has been utilized for synthesis of ^{nat}boron carbide ($^{nat}B_xC$) thin films. Several researchers have utilized PECVD technique for fabrication of boron-carbon (B-C) thin films [4-8] earlier, yet, there remains scarcity of reports on detailed analysis of composition, structure and properties of the films as a function of deposition parameters. Therefore in this study, $^{nat}B_xC$ thin films were deposited taking “self-bias” and deposition time as variables to study several associated properties. Neutron absorption cross section, optical properties, and tribological properties of these films have been investigated as a function of composition, thickness, and crystal structure. In addition, a comparison between boron carbide thin films synthesized via PECVD and Pulsed Laser Deposition (PLD) technique has been carried out to understand how different deposition mechanisms affect film microstructure and microchemistry, hence derivative physical properties.

Silicon, Aluminium, Stainless Steel and Sodalime glass substrates were used for thin film deposition aimed at specific applications. Films were synthesized from a single source solid precursor ortho-carborane (o-$C_2B_{10}H_{12}$). Variations in thickness, deposition rate, surface roughness and wear volume were investigated via 3D Optical Profilometry. Surface chemical state and bulk chemical composition was determined via X-ray Photoelectron Spectroscopy

and Proton Elastic Backscattering Spectroscopy, respectively. Chemical bonds were probed using Fourier Transform Infra-Red Spectroscopy. Crystallinity was determined via X-ray Diffraction technique. Surface morphology was examined with Electron Microscopy. Optical constants were determined with the help of UV-VIS-NIR Spectrophotometry in transmission and reflection geometry depending upon the choice of substrate. Stress measurement was performed by Interferometry technique. Tribological properties were measured in a reciprocating Tribometer in dry lubricated condition in ambiance. Lastly, total macroscopic cross-section (Σ_t) for neutron absorption was investigated via Neutron Transmission Measurement technique.

This study revealed that self-bias and film thickness have prominent effect on the composition, microstructure, and ambient stability of the films. With increase in self-bias, B/C ratio in the films decreases. Σ_t increased with self-bias as a result of film compaction. Films deposited at lower self-bias were optically transparent. At a typical wavelength 400 nm, refractive index increased from 1.87 to 1.97 with self-bias on account of increased density. Both direct and indirect band gap reduced with increasing carbon content in the films. Lower self-bias was found to be advantageous for synthesis of $^{nat}B_xC$ films having superior hardness and wear resistance. Higher film thickness was found to be preferable for improved lubricity. Comparative study revealed that, PECVD technique provides conformal, crystalline, super-hard $^{nat}B_xC$ films at high deposition rate, while PLD technique is useful for stoichiometric or near-stoichiometric $^{nat}B_xC$ thin film deposition. Moreover, use of these two different deposition techniques resulted in different stress profiles in the films.

This study demonstrates that, it is possible to deposit $^{nat}B_xC$ films having preferred elemental composition, using appropriate deposition conditions. This in turn leads to better process control and also provide opportunity to tailor film properties.

Chapter 1 : Introduction

Thin films have contributed to modern technological advancements at a rapid pace in last few decades. Study of thin films science involves solid state physics, chemistry and material science. Despite the fact that thin films are well-researched, thin film technology is still developing and many new functional materials are being increasingly investigated. Contemporary research in thin films is mainly directed at various applications such as: electronics, optics, magnetism, superconductivity, defense and military, space science and other industries. This astounding rise in thin films research can be attributed to their undeniable importance in several applications.

Our material of choice is Boron Carbide, most commonly represented as B_4C. This functional material has attracted interest of physicists, chemists and material scientists over last few decades owing to the unique blend of several interesting physical, chemical and mechanical properties in a single material, useful for several advanced technological applications.

Depending upon the nature of application, a variety of techniques can be used for thin film deposition, which is broadly divided into two categories: Physical Vapor Deposition (PVD) and Chemical Vapor Deposition (CVD) techniques. As the name suggests, physical vapor deposition deals with physical transfer of the desired material from the target to substrate. Examples of few popular PVD techniques used are: Sputter Deposition, Pulsed Laser Deposition (PLD), Magnetron Sputtering, Ion beam assisted deposition and thermal evaporation. Chemical vapor deposition on the other hand involves formation of the thin films on the substrate surface by chemical reaction when the surface is exposed to single or multiple volatile precursor vapors. There are several methods of CVD among which Plasma Enhanced Chemical Vapor Deposition (PECVD) technique has been a very popular and widely accepted technology for deposition of superior quality thin films, owing to its many advantages.

This thesis encapsulates the details of synthesis of boron carbide thin films using capacitively coupled RF-PECVD technique. Neutron absorption cross section, optical properties, and tribological properties of these films have been investigated with the help of several characterization methods. Our detailed studies have been aimed at understanding effect of plasma parameters, specifically DC “self-bias”, on physical properties of these films, and assess their utility for various applications. In addition, a comparative study between boron carbide thin films synthesized via PECVD and Pulsed Laser Deposition (PLD) technique has also been carried out to understand how different deposition mechanisms can affect film structure and properties.

In this chapter we begin with a brief introduction of thin films elucidating their importance in material science and technology. The fundamental structure of boron carbide and its and important physical, and chemical properties have been discussed in the next section. Usefulness of boron carbide thin films in evolution of various scientific and technological applications has also been included. Efforts have been made to elucidate the role of plasma in material processing and the basis of choosing PECVD technique for deposition of boron carbide thin films. In the final segment of this chapter, our motivation for this study is highlighted on the basis of exhaustive review of relevant published literature.

1.1 Thin films

Thin film deposition is the method of applying a layer of the desired material with thickness ranging from few angstroms (Å) to about a hundred micron on a surface usually called the “substrate”, to modify and increase the functionality of a bulk material. Surface-to-volume ratio is very high in thin films and the physical and chemical properties are often quite different in comparison to the bulk material having same composition [9]. Moreover, thin films are sensitive to surface properties and thermo-mechanical stresses. Unique characteristics that a material acquires as a function of thickness, geometry and structure of the film, can be exploited for several advanced applications [10].

From ancient times, thin films have been an integral part of the progress, in the process of surface modification of solids. Earliest application of thin films can be traced back to 890 B. C., by Assyrians, who discovered tin glazing in brick work and pottery in order to overcome the porosity, as well as, for decorative purposes [11]. More than 2000 years ago goldsmiths developed a mercury based process to coat the surface of less precious artifacts with precious metals like gold and silver [12] to make them look valuable, and improve their lifespan. Ancient craftsmen were capable of producing these functional coatings despite lack of in-depth knowledge of the underlying physio-chemical processes. In relatively modern history, thin films were probably first synthesized in 1838 by electrolysis method. Metal films were first synthesized by Bunsen and Groves in 1852 by chemical reaction and Faraday obtained metal films by thermal evaporation in 1857 [13]. Although, early investigations of thin films were triggered by sheer scientific curiosity; later their functional characteristics attracted the attention of researchers' globally. In present world, thin film science and technology plays a prominent role in several rapid technological developments. Tremendous advancement in thin and ultrathin film fabrication techniques is the basis of technological breakthrough in several important areas of research, among them; semiconductor industry is one of the greatest beneficiaries. Years of research have culminated in development of thin film based micro and nano-electronic chips which has led to miniaturization of various electronic devices having superior performance. Also, thin films are proven to be extremely advantageous for advanced applications in optics, magnetics, tribology, and also energy conversion, generation, and storage. For example, thin films finds applications as protective coatings, dry lubricants, optical coatings, interference filters, reflecting and antireflection coatings, photoresist layers, catelysts, sensors elements, magnetic memories, piezoelectric devices, thermal energy conversion and storage elements, superconductors, and finally detectors [14-16].

1.2 Boron Carbide

Boron carbide is a synthetically produced super-hard, low Z compound of boron and carbon whose hardness is only exceeded by cubic boron nitride and diamond at ambience. Beyond 1200 ºC it even surpasses the hardness of diamond, earning the name “black diamond” [3]. It was first synthesized by Joly in 1883, identifying it as B_3C. French chemist Henry Moissan reported the production of boron carbide in 1889 as a byproduct during synthesis of metal borides and identified the phase as B_6C [17]. Detailed investigation on this material began only since 1930s and in 1934, boron carbide was assigned its stoichiometric formula B_4C, corresponding to its idealized, most symmetric form [18]. It is a “network covalent solid” with a three dimensional structure of covalently bonded boron and carbon

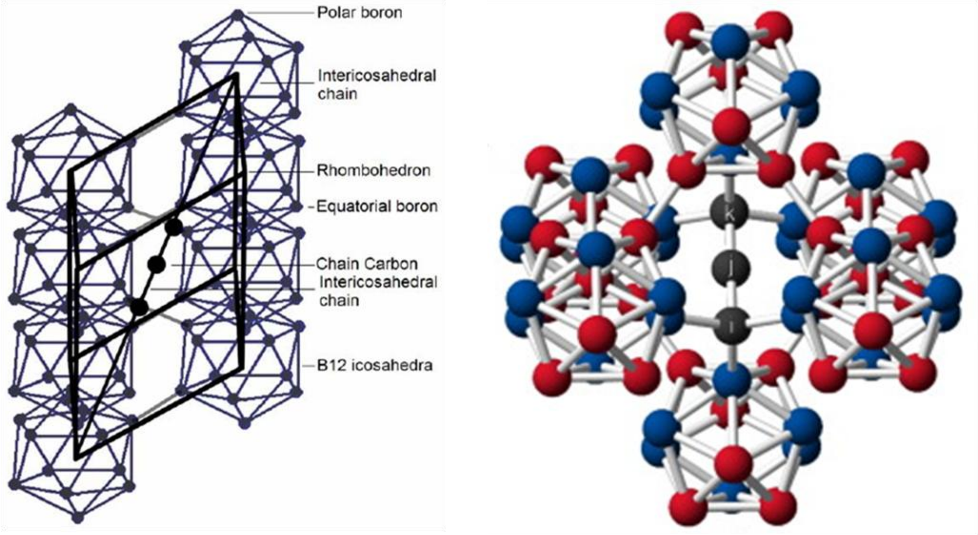

(a) (b)

Figure 1.1: (a) Rhombohedral unit cell of stoichiometric boron carbide, (b) connectivity of atoms in boron carbide unit cell color coded by site: red: polar site, blue; equatorial site, black: chain site.

atoms. Being a network covalent solid, boron carbide does not have discrete molecules; the smallest part of this 3D network is called "formula unit" and defined as $B_{12}C_3$ [18]. Each formula unit consists of a 12 atomic icosahedra essentially made of covalently bonded boron atoms and a three atomic linear chain consisting of carbon atoms. Each icosahedral unit consists of six polar (p) atoms and six equatorial (e) atoms. The polar atoms connect to multiple icosahedra directly and the equatorial atoms connect to multiple icosahedra via chains as shown in Figure 1.1 (a) and (b) [19, 20]. Boron carbide exhibits polymorphism with rhombohedral, tetragonal, and orthorhombic phases. However, the last two phases being metastable are not considered in metallurgical phase diagrams [20]. Most commonly accepted crystal structure of boron carbide is rhombohedral unit cell having trigonal symmetry with R-3m space group. The 12 atomic icosahedra is situated at each of the vertices of the rhombohedra and three atomic linear chain is located along it's body diagonal [3] as shown in Figure 1.1. Boron carbide is equipped with the ability to exist over a stable stoichiometric range from B_4C to $B_{10.4}C$ without undergoing any basic structural change [18, 21, 22]. It can exist as a single phase compound within 8% to 20% carbon content [4]. In the super-stoichiometric range($B/C > 4$), the three chain sites are comprised of single or multiple boron atoms, sometime with non-linear chains also consisting of four or more boron atoms, depending upon the composition. In the sub-stoichiometric range carbon atoms replace the boron atoms first in the chain sites, and then in the icosahedral sites as the structure evolve towards carbon rich configuration [3]. Network covalent solids like boron carbide tend to be extremely hard and brittle due to strong covalent bonding. Also, they have high melting and boiling points due to huge energy requirement for breaking of the bonds. Boron carbide is semiconducting in nature and its lack in electrical conductivity comes due to the involvement of most of the valence electrons of the constituent elements in covalent bonding. Charge carriers in this p-type semiconducting material move with the help of hopping type transport [23]. Various physical properties of boron carbide are listed in Table 1.1 [24].

Table 1.1: Physical properties of boron carbide.

Property	**Minimum Value (S.I.)**	**Maximum Value (S.I.)**	**Units (S.I.)**
Density	2.3	2.55	Mg/ m^3
Bulk Modulus	218	271	GPa
Compressive Strength	2583	5687	MPa
Ductility	0.00058	0.00124	-
Elastic Limit	261	569	MPa
Fracture Toughness	2.5	5	MPa.$m^{1/2}$
Hardness	38100	44100	MPa
Poisson's Ratio	0.18	0.21	-
Young's Modulus	362	472	GPa
Melting Point	2645	2780	K
Specific Heat	840	1288	J/ kg.K
Thermal Conductivity	17	42	W/ m.K
Thermal Expansion	3.2	9.4	10^{-6}/ K
Dielectric Constant	4.8	8	-
Resistivity	100000	1e+008	10^{-8}ohm.m

Among a number of boron rich materials, B_4C as a bulk material has been established as a widely used, important material for a vast range of advanced technological, and industrial applications. Only in last few decades, boron carbide thin films have emerged as a significant material in high-technology nuclear applications, soft X-ray and EUV optics, energy generation and storage, medicine, and semiconductor industry [25]. The possibilities of fabrication of solid state neutron detectors, high temperature thermoelectric energy conversion devices, and superconducting materials using boron carbide are also being explored [18]. Different application areas where boron carbide thin films can find their importance are listed in Table 1.2.

Table 1.2: Different Application areas of boron carbide thin films.

Application Field	Examples
Semiconductor industry	Detectors and sensors. Photovoltaic solar cells. Electrical connection in microelectronic devices, epitaxial layers.
Optics	Antireflection coating on lenses or solar cells, reflection coatings for mirrors. Coatings for decorative purpose (color, luster). Interference filters. CD's DVD's and other hard drives. Waveguides. Photosenistive coating of "analog" film for old cameras.
Chemistry	Diffusion barriers. Protection against corrosion / oxidation. Sensors for liquid/ gaseous chemicals.
Mechanics	"Super-hard" tribological layers. Adhesion providers. Friction reduction.
Magnetics	Hard Disks. Video / Audio tape. SQUIDS
Electrical	Dielectric / conducting films for resistors and capacitors. Piezoelectric devices.

1.3 Deposition methodologies:

In the beginning, research on boron carbide was primarily focused on investigating the synthesis routes, structure, and properties of the bulk material. Since early 1990s, the scenario of research on boron carbide has been changed; with increased focus towards thin film and nanostructures. Quite a few number of researchers have done excellent investigations, exploring different thin film deposition techniques [22]. Improper selection of deposition techniques can lead to irreproducible results in terms of thin film properties, diminishing usefulness of the synthesized films for practical applications. In past two decades, enormous advancement has taken place in boron carbide thin film research and several researches have made exceptional efforts to correlate the effect of deposition parameters on structure and properties of thin films [26-28]. As mentioned in the very beginning of this chapter, thin film deposition techniques can be divided into two broad categories: Physical Vapor Deposition (PVD) and Chemical Vapor Deposition (CVD). In next two sections, these two techniques will be discussed briefly.

1.3.1 Physical Vapor Deposition (PVD):

Physical Vapor Deposition or simply PVD technique refers to the combined set of processes which are used to deposit thin films from few angstroms (Å) to several micrometers [29] μm thickness. Different PVD processes utilize three fundamental steps which involve target material going from a condensed phase to the vapor phase and then again back to condensed phase on the substrate surface to generate thin films. Difference between various PVD techniques arises primarily from the energy sources used for evaporation of the target materials. Two most popular PVD processes are sputtering and thermal evaporation [30]. In sputtering, a plasma medium is used to sputter out the atoms from the target material whereas in thermal evaporation, the target is heated to convert it to vapor form. Other commonly used PVD techniques are; Pulsed Laser Deposition (PLD), Ion Beam Sputtering, Electron Beam Evaporation and Cathodic Arc Deposition. Recent advancements in thin film technology and nano-science has increased the utility of PVD techniques for production of thin material layers with desired microstructure and properties [31]. Different PVD techniques can be used for a variety of application including surface modification for enhancement of surface properties of a material, fabrication of electronic and microelectronic devices, electrodes in battery and fuel cells, diffusion barriers, and optical coatings [32, 33]. Most remarkable advantage of PVD process is the deposition of thin films of high stoichiometric purity. Most prominent disadvantage of PVD techniques is that it utilizes line of site deposition which limits its utility for providing conformal coating on substrates of complex geometry.

1.3.2 Chemical Vapor Deposition (CVD):

Chemical Vapor Deposition, also called as CVD refers to a family of deposition processes where a thin film is synthesized from a precursor vapor by means of chemical reactions occurring on or near the substrate surface. Main advantage of CVD processes is production of conformal coatings of uniform thickness on substrates of complex shapes. It also ensures homogeneity in properties and low porosity of the deposited thin films in comparison with their PVD deposited counterparts. CVD has another powerful ability of selective deposition on patterned substrates [34]. Thin films of a wide variety of materials can be synthesized using CVD techniques such as metals, oxides, borides, carbides, nitrides, sulfides, phosphides, arsenides, and silicides. CVD is also useful for preparation of high-temperature materials (tungsten, ceramics, etc.), production of solar cells, high-temperature fiber composites, and nano-particles of well-defined sizes. Most recently, high critical temperature (T_c) superconductors and carbon nano-structures have been synthesized by this technique. There exists an array of CVD processes, which can be utilized for synthesis of thin films. Few examples of CVD techniques are; Plasma Enhanced CVD (PECVD), Hot Wire CVD (HWCVD), Remote Plasma-Enhanced CVD, Rapid Thermal CVD, Metal-Organic CVD (MOCVD), Atomic layer CVD, Atmospheric Pressure CVD, Low-Pressure CVD, Ultrahigh Vacuum CVD, Direct Liquid Injection CVD, Hybrid Physical–Chemical vapor deposition, Aerosol-Assisted CVD, and Vapor-Phase Epitaxy [34].

Among other CVD techniques, Plasma Enhanced Chemical Vapor Deposition (PECVD) technique is the most widely accepted within thin film industry. Plasma being the most essential part of this technique has led to the name “plasma enhanced” CVD technique. In PECVD, an electrical energy, usually in the DC, radio frequency or microwave region is used to create the plasma in glow discharge mode for thin film deposition. PECVD techniques require comparatively lower process temperature and provide tunable control over the chemical composition of deposited thin films, which are the main reasons behind its popularity [35, 36]. In PECVD, the activation energy for different favored chemical reactions required for formation of thin films is mainly supplied by energetic species present in the plasma. This plasma medium helps in the efficient fragmentation of vapor phase precursors. It also enhances the chemical reaction rate between different reactive species on the substrate surface, without requirement of very high substrate temperature as opposed to PVD processes. Commonly, “non-thermal plasma” or “cold plasma” medium is used for thin film fabrication via PECVD.

Plasma is often referred to as the fourth state of matter and is defined as a “quasi-neutral” gas of neutral and charged particles exhibiting “collective behavior” [37]. It exists in several forms in nature and has a widespread application in science and technology. Depending upon the relative temperature of charge species and the neutrals, plasma can be divided into two classes; thermal plasma or hot plasma and non-thermal plasma or cold plasma. In thermal plasma, positive ions, electrons and neutral gas atoms are at same temperature ($T_e = T_i = T_g,\ T_e$) and in cold plasma, electrons are at much more higher energy than the other species $\left(T_e \gg T_i \gg T_g\right)$ due to lack of sufficient number of collisions to reach thermodynamic equilibrium. Extensive use of plasma in material processing is fuelled by the fact that a range of parameters of the ionized medium can be utilized which is inaccessible by means of other techniques. For example, the energy densities and gas temperatures offered by plasma is not achievable in any other medium. The need for different plasma based techniques for synthesis of materials in various forms is fulfilled by varying plasma conditions, device geometries, and excitation methods [38]. Plasma based processes forms the backbone of many technological advancement. The entire semiconductor industry relies on PECVD technique for synthesis of various semiconducting materials, surface modification, and etching of required patterns for electrical connections on micro-electronic devices. Various applications of plasma processing technology is illustrated in Figure 1.2 [38].

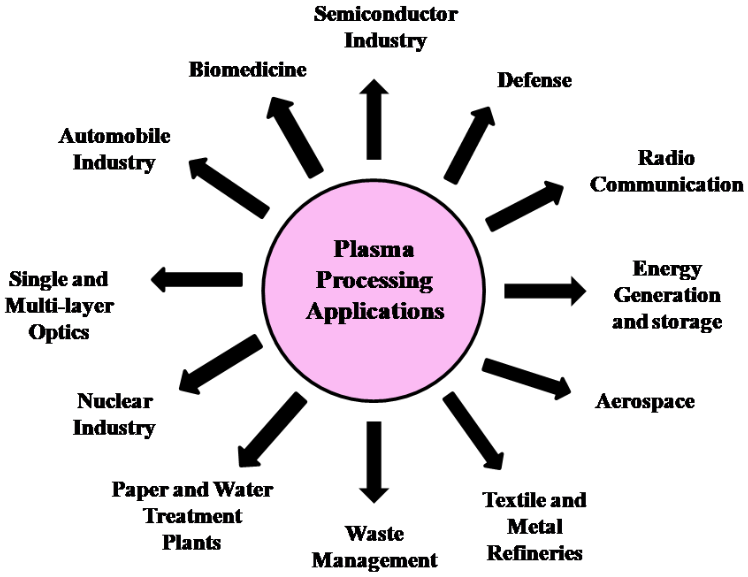

Figure 1.2: Technological applications of plasma.

Non-thermal PECVD processes are usually categorized on the basis of the electrical energy sources used to generate plasma. Details about few non-thermal plasma sources and most importantly the fundamentals of capacitively coupled PECVD technique; used in this study for deposition of boron carbide thin films, will be discussed in the next few sub-sections.

1.4 Non-thermal plasma sources for PECVD:

In all non-thermal plasma sources, plasma is used as a tool which assists in and/ or enhances the favorable reactions in deposition process. The internal state of the plasma affects the properties of the deposited materials. In last two decades, non-thermal, low pressure plasma based deposition techniques; specifically PECVD has emerged as a vital tool for scientific and technological progress for thin film fabrication. The non-thermal plasma discharges can be mainly divided into two categories: Direct Current (DC) discharges and Alternating Current (AC) discharges.

1.4.1 Direct current (DC) Discharge:

A simplest schematic of the set-up for DC glow discharge is shown in Figure 1.3 [39]. The system mainly consists of one cathode and one anode separated by a distance. Both the electrodes are mounted inside a vacuum chamber, filled with a discharge medium; usually a inert gas (e.g. Argon) and the chamber is kept at sub-atmospheric pressure. When a sufficiently high voltage is applied in between the electrodes, cosmic electrons present in the chamber start gaining kinetic energy in the electric field developed between the cathode and anode. When the electron kinetic energy is greater than or equal to the ionization energy of neutrals, electrons ionizes neutral atoms upon collisions. If α is the probability that one energized electron coming from cathode will ionize a neutral gas atom as it travels $1\ cm$

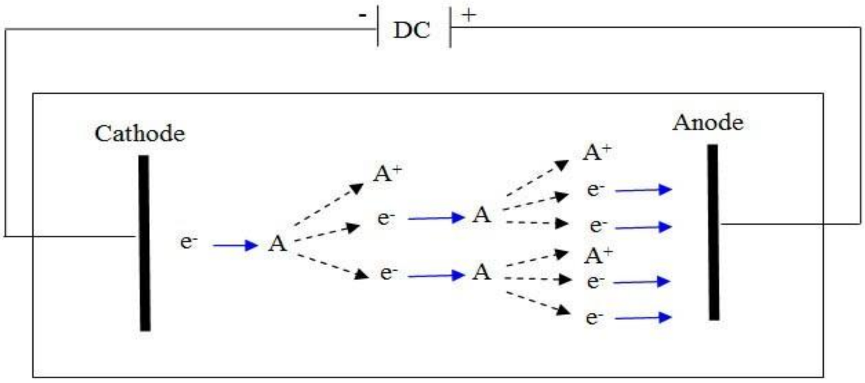

Figure 1.3: Schematic of a DC discharge system.

distance along the length of the discharge tube, $exp(\alpha d)$ no. of electrons will be released via ionization, as the primary electron reaches the anode at a distance d from the cathode. Here, α is called the first Townsend co-efficient. This implies, $exp(\alpha d)$ no. of ions is also released by the primary electron. The secondary electrons produced by ionization are continuously being lost upon reaching anode. An equal amount of ions have to be given up at the cathode to maintain charge neutrality. These ions, while impinging on the cathode, will produce secondary electrons with efficiency γ, where γ is the second Townsend co-efficient. Therefore the number of secondary electrons produced by the ions is $\gamma exp(\alpha d)$. To maintain the discharge, ions bombarding the cathode must produce at least one secondary electron. Thus the condition for sustaining discharge can be written as,

$$\gamma \exp(\alpha d) = 1 \ldots\ldots\ldots\ldots\ldots\ldots\ldots\ldots..(1.1)$$

The relation of the breakdown voltages (V_B) required for producing discharge with chamber pressure and distance between the electrodes can be expressed as equation (1.2),

$$V_B = \frac{A*pd}{(\ln(pd)+B)} \ldots\ldots\ldots\ldots\ldots\ldots\ldots\ldots(1.2)$$

Where, V_B is the breakdown voltage, p is gas pressure, d is the distance between the electrodes and B is constant. This equation leads us to Paschen curve shown in Figure 1.4.

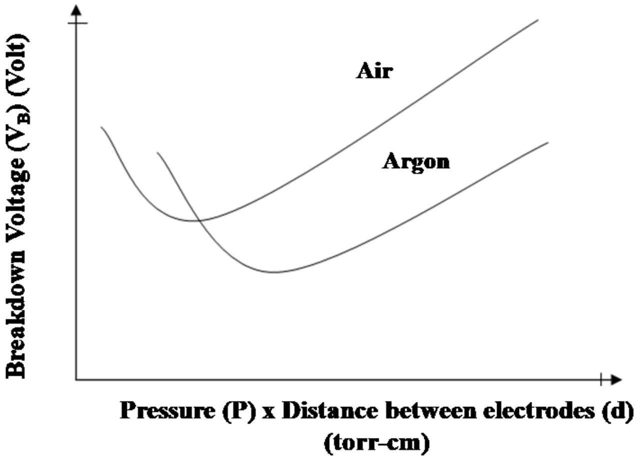

Figure 1.4: Plot of breakdown voltage of air and argon gas as a function of the product of pressure and electrode spacing.

It is seen that for low pressure, breakdown voltage is high. At that pressure the mean free path of the electrons are so large that there is not sufficient no. of collisions to produce the discharge. To increase the probability of ionization of the neutrals via collision, the breakdown voltage V_B rises. At sufficiently higher pressure, V_B rises again. At higher pressure, the mean free path of the electrons are considerably small, therefore between two collisions they are unable to acquire sufficient kinetic energy required to ionize a neutral gas atom. To compensate for that, the breakdown voltage rises again. In between these two maxima, there is a minimum where $V_B$is the smallest. Since in any given DC discharge system, the distance between the electrodes is usually kept constant, it is of absolute importance to find the particular pressure regime for producing efficient discharge.

1.4.2 Alternating Current (AC) Discharge:

For sustaining a DC discharge, the electrodes must be conducting. This DC glow discharge model becomes unsuitable for deposition of insulating materials. During deposition, the electrodes get covered by insulating material gradually and the combination of two parallel electrodes with a dielectric material between them acts as a capacitor. Electrodes are then charged up due to accumulation of either positive or negative charges and eventually the glow discharge is extinguished as the applied DC signal is blocked. To overcome this problem, AC discharges are employed. In an AC discharge, the polarity of cathode and anode are changing in each half-cycle of the applied signal. The ions and electrons respond to the instantaneous cathode and anode respectively, depending upon the frequency of the applied AC field. Therefore, the charges built up in one half cycle of the applied electric field in any of the electrodes will be partially neutralized by the charges of opposite sign in the next half cycle. The frequencies used for AC discharges generally remains in the radio-frequency and microwave range. In the following sub-sections, few most popular low pressure AC discharge plasmas systems will be discussed.

1.4.2.1 Microwave plasma discharge (MD):

Electrical discharges generated by the electromagnetic waves of frequency greater than 300 MHz are called microwave discharges. The microwave frequency typically ranges between 300 MHz to 300 GHz. But the frequencies used for material processing, industrial, medical, and other scientific and technological applications are limited as they must correspond to the permitted microwave frequencies; most commonly used frequency being 2.45 GHz [40]. At such high frequency, the power is coupled to the plasma with the help of a waveguide and antenna for efficient power transfer. The simplified schematic of a microwave plasma discharge system is shown in Figure 1.5 [41]. Similar to all ac discharges, electrons in the plasma reactor first acquires enough energy to create microwave glow discharge. Oscillation of electrons gives rise to different modes in the plasma and the microwave couples to a mode of the plasma to help in sustaining the discharge [42, 43]. Power

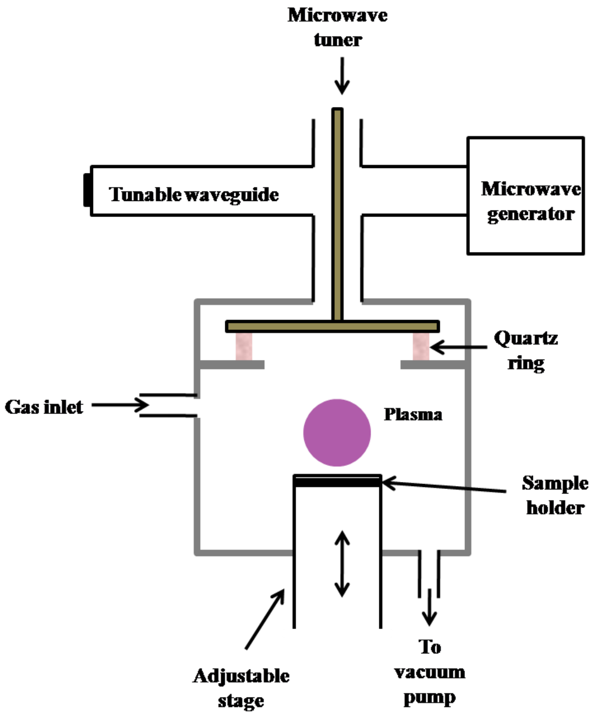

Figure 1.5: Schematic of a low pressure microwave discharge plasma system.

absorption in MD's depends on chamber pressure. In any plasma medium, electromagnetic wave cannot propagate through plasma if frequency of the incoming electromagnetic radiation is greater than plasma frequency of the medium. The number density of the plasma associated with this plasma frequency is called "critical density" and for existence of plasma, this electron number density cannot increase beyond this value. For a applied microwave signal of frequency 2.45 GHz, this critical density is calculated to be $7.3 \times 10^{16}\ m^{-3}$. In this type of plasma, ion temperatures can go as high as 1200°C as a result of high collision rate between electrons and ions. Deposition rate is also higher in microwave plasma owing to higher operating pressure. MD's have been extensively used for deposition of several carbon allotropes. This system is commercially used for synthesis of large single-crystal diamond.

1.4.2.2 Microwave Electron-cyclotron resonance (ECR) plasma discharge:

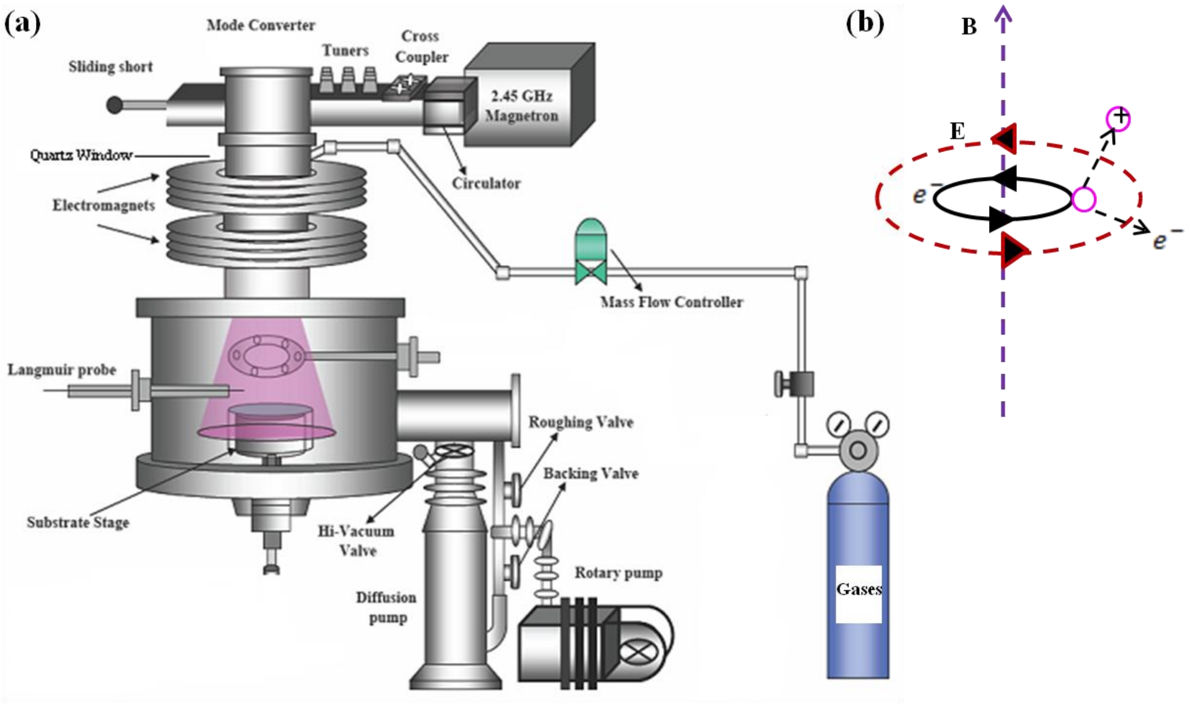

Figure 1.6: (a) A typical arrangement for microwave ECR plasma discharge system and (b) Energy transfer mechanism in a microwave ECR system.

A typical experimental set-up for microwave ECR plasma discharge system is shown in

Figure 1.6 (a). In such systems, plasma is produced by interaction of microwave radiation with the cosmic electrons, in the presence of optimum magnetic field. Maximum power transfer occurs when cyclotron resonance condition is satisfied; i.e. applied microwave frequency equals to electron cyclotron frequency. For a typical microwave frequency 2.45 GHz, the magnitude of the applied magnetic field necessary for the electron cyclotron resonance is 875 Gauss. For generation of ECR plasma, a linearly polarized microwave signal is applied axially in the plasma generation chamber through a dielectric wall (e.g. quartz). A linearly polarized electric field is essentially a combination of a right-handed circularly polarized wave (RHP) and a left-handed circularly polarized wave (LHP); with electric field vectors rotating in opposite directions. Electric field vector in RHP rotates in right handed way perpendicular to the direction of applied magnetic field (B) with a frequency ω_f. Cosmic electrons present in the plasma chamber also gyrate along the induced electric field lines (E), with a different frequency $\omega_{ce} = {Be}/{m}$ which is independent of the velocity of the electrons. Where, ω_{ce} = angular frequency of the cyclotron motion, B = critical magnetic field, e = charge of an electron, m = mass of an electron. Resonance occurs when $\omega_f = \omega_{ce}$ and at this condition maximum power is transferred from the applied microwave radiation to the plasma [44]. Electrons gain energy from this circular electric field continuously under the influence of the force $F = -eE$, until they encounter ionizing collisions with neutral atoms, as shown in Figure 1.6 (b). ECR plasma is usually generated in the pressure regime $10^{-4} - 10^{-5}$ mbar. At this low pressure, the deposition rate is very slow but deposition is always uniform and 'atom by atom' deposition is possible at this pressure. Plasma densities obtained is ~ $10^{17} - 10^{18}\ m^{-3}$. ECR plasma system finds application in production of thin films with low porosity and high thickness uniformity. It is also used as high density ion-beam source.

1.4.2.3 Inductively coupled RF plasma discharge (ICD):

Figures 1.7(a) represents a simplified arrangement for the inductively coupled RF plasma discharge system. In such discharges the powered is coupled to the plasma via transformer action. Usually a conducting helical coil is wound axially around a cylindrical plasma vessel made of dielectric material such as glass or quartz tube. RF power is fed to the helical coil which acts as the primary and the plasma generated inside acts as secondary.

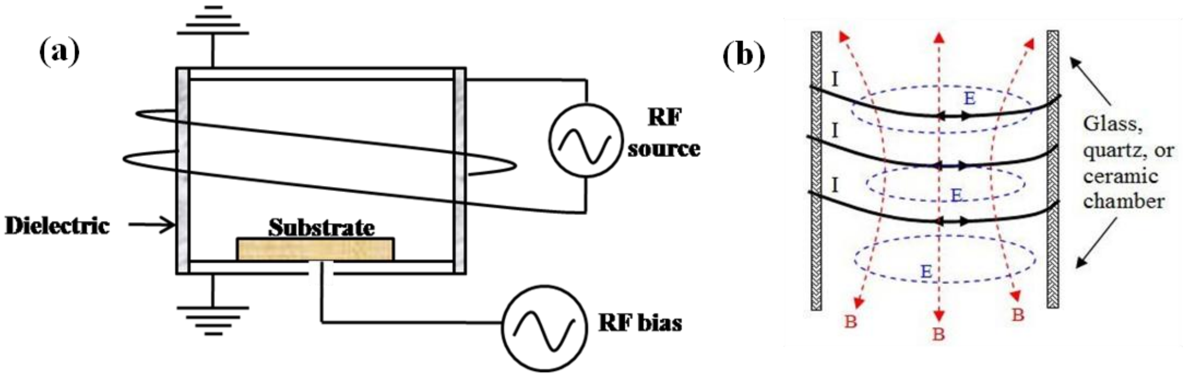

Figure 1.7: (a) Schematic of a typical inductively coupled RF-PECVD system and (b) Schematic representing energy transfer mechanism in ICD.

Main difference of this arrangement with actual transformers is absence of the magnetic core. Typically RF signals of frequency in the MHz range (most commonly ~ 13.56 MHz) are used for such systems. At these frequencies, power coupling via transformer action is quite efficient. When a current is applied to the solenoidal primary windings outside plasma vessel, a magnetic field is developed inside the dielectric vessel. A typical distribution of such magnetic field (B) lines as shown in Figure 1.7(b) [39]. This induced magnetic field (B) produces electric field (E), where the electric field lines forms closed loops in planes perpendicular to the magnetic field lines. The electrons follow the closed electric field lines and gains energy to ionize the gaseous medium. Owing to the movement of electrons in the closed loops, the loss of electrons from the system is much less in ICD's as compared to CCD's and the plasma densities obtained are relatively high ~ $10^{19} m^{-3}$. ICD's find application in thin film deposition, plasma etching, ion sources for mass spectroscopic analysis etc.

1.4.2.4 Capacitively Coupled Plasma Discharge (CCD):

The frequency range of radio frequency (RF) sources used for capacitively coupled AC discharges is $1\,\text{kHz} - 10^3$ MHz, with most commonly used frequency of 13.56 MHz, having wavelength of approximately 22 meters. CCD's can be initiated in other frequency ranges also; but the frequency of the applied AC signal should be high enough so that duration of one half cycle is less than the time taken by the insulator to charge up. Only then the discharge can be sustained [44]. The term "capacitively coupled" is generally used to describe the method of coupling input power to the glow discharge plasma. RF-CCD in parallel plate geometry is one of the most commonly used low presser plasma discharge configuration due to the simplicity in equipment design. In this geometry, two electrodes and their corresponding sheaths form a capacitor, earning the name "capacitively coupled". The schematic of a typical capacitively coupled RF-PECVD system is shown in Figure 1.8 [45].

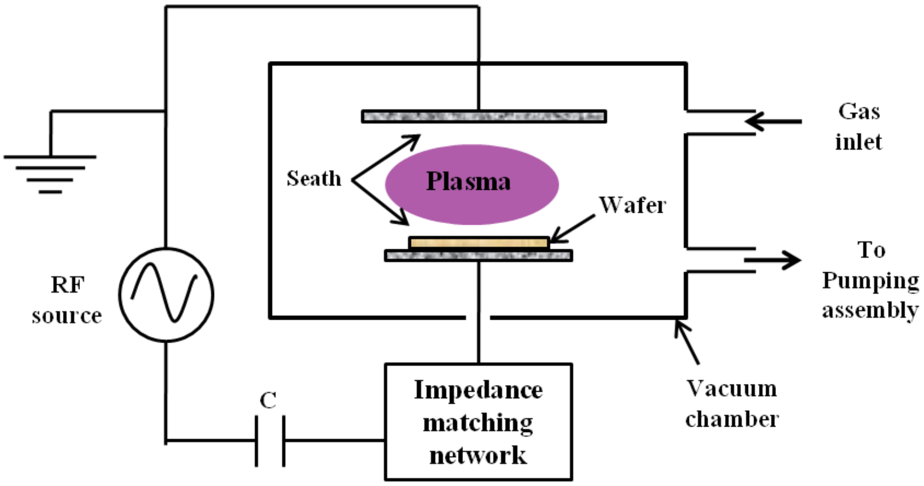

Figure 1.8: Schematic of a typical capacitively coupled RF-PECVD system.

In CCDs, the energy is transferred from the applied radio frequency field to the plasma discharge via collisions between constituent particles of the plasma. The oscillating sheath near the powered electrode also plays a significant role in determining the plasma chemistry [46-48]. In parallel plate CCD geometry, usually a blocking capacitor is connected between the powered electrode and RF generator. As the name suggests, this capacitor blocks DC current to flow between the electrode and RF generator and only allows AC current to pass and initiate the plasma discharge. Both the electrons and ions in the plasma respond to the instantaneous field. Owing to the high mobility, number of electrons reaching the instantaneous anode is more than the number of ions reaching the same in a particular time interval.

Let us consider one full cycle of the applied RF signal at any instant. In the positive half cycle, the powered electrode is positive, therefore electron current reach the powered electrode, eventually the capacitor C, charging it negatively. In the next half cycle, the powered electrode becomes negative, the capacitor then gets charged up by ion current and the amount of negative charge stored in the capacitor is reduced as the ions neutralize some of the available electrons. Since electrons are more mobile than ions, number of electrons reaching the capacitor will be more than the ions after a complete cycle of the applied RF signal. As a net effect, some amount of negative charge will remain stored in the capacitor after completion of one full RF cycle. Over few more cycles, a time averaged negative DC potential will develop in the powered electrode called “self-bias”. All these phenomena take place within a very small time scale (~ ns). Development of DC “self-bias” requires two conditions to be satisfied: (i) the electrodes must have different surface area and (ii) a blocking capacitor should be present in the circuit. Role of this “self-bias” is to prevent further loss of electrons from the plasma and help maintaining “quasi-neutrality”. “Self-bias” is an important feature of the RF-CCD plasma and plays a pivotal role in material processing via etching and deposition. Self-bias controls both the ion flux, and ion energy impinging on the powered electrode. If the substrate is kept on the powered electrode, ions are accelerated towards the substrate under the influence of a potential whose magnitude is equal to the sum of plasma potential and the self-bias. Incoming ions will then bombard the surface of the growing film during deposition and affect the atomic arrangement, altering the composition, crystallinity, and several derivative properties of the films. CCD's are used for various plasma processing applications, predominantly in thin film deposition and plasma etching. Plasma densities obtained in CCD's are in the range $10^{15} - 10^{16}\ m^{-3}$.

Apart from the plasma sources discussed in section 1.5 of this chapter, there are many non-thermal and thermal plasma sources that have not been incuded here. Several thermal plasma sources that utilize DC and AC discharges are also used in material processing and other applications. For example: thermal plasma is being utilized for thick coatings, material cutting, waste management, welding, spraying, micro, and nano-powder synthesis, circuit breakers, and arc lamps [49-52]. Thermal plasma applications are usually carried out at atmospheric pressure. They provide high energy densities ($> 10^{9}\ J\ m^{-3}$) and is extremely useful for rapid treatment of materials. The deposition rates achieved are also much greater than that obtained by non-thermal plasma processes. This high deposition rates is advantageous for thicker coatings but it also comes with some drawbacks. For example, due to high deposition rate, the control over deposition parameters and hence film composition decreases, films often have significant porosity, thickness non-uniformity, and a higher degree of impurity as compared to their low pressure counterparts. Irrespective of this fact, thick coatings deposited by thermal plasma spray technique has widespread application where porosity and other aforementioned limitations do not affect the intended application.

There are few popular non-thermal plasma devices that operate at sub-atmospheric and atmospheric pressure that also have not been discussed here. Among them dielectric barrier discharge (DBD) is the most popular plasma processing technique which is usually used for water purification and textile industry. Also, some of the atmospheric pressure non-thermal plasma devices are used for thin film deposition and medical applications. These types of devices are relatively new and a lot of research and development is going on globally to investigate their utility in material processing.

Since in our study, PECVD technique have been utilized for thin film deposition, a few other contemporary non-thermal plasma sources have been discussed to give an essence about the utility and importance of these cold plasma sources for thin film fabrication.

1.5 Literature survey:

This section includes relevant literature survey on PECVD deposited boron carbide thin films from the year 1989-2019. A few of the noteworthy contributions are presented in a chronological order. Several researchers have been involved in the boron carbide thin film research in terms of finding out appropriate PECVD technique suitable for specific application; for example in tokamak. Others have been investigating chemical composition, structure, surface morphology, local chemical environment, and several associated derivative properties of PECVD deposited films.

S. Vepřek et al. in 1989 [53] reported in-situ PECVD of boron-carbon coatings for tokamak. Optimization of materials properties for their application as protective coating in first wall in tokamak devices were the focus of this study. Mainly, compositional depth profile of the films, evolution of composition with temperature, and thermal shock response was investigated.

J. Winter et al. in 1990 [54] utilized a less hazardous precursor borontrimethyl $B(CH_3)_3$ for fabrication of amorphous boron containing carbon films (a-C/B:H) on inner surfaces of tokamak. The films showed similar qualities and properties as the boron carbide films prepared by other precursors.

V. K. Alimov et al. in 1992 [55] utilized DC glow discharge plasma and studied the effect of utilization of various precursors and substrate bias on the local chemical environment, composition, and structure of a-B/C:H films. It was found that stoichiometric boron carbide films are most useful as inner lining of T-11M toakmak.

In the same year, O.I. Buzhinsky et al. [56] conducted a research to develop a simple novel technique for boronization of T-3M and T-11M tokamak chambers. The study compared this novel technique with other traditional boronization techniques. Characterization of the deposited films was not performed in this case.

It is evident from the examples mentioned above that during the period 1989-1992; the research on PECVD deposited boron carbide thin films were fuelled by the need of development of a self-cleaning, protective, refractory coating layer for inner walls of tokamak. Naturally, most of the studies were focussed on novel process development for the same. Several research groups utilized a variety of plasma sources and combination of precursors to achieve that. Reports regarding in-depth studies on the affect of deposition parameters and/or processes on the material properties are quite scarce in this era.

In 1992, H. Künzli et al. [57] studied the influence of feed precursor gases; trimethyl boron $B(CH_3)_3$ and B_2H_6/ CH_4 process gases on the composition of deposited boron carbide thin films via in-situ spectroscopic studies.

In the same year, S. Lee et al. [7] investigated properties of PECVD deposited boron carbide thin films synthesized from boranes. Composition of the films was controlled by changing the partial pressures of Nido-decaborane, nido-pentaborane and methane gas mixture. Electronic structure, and optical properties were studied for fabrication of photosensitive p-n heterojunction diode.

Later, D. Byun et al. in 1995 [58] did a comparative study of boron carbide-n Si(111) heterojunction diodes prepared by two essentially different CVD techniques- PECVD and synchrotron radiation CVD. Effect of utilization of different precursors was also studied. The resulting electronic properties were found to be independent of crystalline structure.

A. A. Ahmad et al. [59] in 1996 investigated optical properties of PECVD deposited boron carbide (B_5C) thin films with the help of variable angle of incidence spectroscopic ellipsometry. Optical constants near the band edge of the thin films were determined from infra-red to UV region. This study reveals effect of using different substrates on homogeneity of the refractive index of the films.

In 1998, Kyu-Wang Lee et al. [60] studied boron carbide films grown via microwave PECVD from H_2 + CH_4 + BCl_3 gas mixture. Stoichiometric variation of the thin films were studied as a function of input gas composition and found to be independent of the same. The underlying reason causing this behaviour remained unanswered.

S. Adenwalla et al. in 1999 [5] investigated diode characteristics of a boron carbide/ silicon carbide heterojunction in the temperature range 24 to 351 °C, prepared by PECVD technique. The devices exhibited good semiconductor diode behavior on account of improved crystallinity. This work opened the possibilities for further research on boron-carbide heterojunction semiconductors for detector and sensor applications.

It can be seen from the aforementioned researches that in 1990s, PECVD synthesized boron carbide thin film research was mainly focused on fabrication of heterojunction semiconducting devices. These devices are particularly useful for detector applications. This inspired a number of researchers in the coming years to test the efficacy of these boron carbide based semiconductors.

In 2006, A. N. Caruso et al. [8] investigated a boron carbide diode detector, fabricated from two different polytypes of boron carbide. The measured detection efficiency was in agreement with calculated value. In this study, variation in detection efficiency due to alteration in film thickness was also studied.

P. A. Dowben et al. In 2009 [61] studied the effect of transition metal doping on the electronic properties of boron carbide homo-junction diodes. Ni, Co and Fe were found to be successful dopants of PECVD grown boron carbide thin films. The study was based on the assumption that polytype of PECVD grown semiconducting boron carbide with the aforementioned dopants is same as its undoped PECVD grown counterpart. However, identification of the structural polytypes associated with the PECVD grown semiconducting boron carbide remained unsolved.

Boron carbide being a versatile material is useful for many advanced technological applications and needs to be studied in detail. Study of the effect of PECVD process parameters on the composition, structure, and other associated properties is of utmost importance as it enables us to have control over the stoichiometry and properties of the deposited film. Due to its complex structure, it has been a challenge to the researchers to identify accurate structure and atomic positions of constituent atoms in boron carbide, which need advanced studies.

H. Werheit et al. [62-70] have been dedicatedly investigating the structure, composition and associated electronic properties of the boron carbide thin films for more than two decades. Their in-depth advanced studies are mainly focused on investigation of different polytypes and identifying the position of different constituent atoms via Fourier transform infre-red spectroscopy and other relevant advanced characterization techniques.

As an extension to the study reported by P. Dowben et al. in 2009 [61], J. Liu wt al. published their work in 2010 [71] on investigation of transition metal doped boron carbides produced by PECVD from ortho-carborane (closo-1,2-C2B10H12) and 3d metal metallocenes. K-edge extended X-ray absorption fine structure and X-ray absorption near edge structure measurements of the films were analyzed in this study.

One of the few recent researches on PECVD deposited boron carbide thin films were carried out by N. Hong et al. in 2013 [72] on time of flight neutron detection with the help of a boron carbide-heterojunction diode. The Maxwell–Boltzmann neutron spectrum of the device was measured. The study of relevant material properties revealed the probability of tuning the efficiencies by simply varying the thickness and/ or ^{10}B enrichment of the film.

E. Echeverría et al. [73] in 2015 investigated semiconducting boron carbide/ pyridine polymers for neutron detection at zero bias. Results of this study suggest that modifications in the structure/ doping in boron carbide may help in synthesis of better neutron voltaic materials.

In 2016, B. Dong et al. [74] studied composite films of pyrimidine/ B_5C, pyridine/ B_5C and aniline/ B_5C fabricated using PECVD for neutron detection and photocatalysis. The study was focused on investigation of resonance stabilization energy of the aromatic precursors which will result in intact π networks in PECVD films, which directly affect electronic properties of such films.

In the same year, B. J. Nordell et al. in 2016 [75] published an extensive full factorial investigation of PECVD-grown amorphous hydrogenated boron carbide for detector application. Compositional variation in films was achieved by variation of growth rates via changing pressure, and partial precursor flow rate. In addition, effect of variation of temperature, and pressure on composition was also studied. Efforts have been made to correlate the electronic properties with the atomic percentage of hydrogen in the films.

M. Nastasi et al. in 2018 [76] studied electrical, and structural properties of the amorphous hydrogenated boron carbide on silicon p-n heterojunction diodes following irradiation with thermal neutrons. The study revealed improvement in diode performance due to neutron irradiation on account of passivation of defects.

A. Oyelade et al. [77] in 2018 studied charge transport properties of PECVD deposited boron carbide films, alloyed with aniline moieties as a function of composition. Improvement in the charge carrier lifetimes, and capacitance versus frequency behaviour in the films was observed due to doping with aniline.

In spite of all these studies, there is still a scarcity of reports on the effect of variation of plasma parameter, specially “DC self-bias”, during PECVD of ^{nat}boron carbide films on various associated properties. In this study, we have investigated the effect of variation of this DC “self-bias” on the composition, crystallinity, and microstructure of the ^{nat}boron carbide thin films. Efforts have been made to correlate structural and compositional changes to the optical properties of the films. In addition, total macroscopic cross section for neutron detection of these ^{nat}boron carbide films have been measured as a function of film composition/ self-bias. Since boron carbide is known to be a super-hard material with excellent tribo-mechanical applications, tribological properties of the films as a solid lubricant have been measured as a function of composition and film thickness. In the last part of this study, we have compared the optical properties and internal stresses in ^{nat}boron carbide thin films deposited by PECVD and PLD technique. Films produced by these two techniques have different crystalline structure, adhesion, and physical and chemical properties that make each of them suitable for specific applications. Our study demonstrates the possibility of deposition of ^{nat}boron carbide thin films with desired pre-determined composition, structure, and associated derivative properties needed for neutron detection, fabrication of optical materials, and other advanced applications.

Chapter 2 : Experimental and characterization techniques

This chapter describes the details of the experimental setup used for Plasma Enhanced Chemical Vapour Deposition (PECVD) of ^{nat}boron carbide thin films. Each element of the hardware and their utility in the PECVD process is highlighted. For deposition of thin films, a variety of substrates: aluminium, stainless steel, sodalime glass and Si (100) have been used, based on their different applications. In some instances, choice of substrates was driven by ease of characterization. For each type of substrate, there exists a different cleaning method. A brief description of each of these substrate cleaning methods are also included in this chapter. Various properties of the deposited ^{nat}boron carbide thin films have been investigated using multiple characterization techniques. Basic principles and procedures for each of the techniques have been discussed in this chapter. Also, a brief description of the setup used for Pulsed Laser Deposition (PLD) of $^{nat}B_xC$ thin film for our comparative study is included.

2.1 Thin film deposition techniques:

2.1.1 Experimental set-up for PECVD:

In this study, ^{nat}boron carbide thin films have been deposited using a capacitively coupled Radio Frequency Plasma Enhanced Chemical Vapor Deposition (RF-PECVD) system. The schematic of the experimental set up is shown in Figure 2.1 [78]. The deposition chamber primarily consists of a double walled cylindrical stainless steel (316) plasma CVD reactor. This chamber is connected to a vacuum pumping assembly consisting of a rotary and an oil-diffusion pump. The chamber is at first evacuated to a base pressure of 5×10^{-5} mbar using the oil-diffusion pump to get rid of the residual gases and moisture. Actual depositions are carried out at rotary vacuum ~ 10^{-2} mbar. Inside the chamber there is a stainless steel substrate holder which is connected to a 13.56 MHz RF power supply through an automated impedance matching network assembly, with the help of a RG 213 cable. In this configuration, the substrate holder itself acts as the powered electrode. During deposition, depending upon the plasma conditions, impedance of the substrate holder-plasma system can

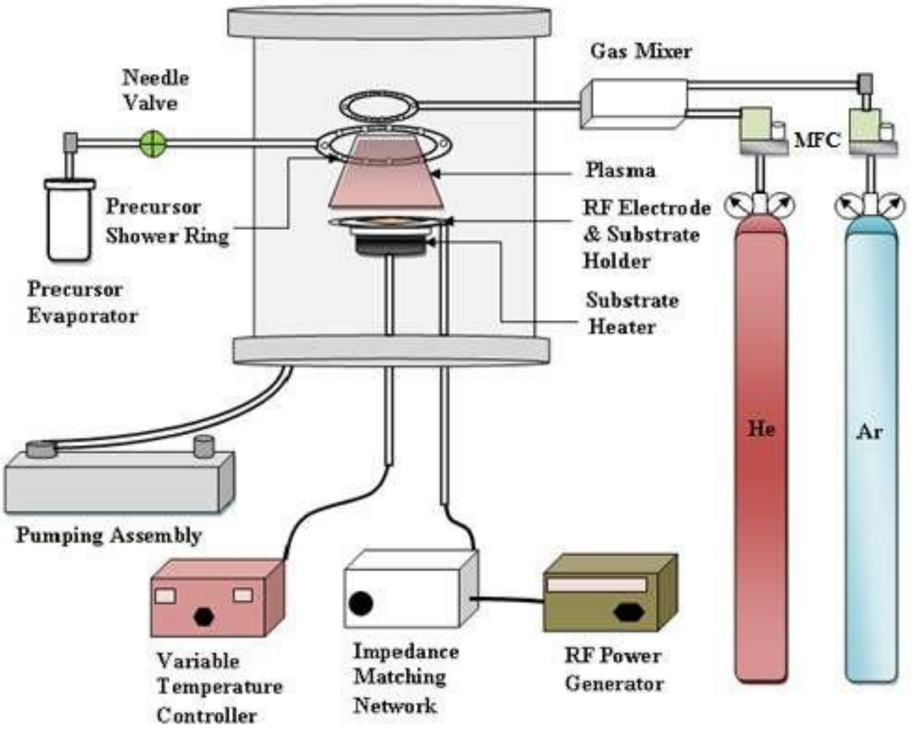

Figure 2.1: Schematic of the RF-PECVD experimental set up.

change. The role of the automated impedance matching network then is to act instantaneously to match the impedance of the RF power supply with plasma system so that maximum power transfer can take place. This automated impedance matching network is an important component of the RF-PECVD system for stable plasma generation and energy efficient deposition.

For this study, all the deposition runs have been carried out at an elevated substrate temperature 400°C. A substrate heater is installed directly below the substrate holder, whose temperature is controlled by a programmable temperature controller. The live substrate holder is insulated from the grounded substrate heater by an annular ceramic disc placed just beneath it. The annular shape of the disc ensures efficient transfer of heat from substrate heater to the substrate holder with minimum heat loss. Argon (Ar) and Helium (He) were chosen as process gases. Ar has been used for sputter cleaning of the substrates before each deposition run and He have been used as plasma medium during deposition. During our initial optimization of the process parameters, Ar was being used as process gas both for sputter cleaning and deposition. However, bombardment of the highly energetic Ar ions on the surface of the growing film enhanced re-sputtering rate of the deposited films, prompting us to use He as process gas. Laboratory grade Argon (Ar) and Helium (He) gases were fed into the chamber through mass flow controllers (MFCs). Gas flow rates were optimized to achieve the desired chamber pressure during sputter cleaning of the substrate and deposition runs as well. The gases were released inside the chamber through a hollow, perforated gas shower ring to ensure uniform distribution of the gases inside the chamber.

A solid state precursor ortho-carborane (o-$C_2B_{10}H_{12}$) was chosen for deposition of the $^{nat}B_xC$ thin films. Significant increase in saturated vapor pressure of the precursor with increase in temperature (from 665 Pa at 100°C to 4×10^3 Pa at 150°C) eliminated the necessity of carrier gases, to carry the precursor vapor into the chamber [55]. The solid precursor was converted into vapor inside a stainless steel precursor bubbler, wrapped with a heating tape on the outer surface. Operation of the heating tape was controlled using a programmable temperature controller and the heating schedule for the precursor was optimized on the basis of Thermogravimetric analysis (TGA) results and also experimental investigation. In TGA, mass of the sample is measured over time as temperature changes giving evaporation rate of the material at different temperature and pressure regime. Details of the chemical structure of the precursor and the TGA results are discussed in the next sub-section. Precursor vapors were transferred from the precursor bubbler to the deposition chamber through a precursor delivery line. A gate valve situated between the precursor bubbler and delivery line enables control of flow of the precursor vapor. Entire precursor delivery line was wrapped with heating tape to prevent solidification of vaporized precursors before reaching the deposition chamber. Precursor vapor was distributed inside the chamber through a precursor shower ring placed just above the substrate holder to facilitate uniform distribution of the precursor into the plasma discharge. The precursor shower ring along with the plasma reactor wall forms the ground electrode. When RF power is applied between the live and ground electrode, plasma is triggered and a instantaneous “DC self-bias” is developed in the powered electrode, which plays a pivotal role in deposition process of ^{nat}boron carbide thin films. Origin and importance of this “DC self-bias” have been discussed in detail in section 1.5.2.1.

2.1.2 Experimental set-up for Pulsed Laser Deposition (PLD):

As a part of the present thesis, we have compared various physical, chemical, and structural properties of ^{nat}boron carbide thin films deposited by one CVD and one PVD technique, namely PECVD and PLD, respectively. PLD was chosen among other available PVD techniques in view of its associated advantages, and relevance for deposition of thin films of a variety of materials including B_4C [22, 79]. In PLD, a pulsed laser beam is focused on a target which induces heating of the target. Subsequent increase of target temperature causes evaporation of molecules and atoms from the target in the form of a vapour plume. The dense plume from the target expands in vacuum and reaches the substrate held perpendicular to the plume, causing deposition of target vapour on the substrate surface. PLD ensures stoichiometric integrity of the material when deposited from target to the substrate; the process is reproducible, and can be precisely controlled. Simplified schematic of a PLD system is shown in Figure 2.2. For this study, ^{nat}boron carbide films were prepared via PLD technique in a stainless-steel deposition chamber under a vacuum of 10^{-5} mbar. Commercially available 99.9% pure $^{nat}B_4C$ pellet of diameter around 18 mm and thickness of 6 mm was used as target which was mounted on a rotating target holder. The target was irradiated with laser pulses from a Nd:YAG laser having a second harmonic wavelength of 532 nm with pulse duration of 6 ns, and laser pulse repetition rate of 10 Hz. Laser beam of

200 mW average laser power was focused on the target using a lens of 50 cm focal length, the spot area was measured on a thermal paper at the target surface to be $1.24 \times 10^{-3} cm^2$. The laser fluence was ~$15\ J/cm^2$ on the target. The laser beam was focused on the target surface at an angle of 45° in order to restrict spatial overlap between the incident laser beam and the generated vapor plume. Ultrasonically cleaned Si (100) wafers having an area around $1\ cm^2$ were used as substrates which were mounted on a substrate holder, equipped with a substrate heater, capable of raising substrate temperature up to 800°C. Distance between the target and the substrate was kept constant at 4.5 cm. The deposition was done for 36,000 laser shots on the target which corresponds to a duration of 60 minutes.

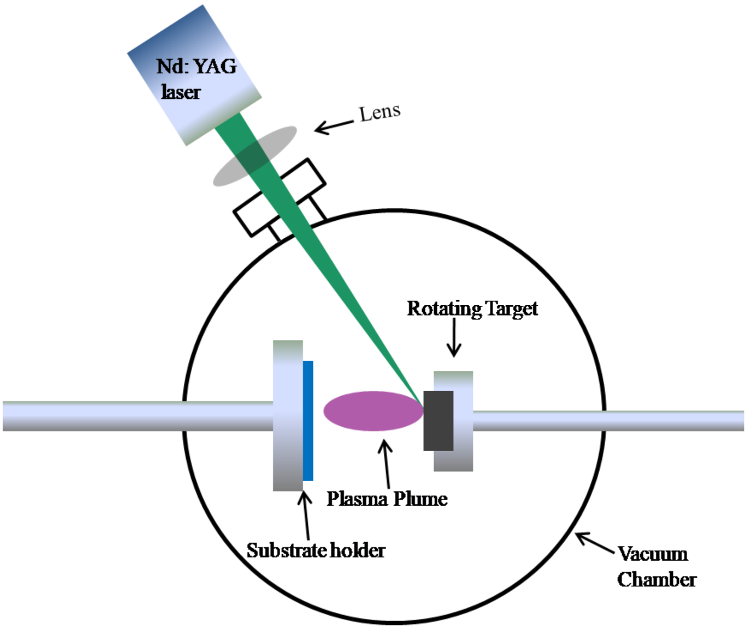

Figure 2.2: Schematic of a pulsed laser deposition system.

2.2 Precursor for PECVD:

A variety of precursors have been utilized earlier for synthesis of ^{nat}boron carbide thin films via PECVD technique over the years (discussed in detail in section 1.5) and a consolidated list of such precursors is given in Table 2.1. Ortho-carborane (o-$C_2B_{10}H_{12}$) was chosen as precursor in this study for its relative non-toxicity as compared to other available precursors. Some of the precursors show explosive behavior; some of them being flammable, self-ignite upon contact with air and therefore require special safety measures for handling in the laboratory. Ortho-carborane is not explosive or easily flammable, hence suitable for easy handling in the laboratory.

Table 2.1: List of precursors used for deposition of boron carbide thin films via PECVD.

Serial No.	Precursor	Limitation
1.	BCl_3+ CH_4+H_2	Toxic and Explosive
2.	BCl_3+ CCl_4+H_2	
3.	BCl_3+ C_7H_8+H_2	
4.	B_2H_6+ CH_4+H_2	
5.	B_2H_6+ CH_4	
6	BBr_3+ CCl_4+H_2	
7.	$B(CH_3)_3$	Flammable, self-ignite upon contact with air.
8.	$B_{10}H_{14}$	Toxic.
9.	BH_3NH_3	Leaves a significant amount of residue.

2.2.1 Chemical Structure of o-carborane:

Ortho-carborane, also referred as o-carborane (o-$C_2B_{10}H_{12}$) is an organo-boron compound having an icosahedral caged structure. Chemical structure of o-carborane is shown in the Figure 2.3 [80]. In the figure, red colored spheres represent 10 boron atoms, black spheres represent 2 carbon atoms and white spheres represent 12 hydrogen atoms. The prefix “ortho” in the chemical name of the precursor comes from the relative position of the carbon atoms in the structure. When the carbon atoms are situated at two adjacent sites in the carborane structure, it is called “ortho-carborane”. Its chemical nomenclature is 1, 2-

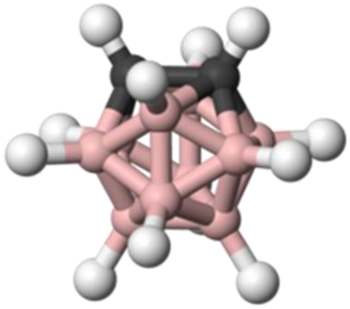

Figure 2.3: Chemical structure of the precursor ortho-carborane (o-$C_2B_{10}H_{12}$).

Dicarbadodecaborane. This carborane is also available in “meta” and “para” isomers having chemical nomenclature 1,7-Dicarbadodecaborane, and 1,12-Dicarbadodecaborane respectively. Organic compounds having caged structure are generally difficult to break. In plasma medium, the icosahedral cages of the precursor are either partially broken or sometimes remain intact. Favorable chemical reaction of this partially fragmented precursor gives rise to the distinct network covalent structure of boron carbide (section 1.2, chapter 1). The o-carborane used in this study possesses natural isotopic abundance of boron i.e. 19.2% ^{10}B and 80.8% ^{11}B atoms.

2.2.2 : Thermogravimetric analysis (TGA) of the precursor:

Thermogravimetric analysis (TGA) plot for o-carborane (o-$C_2B_{10}H_{12}$) precursor is shown in Figure 2.4. The figure shows apparent initial mass gain due to a common phenomenon called “buoyancy effect” [81]. The plot indicates that the solid precursor starts vaporizing at ~ $150°C$ and almost 90% of the precursor is vaporized at ~ $200°C$. However, the vaporization of the precursor showed a different behaviour during deposition runs. The TGA test was performed at ambient pressure in Ar environment. However, actual deposition experiments were carried out at much lower pressures. The precursor was found to start evaporating around $64°C$ at 0.200 mbar chamber pressure and at $75°C$, the rate of evaporation was highest. For our deposition runs, precursor heating schedule was determined

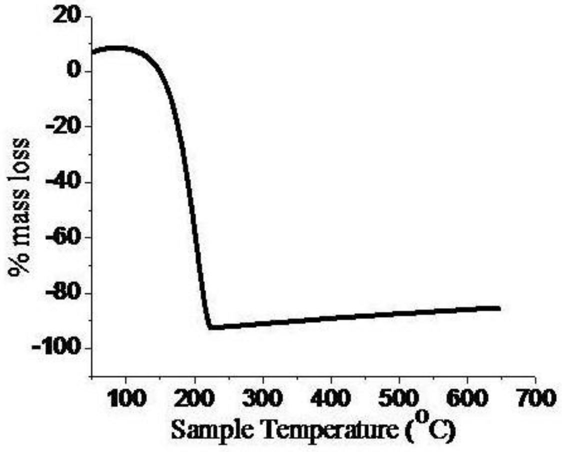

Figure 2.4: Thermogravimetric analysis (TGA) plot for o-carborane (o-$C_2B_{10}H_{12}$) precursor.

accordingly. First the precursor bubbler temperature was increased till $60°C$ at the rate $3°C/ min$ and then to $80°C$ at almost $1 / 2\ °C/min$, to ensure gradual release of the precursor vapour. Nonetheless, the initial TGA results shown in Figure 2.4 confirmed suitability of the precursor for our PECVD experiments.

2.3 Substrate cleaning methods:

In our study multiple substrates have been used for deposition of boron carbide thin films such as: Si (100), SS 316, Aluminium, and sodalime glass. Motivation behind the choice of substrates was guided by two factors: (i) suitability of the substrates for desired application, and (ii) ease of characterization in some cases. The main objective of surface cleaning in thin film deposition is to provide a pristine surface for deposition of adherent thin films. The cleaning processes must be simple, effective, and economical in order to meet the processing requirements. Therefore, researchers have developed a well-defined processing sequence for each type of substrate material.

Si (100): These substrates were cleaned thoroughly before each deposition run for removal of organic, ionic, and oxide contaminants. The cleaning process comprises of solvent clean, RCA-1, and HF dip method. First the samples were kept in acetone bath inside a glass beaker and ultrasonicated for 5-10 minutes. Acetone removes oils and organic residues from the substrate surface. But acetone tends to leave its own residue; hence the samples were then ultrasonicated in another solvent, typically isopropyl alcohol in a separate container. This method of cleaning is called “double solvent method”. After that the samples were ultrasonicated in de-ionized (DI) water, followed by drying in air before commencement of RCA-1cleaning process. RCA-1 cleaning method is generally utilized to remove organic residues from the surface of silicon wafers. The RCA-1 cleansing solution consists of 5 parts of water (H_2O), 1 part 27% ammonium hydroxide (NH_4OH), and 1 part 30% hydrogen peroxide (H_2O_2). Silicon wafers were dipped in the solution for $10 - 15$ minutes and then rinsed thoroughly in DI water. Completion of the process oxidizes the surface of silicon and leaves a thin oxide layer on the surface of the wafer. HF dip is then used to remove this oxide layer. For this process, 2% HF solution is required. Proper protective gears must be used as HF is a dangerous and toxic chemical. Plastic containers are used for dipping of silicon substrate as HF tends to attack glassware. The wafers were dipped in the 2% HF solution for 30 seconds and cleaned thoroughly under running DI water. Removal of oxide layer was checked by a simple wetting test. Silicon oxide is hydrophilic and pure silicon is hydrophobic, a non-wetting surface implies removal of oxides. To check the hydrophobicity, a drop of DI water is poured on the surface. If the water droplets beads up and roll of, the surface of the wafer is free from oxides. After that, the substrates were dried under infra red (IR) lamp and were ready for use.

SS 316: Stainless steel substrates were cleaned by double solvent method, similar to silicon substrates for removal of oil, and organic impurities. Samples were first ultrasonicated in acetone bath for 5-10 minutes followed by ultrasonication in isopropyl alcohol. Solvents were then removed from the substrate by thorough cleaning in DI water before drying under an IR lamp. No further sample cleaning was done for SS substrate.

Aluminium: Aluminium substrates must be chemically or electro-chemically cleaned before using in any deposition run. Surface cleaning is required to remove residual mill oil, smut, and surface oxides; in some cases near-surface disturbed layer (surface asperities) so as to provide a uniform/ smooth surface for deposition. For our study, substrates were cleaned by immersing them in an alkaline solution of potassium hydroxide (KOH) at a temperature of $70\ ^{\circ}C$ for 20 seconds. After the alkaline etching, substrates were first thoroughly cleaned in DI water followed by ultrasonication in the same. An IR lamp was used to dry out the substrate before loading in the deposition chamber.

Sodalime glass: These substrates were also cleaned by double solvent method, first by ultrasonication in acetone for 5-10 minutes, followed by ultrasonication in isopropyl alcohol. Substrates were then thoroughly cleaned in DI water and dried under the IR lamp before deposition.

All the samples were sputter cleaned in Ar plasma at -200V substrate self-bias before each deposition run. Depending upon the type of the substrates, the duration of sputter cleaning was kept between 10-20 minutes. Sputter cleaning is preferred in thin film deposition to ensure complete removal of traces of oxides, and other impurities. A pristine substrate surface improves inter-diffusion, and improves the thin film-substrate adhesion significantly.

2.4 Characterization techniques:

In this study, several characterization techniques have been employed to investigate various physical properties of the $^{nat}B_xC$ thin films and their dependence on structure, chemical composition, and surface morphology. Surface and bulk chemical composition of the films was probed by X-ray Photoelectron Spectroscopy (XPS), and Proton Elastic Backscattering Spectrometry (p-EBS), respectively. Thickness and roughness of the films were measured with 3D Optical Profilometry. Chemical bonding information of the films was extracted via Fourier Transform Infra-Red Spectroscopy (FTIR). Film structure was probed via X-ray Diffraction (XRD) technique. Surface morphology was investigated by Scanning Electron Microscopy (SEM), and Field emission SEM (FESEM) technique. Tribological properties were determined in a reciprocating tribometer and hardness was measured via Knoop Hardness test. In addition, Neutron Transmission Measurement was performed in an experimental nuclear reactor. All the characterization techniques used in this study are consolidated and listed in Table 2.2.

Table 2.2: List of characterization techniques and their utility.

Serial No.	Characterization Technique	Utility
1.	3D optical profilometry	Non-destructive technique to extract information about thickness, roughness and 3D contours of wear volume.
2.	X-ray photoelectron spectroscopy (XPS)	Surface sensitive technique (≤10 nm). Information about elemental composition, chemical state, electronic state, binding energy, layer thickness.
3.	Proton elastic backscattering spectrometry (p-EBS)	A non-destructive bulk technique for compositional analysis. Quantitative information about atomic percentages of elements, elemental depth distribution and layer thickness.
4.	Fourier transform infra-red spectroscopy (FTIR)	Non-destructive technique for identification of different infrared absorption bands.
5.	X-ray diffraction (XRD) and Grazing angle XRD (GIXRD)	Non-destructive technique. Utilized to identify crystalline structure, grain size and stresses in the thin film or bulk material.
6.	Scanning electron microscopy (SEM) and Field emission SEM (FESEM)	Provides information about materials' microstructure, morphology, uniformity and dimension. Non-destructive technique.
7.	Spectrophotometry	Optical properties: refractive index, extinction co-efficient, absorption co-efficient and band gap

		(direct and indirect) can be investigated from optical transmission or reflection spectra.
8.	Soft X-ray reflectivity measurement	Non-destructive technique, suitable for study of surface and interfaces of thin films and multilayers. Provides precise information about the roughness of the interfaces of low Z elements.
9.	Neutron transmission measurement	Information about the total neutron absorption cross section of a material.
10.	Knoop Hardness measurement	Hardness values of thin films.
11.	Scratch-adhesion testing	Critical load of adhesive failure and roughness can be identified. Various failure modes can be identified on the basis of optical micrographs and acoustic emissions.
12.	Tribological measurements in a reciprocating tribometer	Useful techniques to determine wear rate and lubricity of a material at different tribological stress conditions.

2.4.1 3D Optical Profilometry:

A 3D optical profilometer works on the principle of interference. When a reference light beam and the beam reflected from the sample surface undergo interference, fringes are formed due to path difference between these two beams. If during deposition, one part of the substrate is kept masked, during profilometry measurements, the substrate part and the sample part will generate interference fringes of different width due to change in wavelength of light in two different mediums. The interference fringes produced in the substrate side and thin film side are well separated as shown in Figure 2.5 (b). From the distance between the envelopes of the two fringe patterns, film thickness is measured using relevant software. In our study, during each deposition run, one of the samples was kept partially masked to facilitate thickness measurement of the deposited films. Profilometry measurements were

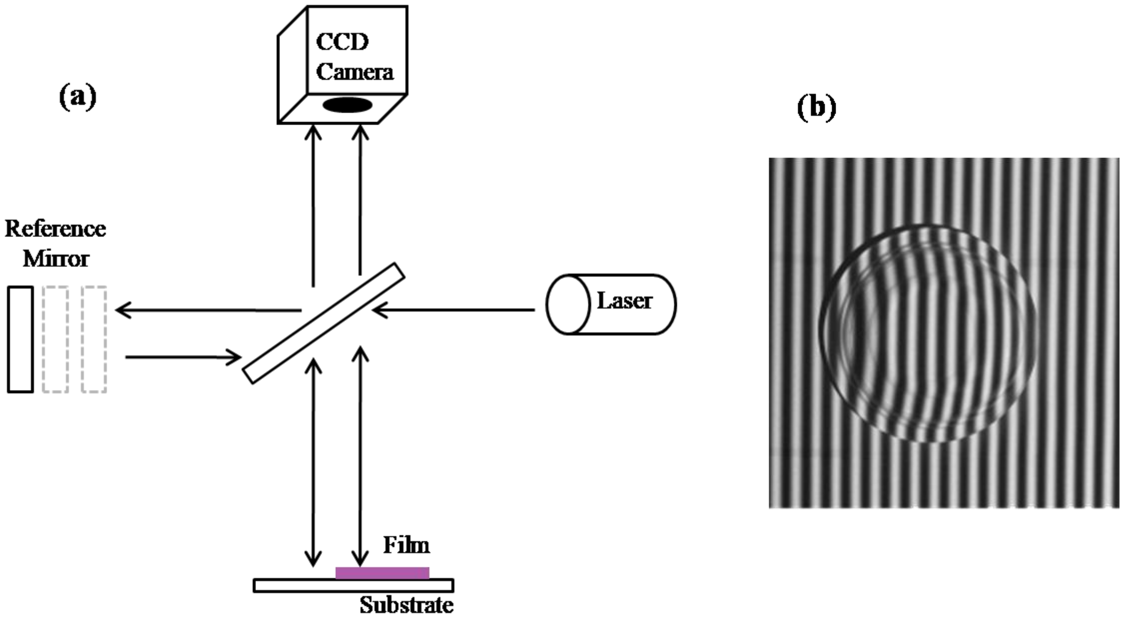

Figure 2.5: (a) Schematic representation of the principle of operation of optical profilometer and (b) Typical interference fringes generated on the sample having region of different thickness.

done using a Taylor Hobson 3D optical profilometer (Green light ($532\,nm$), resolution 0.1 Å).

2.4.2 X-ray Photoelectron Spectroscopy (XPS):

XPS is a widely used surface analysis technique to extract information about chemical state, and also the surface chemical composition for a wide range of materials. This technique can also be used for elemental depth analysis up to $5\,nm$, using specific arrangement (angle resolved XPS). XPS technique involves exciting the sample surface by mono-energetic soft X-ray source, for example AlK_α (1486 eV) or MgK_α (1258 eV). A crystal monochromator is used to reduce the energy spread of the X-ray source. Core-level photo electrons emitted from the sample are then detected in an electron energy analyzer. The resultant information is intensity versus electron binding energy/ kinetic energy. From the binding energy and the intensity of a photo-electron peak, the identity of elements, quantity and chemical state of a constituent element can be determined. XPS instrument is capable of operating in two modes:

(i) Survey scan, which is useful for elemental identification, and (ii) detailed scan, useful for quantitative measurement. Simplest schematic of the XPS arrangement is shown in Figure 2.6.

The kinetic energy of a detected photo-electron can be written as,

$K.E. = h\nu - B.E. - \emptyset$ ………………………..(2.1)

Where, $h\nu$ = Energy of incoming X-ray photons, $B.E.$ = Binding energy of core electrons of individual elements, and $\emptyset$ = Work function of the detector.

In our study, ex-situ XPS analysis on the boron carbide films was performed using a VG make model CLAM-2 hemispherical analyzer with MgK_α source (1253.6 eV). Survey scans were performed with step size of 0.1 eV. Detailed scans were taken with pass energy 50 eV to acquire the electron spectra of boron (B 1*s*), carbon (C 1*s*) and oxygen (O 1*s*) in the deposited films.

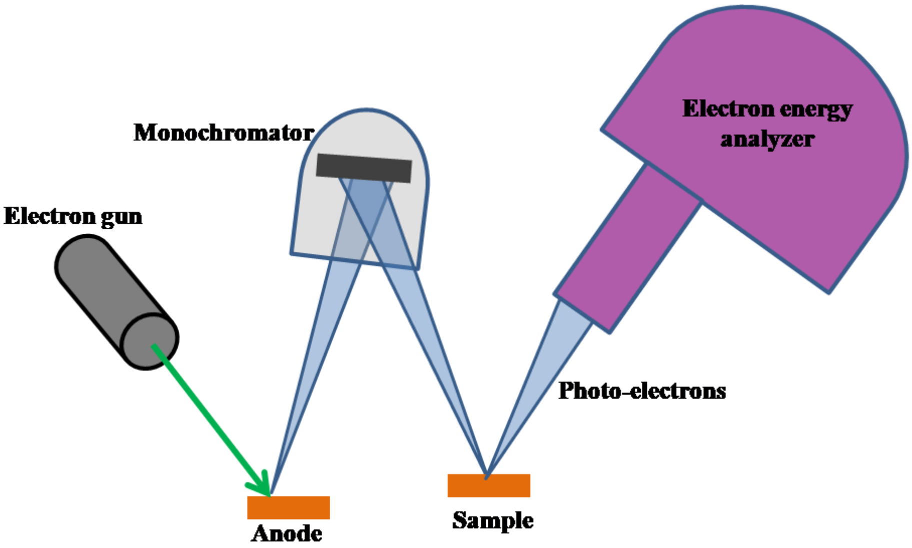

Figure 2.6: Schematic representation of the experimental arrangement for X-ray photoelectron spectroscopy (XPS).

2.4.3 Rutherford Backscattering Spectrometry (RBS)/ Proton Elastic Backscattering Spectrometry (p-EBS):

RBS or p-EBS is the most popular non-destructive nuclear analytical technique for compositional thin film analysis (nm-μm) as well as elemental depth analysis. In this method, a highly energetic beam of ions, generally H^+ or He^+ is directed towards the sample under investigation, and the energy distribution, and yield of the backscattered ions are measured at large angles. Since the backscattering cross section of each individual atom is different, it is possible to extract information about both the atomic mass, and concentration of the constituents of the sample. The detection limit of this method is about $10^{11} - 10^{15}\ atoms\ cm^{-2}$. In addition to the elemental composition, this technique can provide information about the crystalline quality, and purity of single crystals via a process called “channeling”. Only drawback of this technique is that light elements like hydrogen (H) and Helium (He) cannot be investigated. Elastic Recoil Detection Analysis (ERDA) is used to

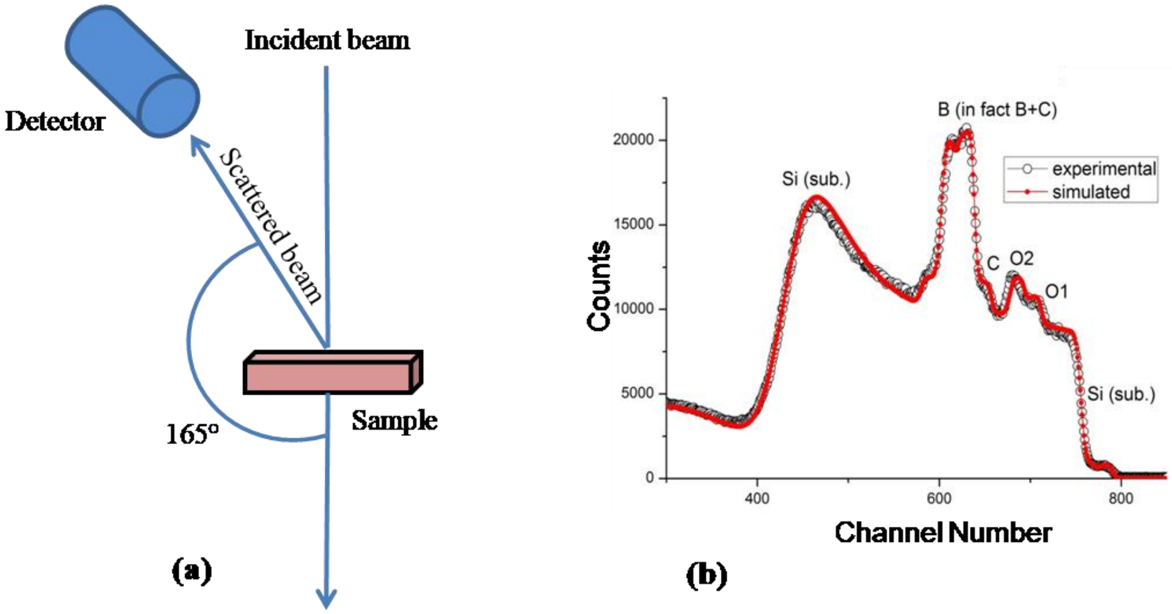

Figure 2.7: (a) Schematic representation of the proton elastic backscattering spectrometric technique and (b) Typical p-EBS spectra of boron carbide samples.

measure concentration, and depth profile of light elements like H and He atoms. The basic schematic of p-EBS experimental arrangement is shown in Figure 2.7 (a).

A typical p-EBS spectrum is shown in Figure 2.7 (b). Separation between the peaks corresponding to different elements depends on the kinematic factor of elastic scattering given by:

$$k = \left[\frac{\sqrt{M_2^2 - M_1^2(\sin\theta)^2} + M_1\cos\theta}{M_2 + M_1}\right]^2 \quad \ldots\ldots\ldots\ldots\ldots\ldots\ldots\ldots(2.2)$$

Where, $M_1 =$ mass of the incident nucleus, $M_2 =$ mass of the target nucleus, and $\theta =$ angle of scattering. Intensity of the peaks depend on the differential scattering cross section given by,

$$\frac{d\sigma}{d\Omega} \equiv \sigma(\theta) = \left[\frac{Z_1 Z_2 e^2}{4E\left(\sin\frac{\theta}{2}\right)^2}\right]^2 \quad \ldots\ldots\ldots\ldots\ldots\ldots\ldots\ldots\ldots\ldots\ldots(2.3)$$

Where, $Z_1 =$ atomic number of the incident nucleus, $Z_2 =$ atomic number of the target nucleus, $e =$ charge of an electron, $E =$ energy of the incident particle.

Area under each peak gives the concentration of the corresponding element. The peak width, and peak shift gives the thickness of the films.

2.4.4 Fourier Transform Infra-red Spectroscopy (FTIR):

FTIR spectroscopy is a technique for obtaining infrared absorption or emission spectra of solid, liquid, or gas. FTIR spectrometer simultaneously collects high-spectral-resolution data over a wide spectral range. In FTIR technique, with the principle of Michelson’s interferometer, a beam of light is generated containing the information over the desired frequency range. An interferogram is then generated which is further directed towards the sample. This beam when detected after passing through the sample provides information about absorption of light for the entire frequency range at once. Fourier Transform of this data is performed to convert the measured absorption as a function of displacement of the

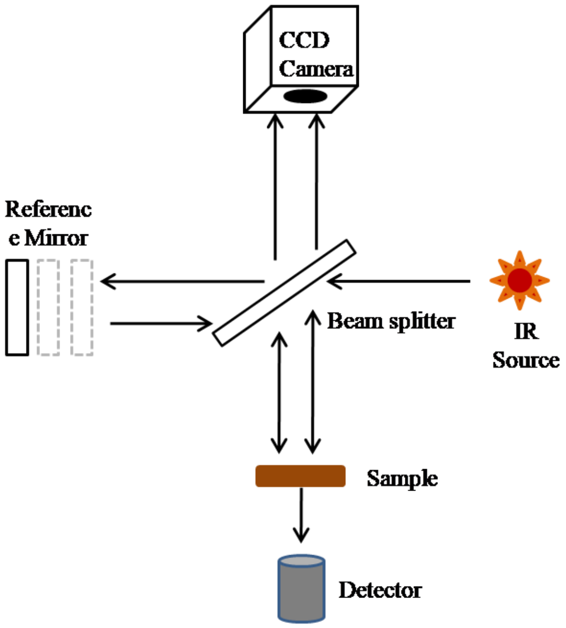

Figure 2.8: Schematic representation of the Fourier Transform Infra-Red (FTIR) Spectroscopic technique.

mirror position (cm) into its inverse domain i.e. absorption at different wavenumbers (cm^{-1}). Schematic of a typical experimental arrangement for FTIR is shown in Figure 2.8. In our study, Infrared spectra were recorded using a Bruker Vertex 80V FTIR spectrometer in the mid-IR region, having a resolution of 4 cm^{-1}.

2.4.5 X-ray diffraction (XRD):

XRD is a non-destructive rapid analytical technique for phase identification. It provides information about unit cell dimension, grain size, and internal stresses within a material. XRD utilizes the constructive interference of X-rays diffracted from the crystalline samples to extract the required information. Constructive interference occurs when the superposed waves satisfy Bragg's law of diffraction (equation 2.4) which states that, when a X-ray of wavelength (λ) is incident on a material surface having inter-planar spacing d (1-

100Å), constructive interference between diffracted rays provides maximum intensity at angle of incidence θ, called the Bragg's angle.

$$2d \sin\theta = n\lambda \text{ ……………………………………}(2.4)$$

To satisfy the Bragg's law, the wavelength of the incident radiation should be similar to inter-planer spacing of the sample. X-ray diffractometers consist of three basic elements: one X-ray tube, a sample stage, and an X-ray detector. For bulk material, usually Bragg-Brentano reflection geometry is used in XRD, where angle of incidence equals to the angle of diffraction with respect to the sample surface. If the angle of incidence is high, X-rays can penetrate to the depths of few to several hundred micrometers inside the material. For thin film analysis, beam penetration depth should not be greater than the film thickness, otherwise diffraction pattern predominantly records substrate peaks. A grazing incidence configuration (GIXRD) for the incoming beam can minimize the contribution from the substrate. In this technique, a collimated beam of monochromatic X-rays is directed towards the sample at grazing angle ($< 2 - 3°$) and the diffraction profile is recorded by scanning the detector at different angles. In our study, XRD was performed in Bragg-Brentano geometry (θ -2θ geometry) with 2θ angle in the range of 20°-30° in angular steps of 0.02° using CuK_α (λ=1.5406 Å) radiation in angular steps of 0.02°. Grain size was also calculated from XRD peaks using Scherrer's equation given by:

$$D_p = \frac{0.94\lambda}{\beta \cos\theta} \text{ ………………………………………}(2.5)$$

Where, $D_p =$ average crystallite size, $\beta =$ full width half maximum (FWHM) of the most intense peak, $\theta =$ Bragg's angle in radian, and $\lambda =$ X-ray wavelength. To calculate grain size, the most intense peak of the XRD patterns of ^{nat}boron carbide films was considered. GIXRD data was recorded at an angle of incidence 0.6 degree. Simplest schematic of XRD arrangement is shown in Figure 2.9.

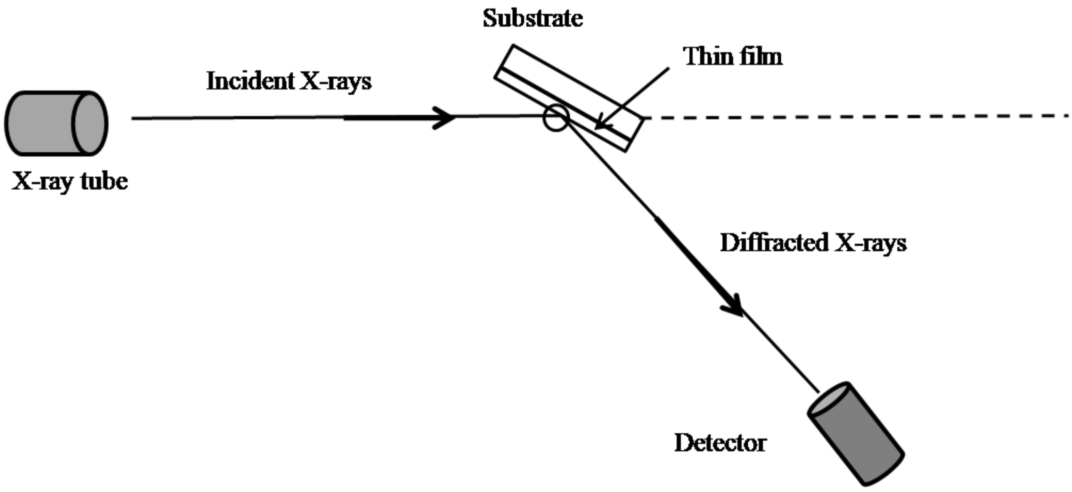

Figure 2.9: Schematic representation of the X-ray Diffraction technique.

2.4.6 Scanning Electron Microscopy (SEM):

SEM is an important electron microscopic technique for determination of nanostructures of materials, and surface morphology of thin films. SEM image of a sample surface is acquired by scanning it with a focused beam of electrons. Due to the focusing of the electron beam, SEM instruments have a large depth of field which results in a characteristic three-dimensional image of the sample. SEM instruments are available in a wide range of magnifications, from about 10 times to more than 500,000 times with a resolution better than 1 nm. Figure 2.10 shows a simplified schematic of the instrument [82]. Electron beam is generated by heating a filament (thoriated tungsten, LaB_6 or a field emission based source) which acts as the cathode, emitting electrons with energy $\sim 20-40 keV$, depending on the filament current. Emitted electrons are then attracted towards the positively biased annular anode, through which the accelerated electron beam reache the condenser lens system. Condenser lenses are electromagnetic lenses which focus the beam in the vicinity of the objective lens system. A pair of deflection coils, placed in between the objective lens and condenser lens helps to scan the beam on the sample surface in X-Y direction, in a raster-like pattern. The electrons that are reflected or knocked off the near-

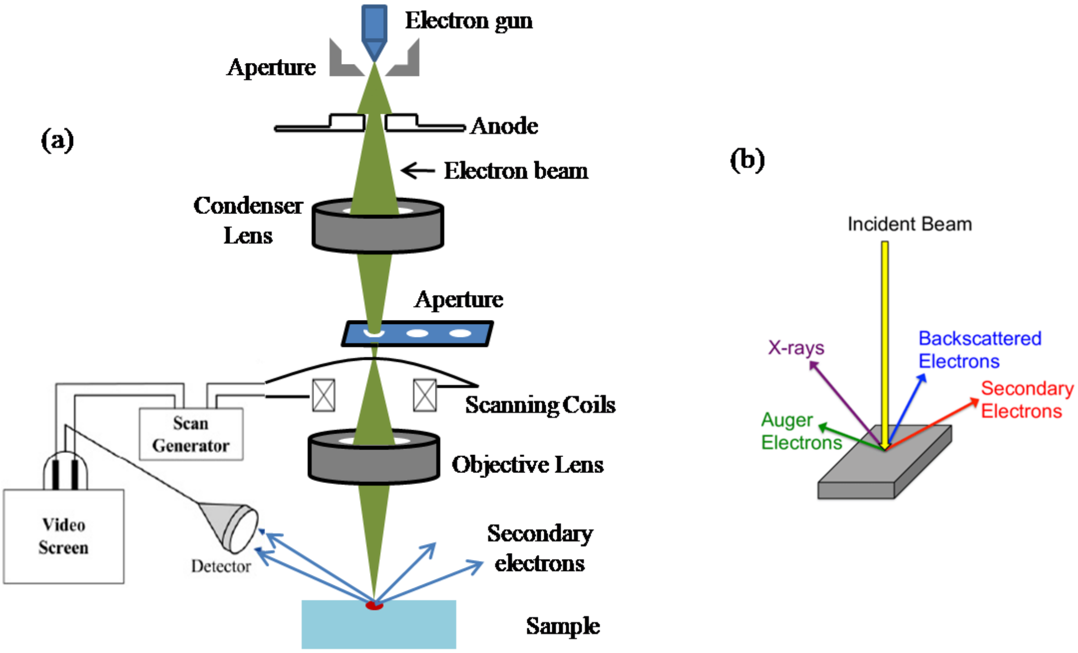

Figure 2.10: Schematic of (a) typical Scanning Electron Microscope (SEM) and (b) sample-electron beam interactions within a SEM.

surface region of a sample are used to form the image. Electron interaction with the material leads to elastic and inelastic scattering. Inelastically scattered secondary electrons (energy ~ 50 eV) are detected for imaging via surface micrographs. Elastic scattering produces backscattered electrons which are useful for generation of surface micrographs with atomic number contrast. Characteristic X-rays are also produced, which are analyzed to obtain the elemental composition of the sample. It is easier to record SEM micrograph for conducting samples. For insulating materials, electron accumulation on the sample surface leads to ‘charging effect’ which makes surface imaging difficult and unreliable. To overcome this constraint, insulating samples are coated with a thin layer (~ 5nm) of conducting material so that accumulated electrons can flow through the top surface but can also penetrate the thin layer to provide information about the specimen. In this study, one desktop mini scanning electron microscope (SEM) (Model SNE 3000M, SEC engineering, Korea) and one field emission scanning electron microscope (FESEM) (make-Zeiss, model-Supra) were employed to investigate surface morphology of the deposited films.

2.4.7 Ultraviolet-Visible (UV-VIS) Spectrophotometry:

Spectrophotometry is a branch of spectroscopy for quantitative measurement of absorbance or transmission of light in a material as a function of wavelength. Modern spectrophotometers cover a wide range of electromagnetic spectrum starting from X-ray, ultraviolet, visible, infra-red, and microwave. With the help of this technique one can determine the intrinsic optical properties such as refractive index, extinction co-efficient, direct, and indirect optical band-gap. For thin films, the thickness of the films can also be measured. A UV-Visible spectrophotometer usually consists of a white light source which is collimated before incidence on the sample surface. The transmitted/ reflected light beam from the sample is then passed through a slit to remove off-axis rays, and then using a mirror it is directed towards a grating/ combination of gratings to separate different wavelengths. The detector placed after the grating records light intensity at different wavelength. Simplest schematic of the experimental arrangement is shown in Figure 2.11. In our study, optical transmission spectra of the films were recorded using a UV-VIS-NIR spectrophotometer (UV-3101PC, SHIMADZU) in the range 200 nm–1200 nm to determine refractive index (n), extinction co-efficient (k), absorption co-efficient (α), optical band gap (E_g), and film thickness (t) of the deposited ^{nat}boron carbide thin films. Determination of the optical constants from recorded transmission/ reflection spectra needs involved analysis using specific model for the thin film-substrate system. Details of the data analysis have been included in the subsequent chapters.

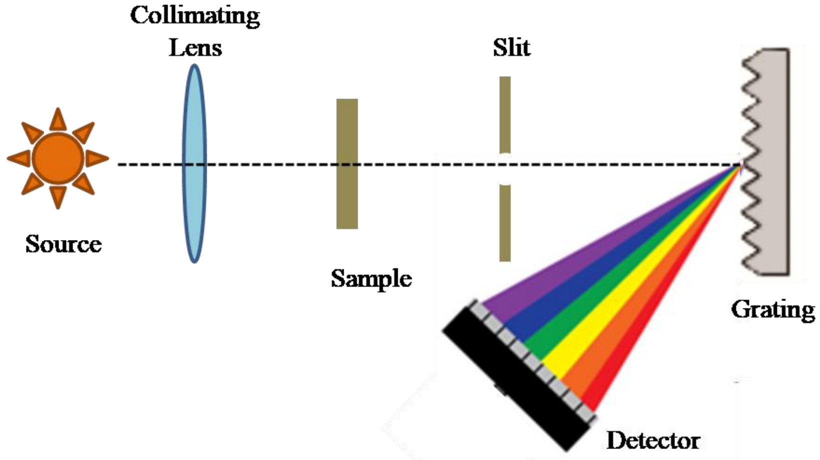

Figure 2.11: Simple schematic of a UV-VIS spectrophotometer.

2.4.8 Soft X-ray Reflectivity:

Soft X-ray reflectivity measurement is a powerful technique to probe interfacial structural phenomena in single layer, multi-layer, and nano-structured films with the help of spectral and angular dependence of reflection co-efficient. This technique provides a direct measure of reflectivity of a material as a function of wavelength, and angle of incidence. Also, from the absorption edge spectra of different elements, precise quantitative analysis of the samples is possible. For thin films of any material to be useful as a single or multi layer component in optical coatings, it must have reasonable reflectivity as individual layer in the desired range of electromagnetic spectrum. Boron carbide films as optical coating in soft X-ray and Extreme Ultra Violet region are increasingly being investigated. Therefore, in our study, soft X-ray reflectivity of the boron carbide thin films were assessed in INDUS 1 beamline at Raja Ramanna Centre for Advanced Technology (RRCAT), Indore. Reflectivity of the samples was determined in the wavelength range 40 Å–360 Å at a fixed grazing angle 5°. A schematic of the experimental arrangement is shown in Figure 2.12. Here, soft X-rays from a synchrotron radiation source are focused on a toroidal grating monochromator with toroidal mirror based pre-focusing optics. Similar toroidal mirror is used in post focusing optics, once the X-ray photons comes out of the monochromator to focus the photon beam on

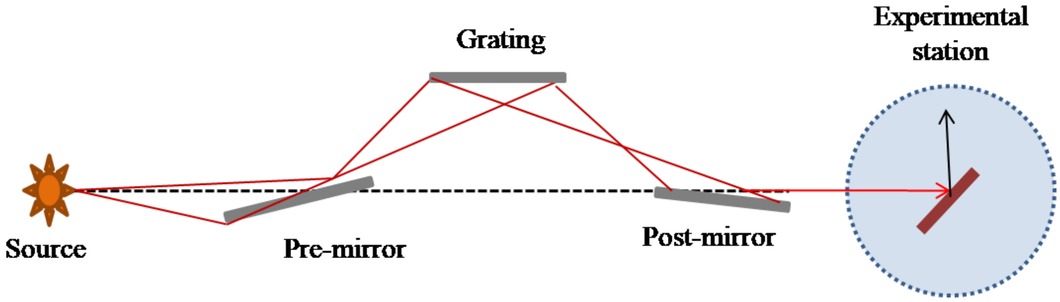

Figure 2.12: Schematic of Soft X-ray reflectivity measurement arrangement.

the samples kept in the experimental station. The experimental station of the beamline is a high vacuum reflectometer, capable of performing angle, and wavelength-dependent reflectivity measurements. In addition to reflectivity measurements, the beamline is also suitable for study of optical properties of materials (metals, semiconductors, thin films, multilayers, etc.) in VUV, and soft X-ray regimes.

2.4.9 Neutron Transmission Measurement:

Neutron transmission measurement was performed on the as-deposited ^{nat}boron carbide thin films to find out total macroscopic cross section (Σ_t) for neutron absorption. Measurements were performed using a fine collimated neutron beam from a research reactor (DHRUVA). For this particular measurement, ^{nat}boron carbide samples were deposited on 1 mm thick Aluminium substrates, as the % neutron absorption in Aluminium is less (1% of the incident neutron flux) than steel or other materials. The samples were mounted in between the neutron beam and a standard BF_3 gas filled neutron proportional counter. Films were exposed to a 2 mm diameter beam of 4Å neutrons having a neutron flux ~ 10^7 n/ cm^2/ sec at the reactor power of 90 MW. Intensity of the neutron beam was measured prior to incidence on the sample, and after passing through the sample as well. Total macroscopic cross section (Σ_t) was calculated from the following equations:

$I(x) = I_0 e^{-n\sigma x}$ ……………………………………(2.6)

Where, $I(x)$ = Intensity of the neutron beam after passing through the sample, I_0 = intensity of the incident neutron beam, n = number density of the material, σ = neutron cross section of the material and x = thickness of the material.

Equation (6) can be re-written as,

$I(x) = I_0 e^{-\Sigma_t x}$ ……………………………………..(2.7)

Where, Σ_t = total macroscopic cross section of the material which takes care of both absorbed and scattered neutrons. Simplified schematic of the experimental arrangement for neutron transmission measurement is shown in Figure 2.13.

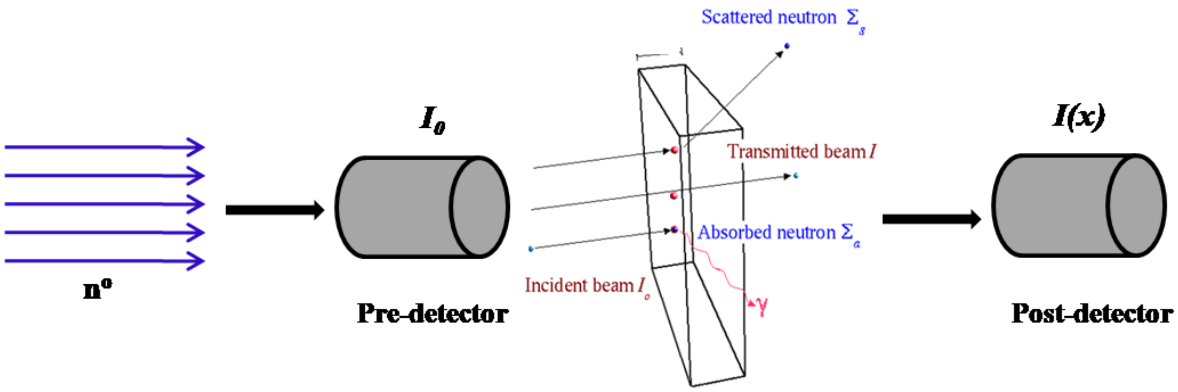

Figure 2.13: Schematic of the neutron transmission measurement set-up.

2.4.10 Hardness measurement:

Hardness of the deposited ^{nat}boron carbide thin films was measured by a Knoop's hardness indenter. Knoop hardness test is a microhardness test technique, used specifically for very brittle material to prevent cracking, and to facilitate hardness measurement for thin films. The indenter used in the Knoop hardness test is a pyramidal diamond similar to the one used in Vickers hardness test. However, instead of being symmetrical, the pyramid is elongated. The typical length to width ratio of this pyramidal indenter is 7:1 and respective face angles are 172 degrees for the long edge and 130 degrees for the short edge. The depth of the indentation can be approximated as $1/30^{\text{th}}$ of the long dimension. Schematic of the indenter's impression used for Knoop hardness measurement is shown in Figure 2.14 [83]. Knoop Hardness (HK) of a material/ thin film is ascertained by first measuring long diagonal of the indent impression with the help of an optical microscope, and then putting the measured value in the following equation:

$$HK = \frac{Load\ (kgf)}{Impression\ /area\ (mm^2)} = \frac{P}{C_p L} \ldots\ldots\ldots\ldots\ldots\ldots\ldots\ldots(2.8)$$

Where, L = length of the indentation along the long axis, C_p = correction factor related to the shape of the indenter, ideally 0.070279, P = applied normal load.

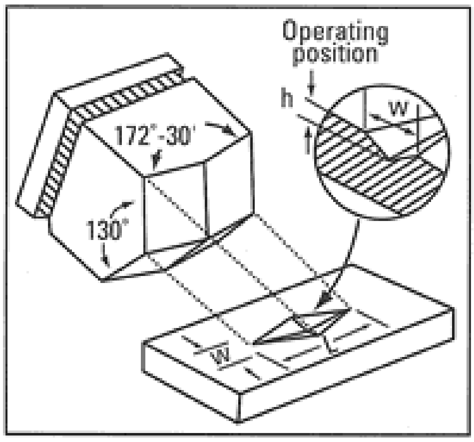

Figure 2.14: Schematic of the indenter and its impression on the sample surface during Knoop hardness measurement.

2.4.11 Scratch-adhesion test:

Scratch test is one of the most popular, fast, and effective method to assess adhesion properties of thin film coatings, and to identify different failure modes with associated critical load values (L_{ci}). On any sample, scratch-adhesion test can be performed in two modes: by applying either a linear progressive load or constant load. In Progressive Load Scratch Test (PLST) mode, a stylus indenter is moved over a specimen surface with a linearly increasing load until failure occurs at a certain critical load (L_{ci}) value. Magnitudes of Normal (F_z) and tangential force (F_x) are recorded. The failure events are usually examined with the help of an optical microscope. In addition, acoustic Emission (AE) can also be measured during the test.

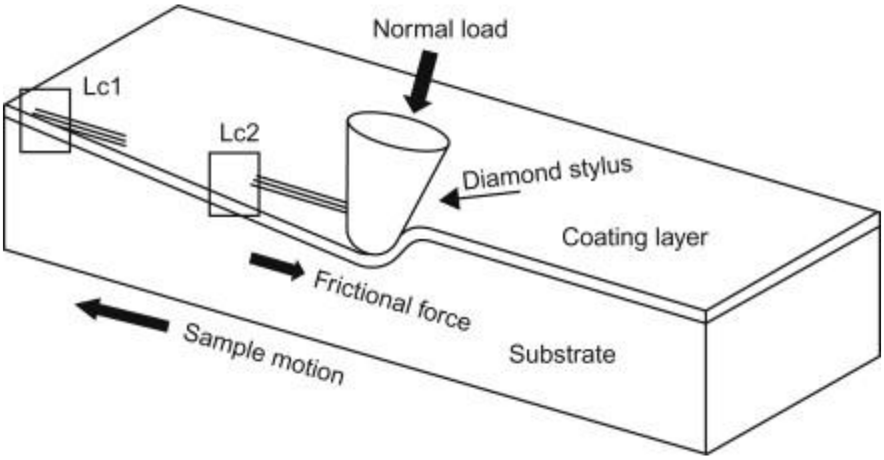

Figure 2.15: Schematic of the scratch-adhesion test for thin films.

L_c is primarily a function of thin film-substrate adhesion, stylus-tip radius, loading rate, coating thickness, and internal stress in films. Practical scratch-adhesion value is defined as the lowest critical load at which failure of thin films takes place. It is an important parameter related to thin film-substrate adhesion, useful for comparative evaluation of films. Schematic of the scratch-adhesion test set-up is shown in Figure 2.15 [84]. In this study, the tests were performed in PLST mode with starting contact load of 1 N, increased with time till 30 N for all the samples. The scratch length was 3 mm and the slide velocity of the applied normal load was 2 mm/ min. Optical micrographs of the scratch-tracks were also recorded using an optical microscope.

2.4.12 Tribological tests in a Reciprocating Tribometer:

Tribometer is a generic name for instruments used to measure frictional force between two surfaces under relative motion. It is also used to evaluate wear of bulk material and thin films. A large variety of tribometers are available for tribological characterization, two extensively used set up being Linear Reciprocating and Rotative (pin on disk or ball on disk) wear test technique. Friction and wear properties of any material are function of the external parameters such as: temperature, humidity, lubrication, and applied load. The purpose of using a tribometer is to provide a simulated environment where all the aforementioned factors can be carefully controlled and monitored to assess the wear and friction behaviour of a material, without facing the difficulties of carrying the experimentation on the original system. Schematic of a typical linear reciprocating tribometer is shown in Figure 2.16. The tribometer usually consists of a sample stage where the test samples are mounted steadily. The test sample is mounted against the counter sample in the pin or ball holder and a static normal load is applied to this test sample-counter sample system, either by adjustable weights or by pneumatic valves. During the test, the frictional force on the sample stage is measured in the horizontal direction. Transducers are used to measure the deflection at the point of contact due to surface irregularity or wear, which is then converted into desired data sets using a computer programme. In our study, wear and friction performance of the as-deposited ^{nat}boron carbide films were probed by a reciprocating tribometer using a conventional ball on disc configuration (TE-70, Phoneix Tribology Ltd, UK). Chrome steel was taken as counter-

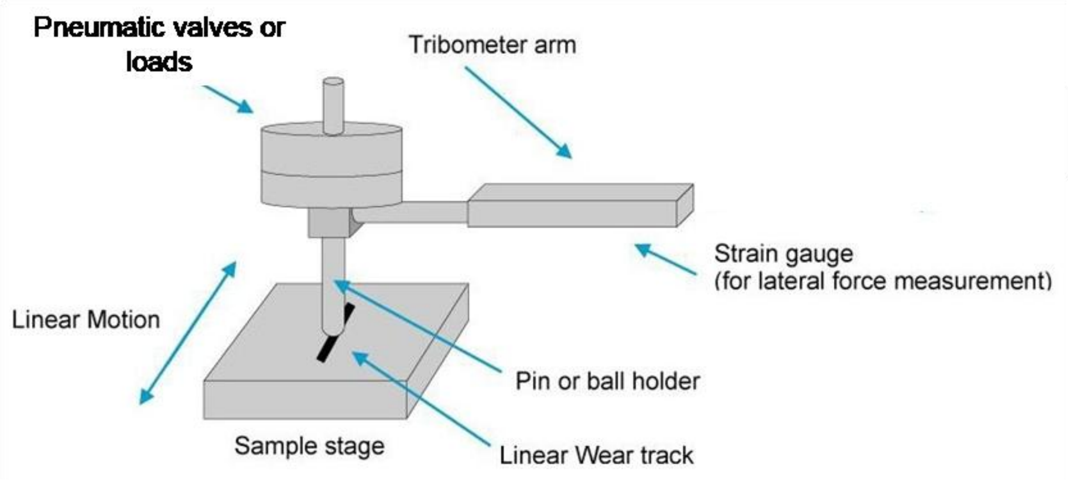

Figure 2.16: Schematic of a reciprocating tribometer arrangement.

face material. The stainless steel substrate -$^{nat}B_xC$ thin film coating system, and the chrome steel counterpart was subjected to relative oscillatory movement. Sliding tests were performed at ambience in dry lubricated conditions with relative humidity ~ 70% and temperature 27°C. Specific wear rate W_s was calculated from the following relationship,

$$W_s = \frac{V}{FL}\left(\frac{mm^3}{Nm}\right) \ldots\ldots\ldots\ldots\ldots\ldots\ldots\ldots\ldots\ldots (2.9)$$

Where, $L =$ total sliding distance, $F =$ applied normal load, and $V =$ volume of wear tracks.

The next four chapters encapsulate our important findings during investigation of the PECVD deposited ^{nat}boron carbide thin films using all the aforementioned characterization techniques.

Chapter 3 : Deposition of ^{nat}boron carbide ($^{nat}B_xC$) thin films and investigation of effect of self-bias on elemental composition, structure, and neutron absorption.

3.1 Introduction:

Boron carbide thin films have been increasingly investigated for their application in new generation neutron detectors owing to the high thermal neutron absorption cross section of ^{10}B atoms (3840 b for 1.8 Å neutrons, $1b = 10^{-24} cm^2$). ^{10}B atom undergoes neutron capture reaction $^{10}B(n, \alpha)^7Li$, enabling detection of neutrons.

$$^{10}_{5}B + ^{1}_{0}n \rightarrow ^{7}_{3}Li(0.84\ MeV) + ^{4}_{2}He(1.47\ MeV) + \gamma(0.48\ MeV)\ (94\%\ probability) \ldots\text{(3.1)}$$

$$^{10}_{5}B + ^{1}_{0}n \rightarrow ^{7}_{3}Li(1.02\ MeV) + ^{4}_{2}He(1.78\ MeV)\ (6\%\ probability) \ldots\text{(3.2)}$$

High cost and shortage of ^{3}He gas based conventional neutron detectors, and toxicity of BF_3 gas filled neutron proportional counter has necessitated a search for possible alternative materials for thermal neutron detection [8]. Boron carbide eventually emerged as an important material for nuclear industry. Boron carbide thin films can either be implemented as neutron conversion layer in traditional proportional counters or diode based detectors, or it can be used as the p-type or n-type material itself in the semiconducting diode neutron detectors. Neutron absorption in boron carbide thin films essentially depends upon the elemental composition of the film, majorly on the presence of ^{10}B atoms. Chemical and elemental composition of boron carbide films varies significantly with factors such as, deposition methods, external process parameters, and the choice of precursors used for deposition [4].

This chapter encapsulates our investigation on the DC self-bias developed on the substrate during RF-PECVD, and its effect on the bulk, and surface elemental composition of the films. Neutron absorption behavior of the deposited ^{nat}boron carbide films has also been studied as a function of film composition. For deposition of ^{nat}boron carbide thin films, o-carborane precursor (o-$C_2B_{10}H_{12}$) was used where the boron atoms were present in their natural isotopic abundance i.e. approximately 19.8% ^{10}B and 80.2% ^{11}B atoms. Therefore the deposited films are usually referred to as $^{nat}B_xC$ films in this study. Elemental composition were investigated by X-ray photoelectron spectroscopy (XPS), and proton elastic backscattering spectrometry (p-EBS). Fourier Transform Infrared Spectroscopy (FTIR) was performed to investigate different bonding environment of the constituent elements. Efforts have also been made to find out the chemical bonding configuration through XPS and FTIR spectroscopy, for optimizing deposition condition, to minimize impurity content, as well as, to obtain desired B/C ratio in the films. Surface morphology of the deposited films was investigated using Field Emission Scanning Electron Microscope (FESEM). Film thickness was measured by 3D optical profilometry. Neutron transmission measurements of the deposited films were performed in an experimental nuclear reactor. The characterization results were utilized to correlate the change in chemical composition, stoichiometry, and total macroscopic cross section (Σ_t) with deposition conditions.

3.2 Experimental:

Schematic of the experimental set up used for deposition of ^{nat}boron carbide thin films via RF-PECVD is shown in Figure 2.1 (chapter 2). Detailed description of the experimental setup is given in section 2.1.1 of chapter 2. Briefly, a 13.56 MHz RF power supply along with automated impedance matching network was used to generate plasma. Argon plasma was used for sputter cleaning of the substrate surfaces and actual depositions were carried out in Helium plasma. For deposition of thin films, p-type Silicon (100) (99.999% purity) and aluminium (99.99% purity) substrates were used. Respective substrate cleaning procedures are discussed in details in section 2.3 of chapter 2. Compositional, structural, and other physical characterization was performed on ^{nat}boron carbide films deposited on silicon substrates. Neutron transmission measurement was performed on the films deposited on $25mm^2$ square plates of Aluminium having 0.9 mm thickness, such substrates were chosen owing to their low thermal neutron absorption (0.03% of total neutron flux). A set of five ^{nat}boron carbide thin films were deposited using substrate self-bias as variable. Development of DC self-bias is a characteristic feature of the capacitively coupled RF plasma system. It is a negative potential that develops between plasma and powered electrode (which is also the substrate holder in our case) and originates mainly due to the difference in mobility of electrons and ions (as discussed in section 1.4.2.4). This DC self-bias essentially biases the substrates to a negative potential and can be controlled by changing the power coupled to plasma. This negative self-bias plays a pivotal role in etching and deposition of thin films via PECVD. It attracts ions from plasma towards substrate surface. Energetic ion bombardment on the surface of growing film affects surface adatom mobility, in turn affecting the composition and structure of thin films. In our study, the set of five boron carbide thin films were prepared by keeping substrate self-bias values were set at -75 V, -100 V, -125 V, -150 V, and -175 V during deposition. These five deposited boron carbide thin film samples will be referred to as -75 V, -100V, -125 V, -150 V, and -175 V films throughout this chapter.

3.3 Results:

3.3.1 Film thickness measurement:

Figure 3.1 shows 3D optical profilometry measurement results of deposited ^{nat}boron carbide thin films. Although deposition time was kept constant for all the samples, film thicknesses varied in the thickness range $4.08\,\mu m - 4.9\,\mu m$ due to change in deposition rate. Variation in deposition rate with self-bias is demonstrated in Figure 3.2. Deposition rate was found to decrease almost linearly with increase in magnitude of substrate self-bias. This was an important observation suggesting that the decrease in deposition rate at higher substrate self-bias was probably due to the re-sputtering effect [85].

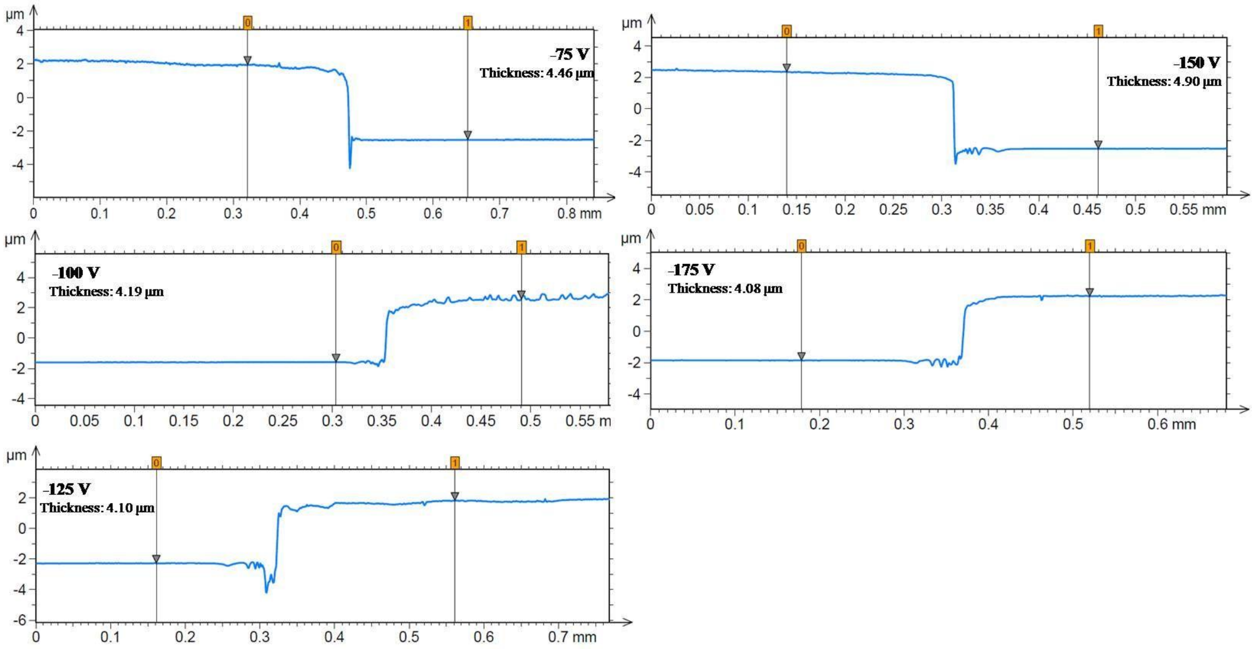

Figure 3.1: 2D step profile of the films measured in 3D optical profilometer and associated film thicknesses.

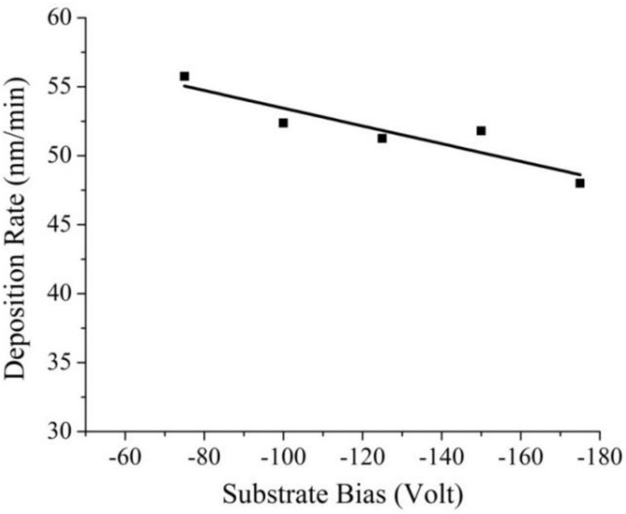

Figure 3.2: Change in deposition rate with self-bias.

3.3.2 Assessment of surface and bulk chemical environment:

Surface chemical environment of constituent elements in the deposited films were investigated using ex-situ XPS technique. XPS results also shed light on the surface chemical stability of the films, and their response to ambient conditions. Analysis of the electron spectra were performed using XPS peak fit 4.1 software. Deconvoluted XPS spectra corresponding to B 1*s*, C 1*s*, and O 1*s* peaks for deposited films are shown in Figures 3.3 (a), (b), and (c), respectively. In B 1*s* spectrum (Figure 3.3 (a)), the most dominant peak is located at 189.5 eV corresponding to $BC_{3.4}$ phase [86]. Oxides appear beyond 190.0 eV in the spectrum. Chemical environment for boron atoms, corresponding to oxides are namely B_2O_3 and BCO_2 having binding energies 193.2 eV and 192.0 eV, respectively [87]. Oxy-boron carbide species appear at 190.9 eV [88]. The peak present around 188.5 eV represents stoichiometric B_4C phase [89]. 187.9 eV peak corresponds to B-B bonding in boron cluster [90]. Usually, B 1*s* binding energy decreases with increasing boron content in the composition [57].

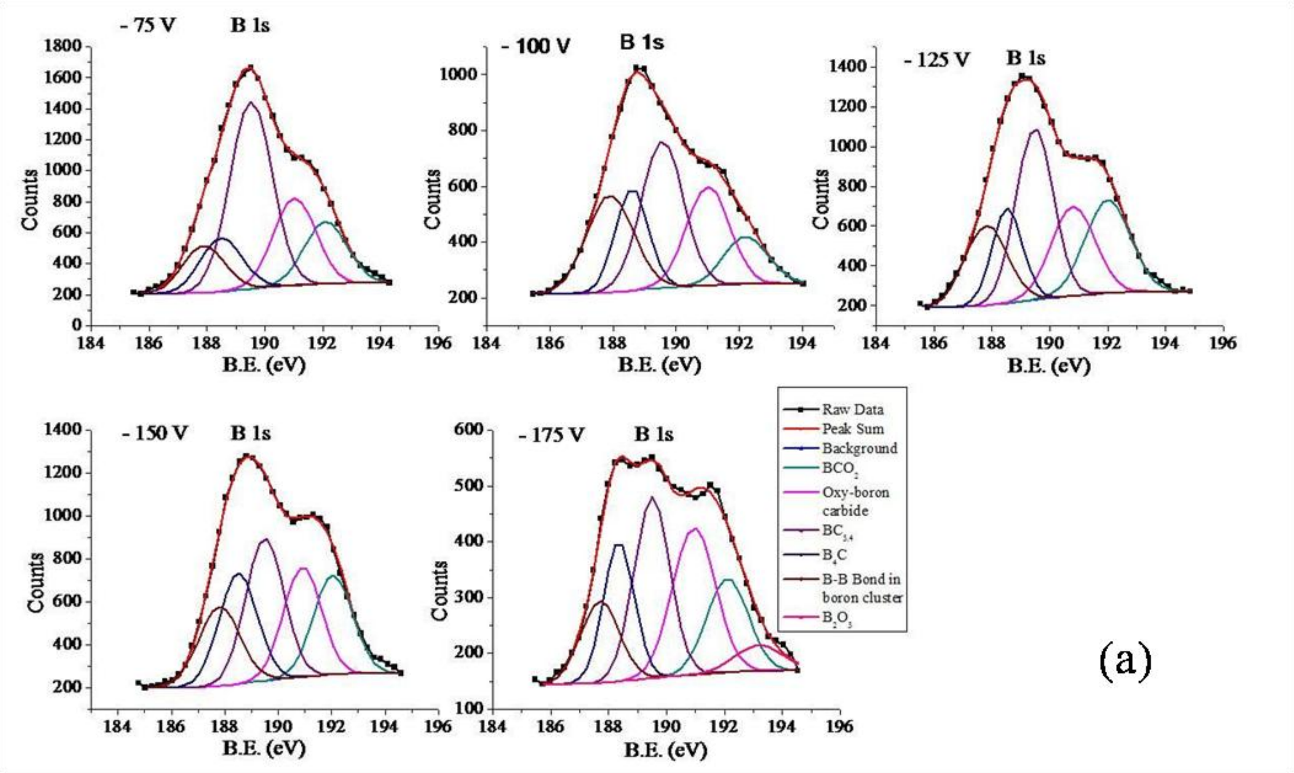

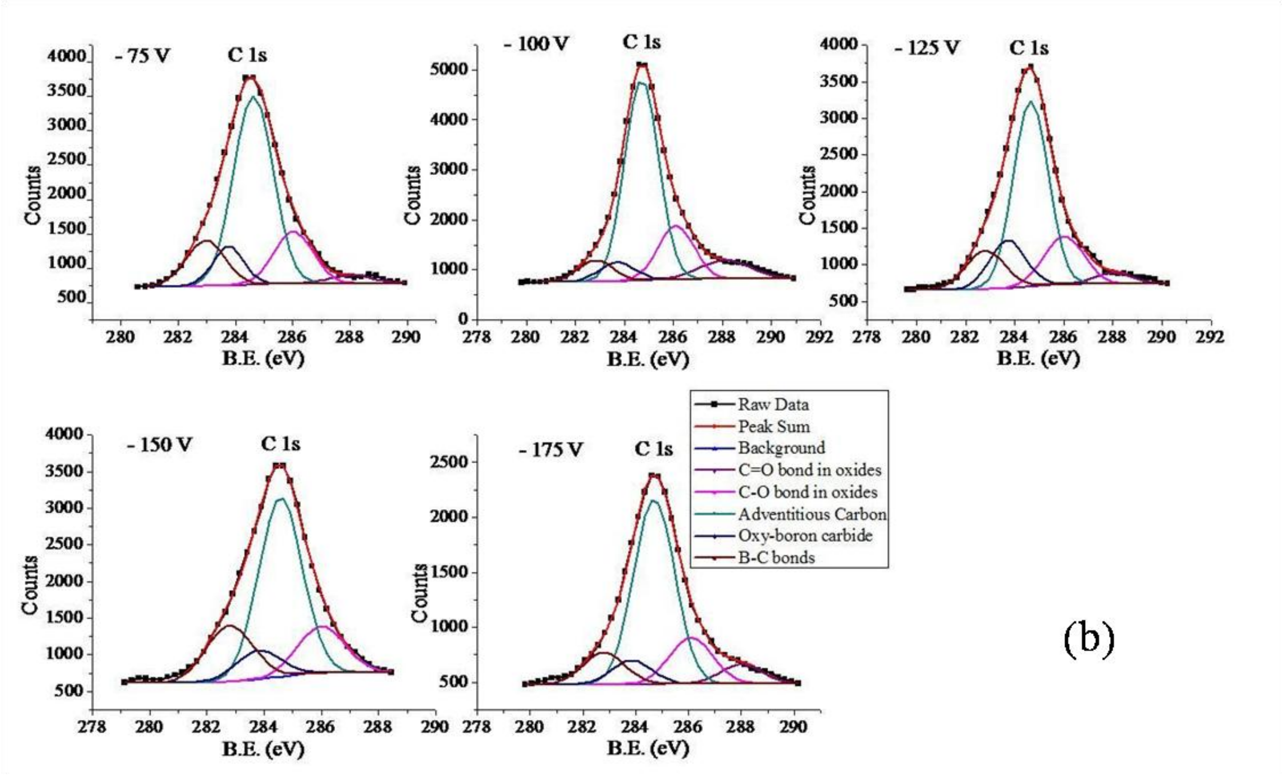

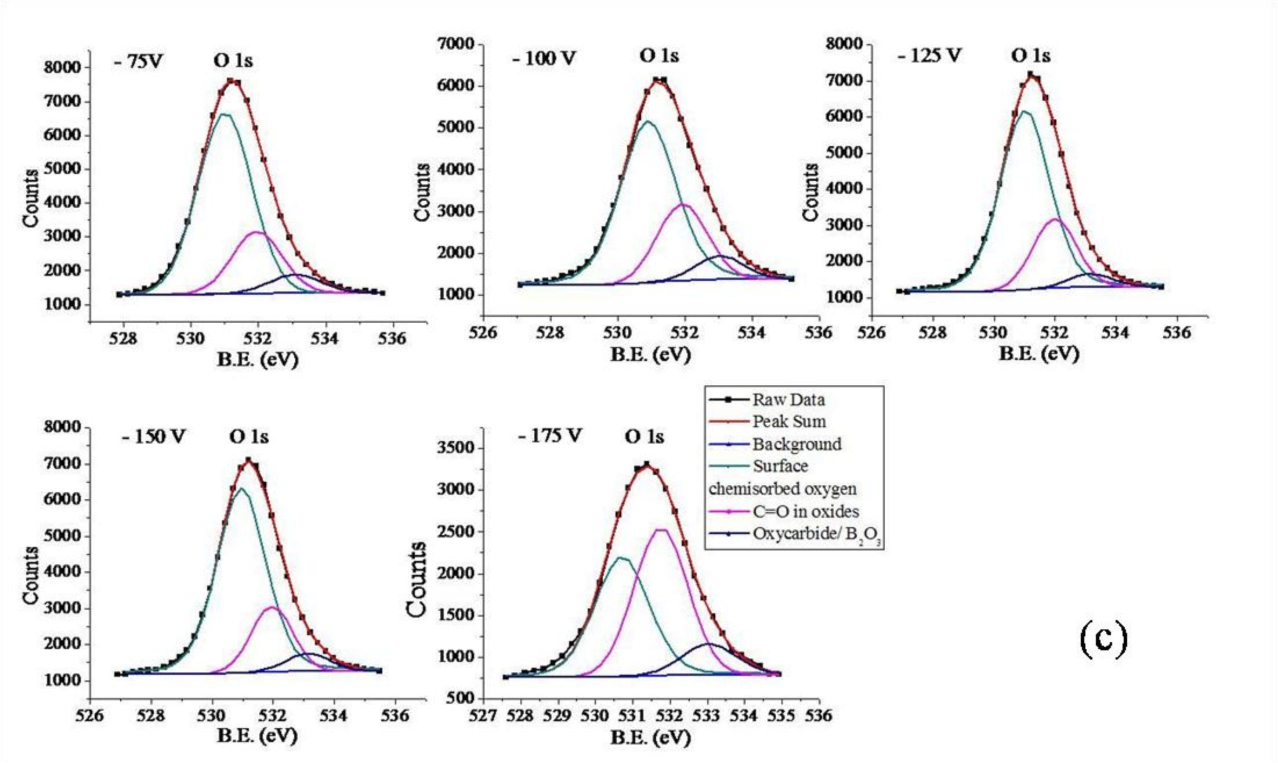

Figure 3.3: Core level XPS spectra of (a) B 1*s* (b) C 1*s* and (c) O 1*s* lines of deposited ^{nat}boron carbide films.

Again, lower binding energy peak indicates a chemical environment for boron atoms with more electropositive neighbouring atoms [91]. Therefore the peak at 187.9 eV corresponds to B-B bond in B_xC structure where $x > 4$. Existence of stable boron carbide phases in the concentration range from B_4C to $B_{10.4}C$ [21] support our finding of high boron containing carbide compound by RF-PECVD. In Figure 3.3 (a) it is also observed that shape of the B 1*s* spectral envelope changes significantly as self-bias increases. With increasing magnitude of self-bias, intensity of oxide peak BCO_2, and oxy-boron carbide peak increases considerably, resulting in peaking of B 1*s* envelope towards the higher binding energy side. Also for -175 V film, appearance of significant B_2O_3 oxide peak was observed.

Core level C 1*s* spectra (Figure 3.3 (b)) has dominant adventitious carbon peaks at 284.6 eV [92] which is incorporated in the films as a result of ambient exposure. Peaks appearing around 288.0 eV, and 286.0 eV correspond to C=O and C-O bonds in oxide environments, respectively [87, 92]. Peaks appearing around 283.8 eV, and 282.9 eV represent carbon atom in oxy-boron carbide, and B-C bonds [92]. From deconvoluted C 1*s* spectra, no particular trend was observed with change of self-bias.

O 1*s* spectra (Figure 3.3 (c)) was deconvoluted into three peaks centered near 531 eV, 532 eV, and 533.1 eV [92, 93] referring to surface chemisorbed oxygen [94] , C=O in oxides and oxy-boron carbide/ B_2O_3 phases [92], respectively. Oxygen can appear in the films for two reasons: as surface contamination due to exposure to ambient condition, and due to presence of residual oxygen inside the reactor during deposition (though precautions were taken to minimize the residual gases by evacuating the chamber to 5×10^{-5} mbar before each deposition run).

Asymmetric nature of peaks shown in Figure(s) 3.3 (a), (b), & (c), made it evident that multiple chemical environments for boron, carbon, and oxygen were present in all the films. Though B 1*s* spectra in Figure 3.3 (a) showed a trend that, with increasing bias, more amount of boron starts getting combined with oxygen. C 1*s* (Figure 3.3 (b)) and O 1*s* (Figure 3.3 (c)) did not show any such trend with self-bias. This happened due to the fact that carbon and oxygen from ambience contaminate the surface of the films apart from being present during deposition, while source of boron was solely the precursor.

XPS is an excellent technique for surface analysis, but fails to provide exact information about bulk elemental composition of the samples. However, for thicker films having thickness typically in the micrometer range, knowing the bulk elemental composition becomes necessary to assess their composition and associated properties. Proton elastic backscattering measurement (p-EBS) technique is useful for probing bulk elemental composition of such films. This technique has comparatively greater probing depth (typically 2- 10 μm) than XPS (up to 10 nm). p-EBS measurement results for our samples are presented

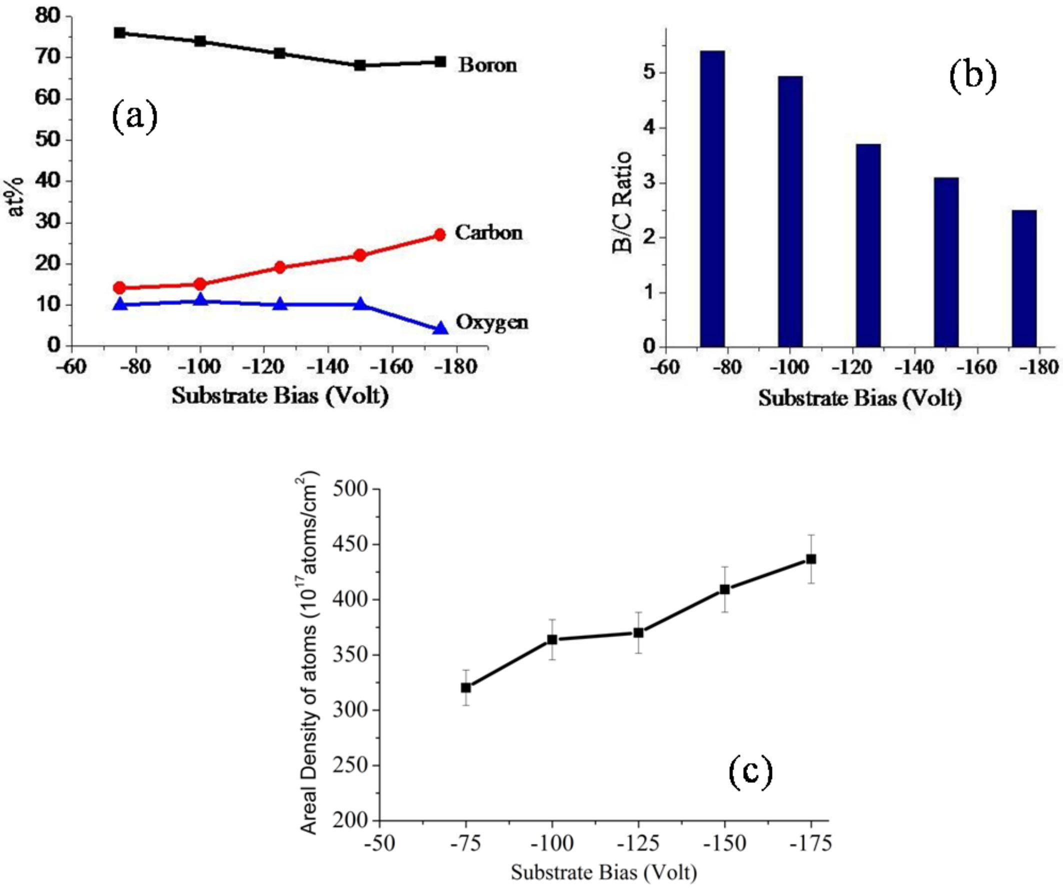

Figure 3.4: Variation of (a) elemental atomic percentages, (b) B/C ratio and (c) areal density of atoms in the deposited films as obtained from p-EBS results.

in Figures 3.4 (a), (b), and (c). Figure 3.4 (a) shows atomic percentage variation of boron, carbon, and oxygen in the bulk of the films, Figure 3.4 (b) shows variation of B/C ratio, and Figure 3.4 (c) exhibits variation of areal density of atoms with substrate self-bias. From the figures it is evident that stoichiometric B/C ratio decreases gradually with increasing self-bias. Dependence of stoichiometry and areal density of atoms of $^{nat}B_xC$ films with self-bias is presented in Table 3.1. Table 3.1 shows that B/C ratio can be as high as 5.28 for -75 V film and it decreases gradually to 2.56 for -175 V film. On the other hand, areal density of atoms is found to increase from -75 V film to -175 V on account of increasing impinging ion energy (Figure 3.4 (c)).

Table 3.1: Variation of stoichiometry and areal density of atoms in ^{nat}boron carbide films with self-bias obtained from p-EBS measurement.

RF Self-bias on the substrate	**Stoichiometric ratio of B and C**	**Areal Density of atoms (10^{15} at./cm^2)**
-75 V	$B_{5.28}C$	32031
-100 V	$B_{4.94}C$	36380
-125 V	$B_{3.74}C$	37005
-150 V	$B_{3.1}C$	40925
-175 V	$B_{2.56}C$	43670

3.3.3 FTIR Spectroscopy:

FTIR spectra of the deposited films in the spectral range 400 cm^{-1} to 3500 cm^{-1} are shown in Figure 3.5. The prominent peaks in FTIR spectra are close to ~ 800 cm^{-1}, 1100 cm^{-1}, 1450 cm^{-1}, 1600 cm^{-1} and 2600 cm^{-1}. Peaks around ~ 800 cm^{-1}correspond to intra-icosahedral B-B vibrations of the compositions $B_{4.3}C$, $B_{6.3}C$ and $B_{10.37}C$ [68] and those close to 1100 cm^{-1}correspond to B-C band. Three other major peaks close to ~ 1450 cm^{-1}, ~ 1600 cm^{-1} and 2600 cm^{-1} represent stretching mode vibrations of different bonds. While the first one comes from B-O bonds in the films [25], the second one originates from the vibrations of CBC chains in the boron carbide structure [70] and the third one represent vibration of B-H bonds [95]. FTIR measurement results presented in Figure 3.5 reveal that, intensity of the peak corresponding to intra-icosahedral B-B vibrations (near 800 cm^{-1}) for film deposited at -75 V appears to be stronger than the other peaks. For film deposited at -100 V, intensity of the peak representing CBC chain vibrations at ~ 1600 cm^{-1} also increases and almost becomes comparable to the intensity of the peak at ~ 800 cm^{-1}. This indicates increase in the number of CBC chains in the bulk for this film. It is also observed that, as substrate bias increases from -75 V to higher values, the intensity of the peak corresponding

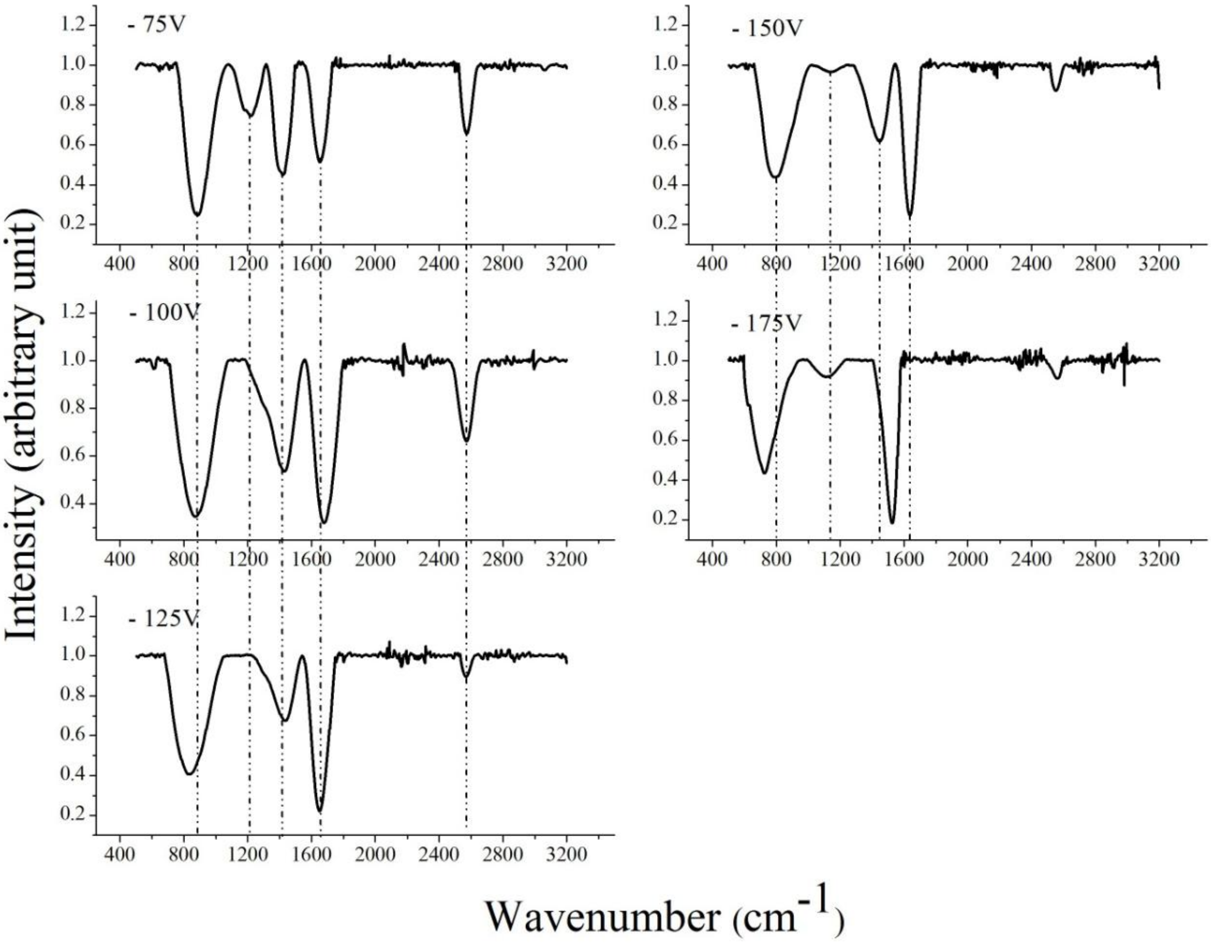

Figure 3.5: FTIR absorption spectra of ^{nat}boron carbide films deposited by varying self-bias.

to the vibrations of CBC chains (close to 1600 cm^{-1}) increases gradually (Films deposited at -100 V up to -175 V), indicating increase in carbon content in the bulk for these films.

3.3.4 Surface morphology:

Self-bias on the substrate during deposition was found to have a significant influence on surface morphology of the films as revealed by FESEM micrographs, shown in Figure 3.6.

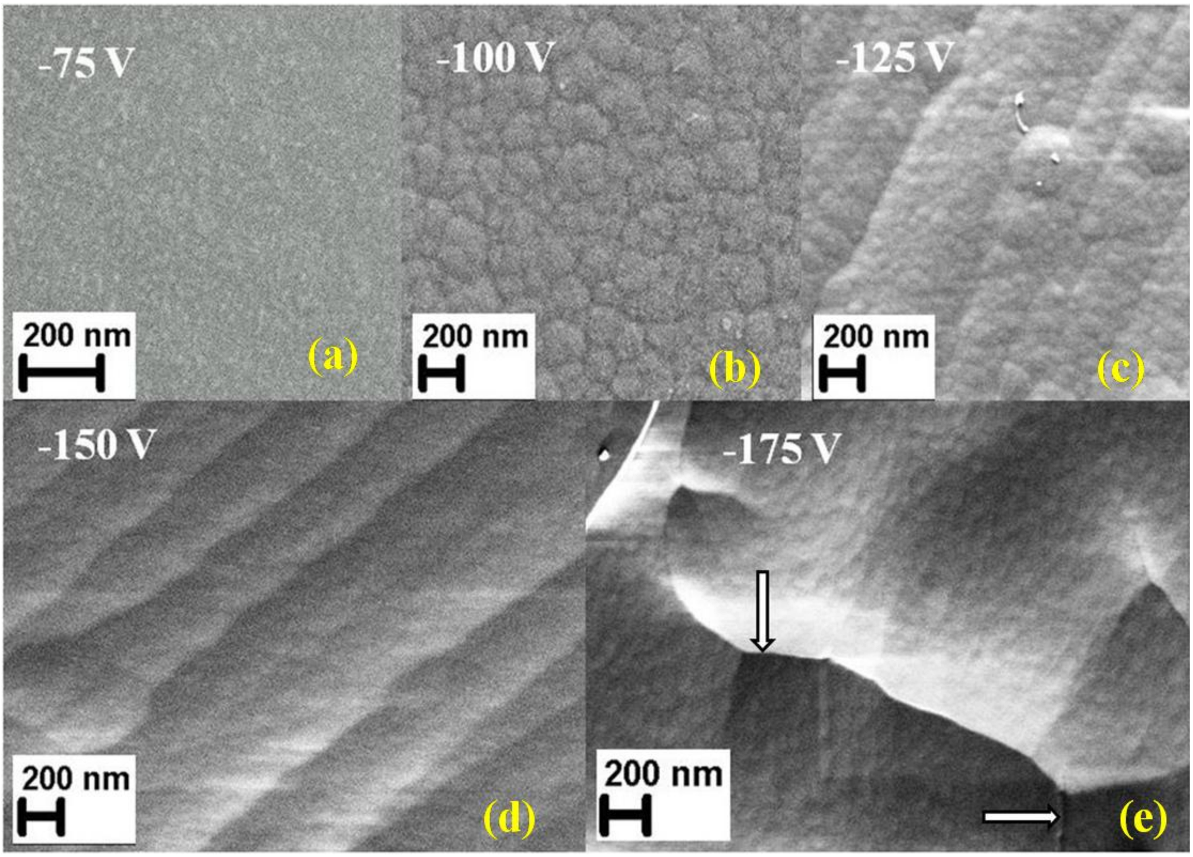

Figure 3.6: FESEM micrographs of ^{nat}boron carbide films deposited at (a) -75 V, (b) -100 V, (c) -125 V, (d) -150 V, and (e) -175 V self-bias values.

FESEM micrographs for films deposited at -75 V and -100 V self-bias values show granular structures on the surface. Columnar undulations are seen on the surface of -125 V and -150 V films, with the latter showing slightly larger amplitude. Film deposited at -175 V bias does not show any such undulation, instead exhibits micro-cracks (marked by arrows in Figure 3.6) on the surface which eventually could lead to film degradation.

3.3.5 Measurement of neutron transmission:

Total macroscopic cross section (Σ_t in cm^{-1}) of the ^{nat}boron carbide thin films was calculated from neutron transmission measurement results. Variation of Σ_t with substrate self-bias is given in Figure 3.7. Σ_t is the sum of macroscopic cross sections of all the nuclides present in the film considering neutron absorption and scattering. It was calculated from the simple formula:

$I(x) = I_0 e^{-\Sigma_t x}$……………………………………(3.3)

$\Sigma_t = \frac{[\ln(I_0/I(x))]}{x}$………………………………….. (3.4)

Where I_0 = Intensity of the neutron beam incident on the sample,

$I(x)$ = Intensity of the neutron beam after passing through the sample, and

x = Thickness of the films

$I(x)$ was corrected for background and absorption in bare aluminium substrate. Neutron transmission data was averaged over various positions on each film. This method gives a direct measurement of total macroscopic cross section, Σ_t. Error in neutron transmission measurement was nearly ~1%. As per the measurements, film deposited at lowest self-bias i.e. -75 V show least value of Σ_t (170.47 cm^{-1}) and the one deposited at -175 V exhibits the highest Σ_t (273.38 cm^{-1}) owing to structural densification, resulting in increased areal density of atoms with increase in self-bias (Figure 3.4 (c), Figure 3.7, and Table 3.1, and 3.2).

Table 3.2: Variation of $\Sigma_t$with substrate self-bias.

Substrate Self-bias (in Volt)	**Thickness (in µm)**	**% Neutron absorption**	**Total Macroscopic cross section Σ_t (cm^{-1})**
-75	4.46	7.32	170.47
-100	4.19	10.06	253.36
-125	4.10	10.4	267.68
-150	4.90	11.55	249.41
-175	4.08	10.6	273.38

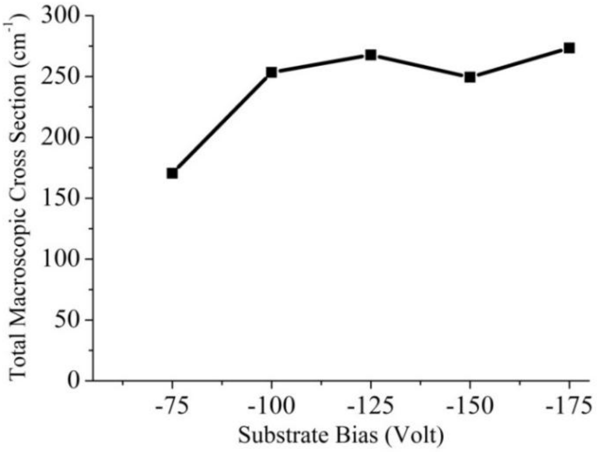

Figure 3.7: Variation of Total Macroscopic Cross Section for neutrons (Σ_t) with self-bias.

3.4 Discussion:

Characterization results revealed that, deposition rate was highest at -75 V and lowest at -175 V self-bias (Figure 3.2), linearly decreasing with increasing magnitude of self-bias. Normally, increase in self-bias requires increase in RF power fed to the plasma, which helps in further fragmentation of vapor phase precursor resulting in high deposition rate. On the other hand, highly energetic ions (predominantly He) impinging on the growing film surface causes re-sputtering of the deposited material. Re-sputtering threshold energy of boron carbide (B_4C) is about 70 eV for He [96, 97]. In addition to the self-bias, plasma potential also accelerates ions towards the substrate. Typically for such high frequency of operation (13.56 MHz), plasma potential reaches a value of few hundred volts [42]. Therefore, with increasing self-bias, impinging ion energy on the growing film also increase which subsequently leads to higher re-sputtering rate. Therefore, in this study, deposition rate was found to decrease on account of two competing effects: increase in deposition rate due to increased precursor fragmentation at higher self-bias, and at the same time enhanced rate of re-sputtering of deposited material.

If RF power coupled to the plasma is changed, it normally changes the plasma chemistry during deposition. It was observed from our XPS analysis that the content of oxides and oxy-boron carbides in the films increases with increasing self-bias. Since the precursor feed rate, and He and Ar gas flow rates were kept fixed for all the experiments, increasing RF power results in increased dissociation of residual gases present in the chamber. Evidently, with increase in self-bias, residual oxygen in the chamber dissociate to a greater extent, and being more electronegative, easily bonds with boron atoms. As a result, the appearance of B_2O_3 peak in XPS spectra for -175 V film was observed.

It has been reported earlier that defect content in the films increases with increasing ion bombardment energy [92] and impurities from the plasma can be introduced in the films during energetic ion bombardment [98]. Bombardment by highly energetic ions also cause strain in the films. This may be the reason for films deposited at highest self-bias value (-175 V) peeling off after few months, while the other films deposited at lower bias values show comparatively higher longevity.

With increasing substrate self-bias, the number of CBC chains increases considerably in the deposited films, indicating formation of boron carbide in carbon rich end as seen in FTIR spectra. This result is in agreement with p-EBS measurement results which indicates decreasing B/C ratio with increasing self-bias. Results from p-EBS analysis show that it is possible to achieve B/C ratio ~ 5.5 in bulk ^{nat}boron carbide films by RF-PECVD (Figure 3.4 (b)). Though XPS and FTIR results indicated deposition of boron rich stoichiometric phases at higher self-bias, overall B/C ratio was found to decrease as seen in p-EBS results. XPS results also indicate an increase in boron oxides and oxy-boron carbides at higher bias values.

p-EBS measurement data indicates that films deposited at highest self-bias (-175 V) have the highest areal density of atoms (Table 3.1 and Figure 3.4 (c)), hence maximum structural densification [99]. This structural densification at higher impinging ion energy could explain the maximum value of Σ_t as exhibited by -175 V film in neutron transmission measurements, in spite of having the lowest stoichiometric B/C ratio.

From FESEM micrographs presented in Figure 3.6, it was observed that with increase in self-bias, columnar surface undulations appeared in the films. These micrographs also suggested that continuous increase in the self-bias might be detrimental for the film stability. At higher self-bias (-175 V), appearance of micro-cracks can be noticed, which affect the adhesion of the film with the substrate, resulting in poor ambient stability of such films. Typically, for high substrate self-bias, surface ion bombardment also degrade the quality of the deposited films. There exists a minimum bombardment energy for creating atomic displacement defects [100] which depend on the incident charge species. The atomic threshold displacement energies of boron and carbon atoms in boron carbide typically lie in the range of 20 eV [101]. Since the impinging ion energy in our study fairly exceeds the minimum bombardment energy, defect formation can also take place in the boron carbide structure via this mechanism.

3.5 Summary:

Detailed XPS, p-EBS, and FTIR spectroscopy investigation, 3D optical profilometry measurements, FESEM imaging, and neutron transmission measurements were performed on RF-PECVD deposited ^{nat}boron carbide thin films. Characterization results led us to a conclusion that, it is advisable to use low self-bias to obtain stable films with high B/C ratio, having desired film thickness. However, higher self-bias was found to be suitable for deposition of ^{nat}boron carbide films with higher value of total macroscopic cross section (Σ_t). Film thickness can be optimized for neutron detection considering the range of Li^7 and He^4 produced in neutron capture reaction in the films. It is also evident from FESEM micrographs that surface morphology of the films changes as a result of energetic ion bombardment at higher self-bias. Further increase in self-bias eventually leads to film degradation over time.

Systematic variation of B/C ratio with self-bias demonstrated that, it is possible to deposit a ^{nat}boron carbide film with preferred elemental composition, choosing appropriate deposition conditions. Hence, ^{nat}Boron carbide thin films deposited using RF-PECVD exhibited promising features for their application in neutron detection.

Chapter 4 : Evaluation of composition dependent microstructure, and optical properties of ^{nat}boron carbide ($^{nat}B_xC$) thin films

4.1 Introduction:

In addition to a wide range of application starting from tribology to military, space, micro-electronics, and nuclear technology [2], boron carbide has also attracted attention of researchers' worldwide as optical material in single and multilayer optics for application in extreme ultraviolet (EUV)/ X-ray region. At present, various materials are being investigated for fabrication of optical devices in the aforementioned region of electromagnetic spectrum, among them CVD deposited silicon carbide (SiC) is widely used, offering highest normal reflectance (40% till 60 nm) in EUV region [102]. Development of newer material for EUV/ X-ray optics, exhibiting better performance, and higher shelf-life under harsh experimental conditions still remains a necessity. Some materials like boron carbide and Iridium with comparatively lower reflectance are advantageous for the said application as they offer reasonably higher environmental stability, and comparatively better cost effectiveness. Boron carbide is also finds application in solar spectroscopic studies, synchrotron radiation beam lines, plasma diagnostics, lithography, and X-ray astronomy [103, 104].

We have chosen Plasma Enhanced Chemical Vapor Deposition (PECVD) technique over other available PVD and CVD methods [2, 59, 105] for deposition of ^{nat}boron carbide thin films as it requires lower process temperature, allows uniform deposition over substrates of different geometry, and leads to films having superior surface quality, and adhesion. In PECVD, film growth mechanism is rather complex and strongly dependent on deposition parameters. A systematic control of deposition parameters enables control on the film stoichiometry and hence film properties which has been observed in our previous study [78].

In this work, we have investigated influence of film stoichiometry on the optical properties of RF-PECVD deposited ^{nat}boron carbide ($^{nat}B_xC$) thin films. Films were deposited on silicon (100) and sodalime glass substrates at different substrate self-bias varying from -100V to -250V. Optical property, structure, and stoichiometry of the films were determined by spectrophotometry, X-ray diffraction, and proton elastic backscattering spectrometric measurements, respectively. Soft X-ray reflectivity in the wavelength range of 40 Å -360 Å has been measured to explore potential of these films for application as optical material in this region of electromagnetic spectrum. Our experimental investigations were aimed at determining optimum deposition condition of ^{nat}boron carbide thin films by RF-PECVD for their application as optical material.

4.2 Experimental:

4.2.1 Deposition of $^{nat}B_xC$ thin films:

Schematic of the experimental set up used for deposition of ^{nat}boron carbide thin films is shown in Figure 2.1. Detailed description of the experimental setup is given in section 2.1.1 of chapter 2. For deposition of thin films, p-type Silicon (100) (99.999% purity), and sodalime glass (99.99% purity) substrates were used. The substrate cleaning procedures are discussed in details in section 2.3 of chapter 2. Before starting the deposition experiments, reactor base pressure was brought down to 2×10^{-5} mbar to minimize effects of moisture and residual atmospheric gases. Depositions were carried out at a pressure of ~ 10^{-3} mbar. Substrates were first sputter-cleaned by Argon plasma (8 sccm flow at -200 V self-bias) for 20 minutes before deposition. Helium gas was then introduced into the plasma reactor at a pressure of 0.180 mbar for 10 minutes during which heated precursor vapor was allowed to enter the deposition chamber. Four ^{nat}boron carbide thin films of different chemical compositions were prepared by varying DC substrate self-bias from -100 V to -250 V, in steps of -50 V for the deposition runs. Hereafter, each sample will be identified by their corresponding substrate self-bias values.

4.2.2 Characterization:

The optical transmission spectra of the films were recorded using a UV-VIS-NIR spectrophotometer (UV-3101PC, SHIMADZU) in the range 200 nm -1200 nm to determine refractive index (n), extinction co-efficient (k), absorption co-efficient (α), optical band gap (E_g) and film thickness (t). ^{nat}Boron carbide ($^{nat}B_xC$) thin films deposited on sodalime glass substrates were used for optical characterization since the spectrophotometric measurements were taken in transmission mode. Bulk elemental composition of the films was investigated by p-EBS technique. The measurements have been performed using 2.0 – 3.0 MeV proton beam obtained from a 3 MV Tandetron. Film structures were determined by XRD in Bragg-Brentano geometry with 2θ angle in the range of 20˚-30˚ using Cu-K$_\alpha$ (λ =1.5406 Å) radiation in angular steps of 0.02˚. Grain size was also calculated from XRD peaks using Scherrer's equation (equation 4.1). Soft X-ray reflectivity of the films was measured at the soft X-ray reflectivity beamline in INDUS 1 at Raja Ramanna Centre for Advanced Technology (RRCAT), Indore. Reflectivity of the samples was determined in the wavelength range 40 Å - 360 Å at a fixed grazing angle 5˚. Surface microstructure of the deposited films was investigated using a field emission scanning electron microscope (FESEM).

4.3 Results:

4.3.1 Film stoichiometry:

Atomic percentages of boron, carbon, and oxygen in the films as measured by p-EBS technique are shown in Figure 4.1. The boron to carbon(B/C) ratio of the films was found to be in the range 3.93 to 5.02 (Table 4.1). Figure 4.1 shows that a significant amount of oxygen impurity is incorporated in the films during deposition. B/C ratio was found to be higher, 4.93 and 5.02 for the films deposited at -100 V and -150 V respectively, while it decreases for the films deposited at comparatively higher substrate self-bias assuming values 3.93 and 4.16 for -200 V and -250 V films respectively. The variation of B/C ratio with substrate self-bias is consistent with our previous findings [78]. The overall uncertainty in the p-EBS measurement is taken as ~ ± 5% [106].

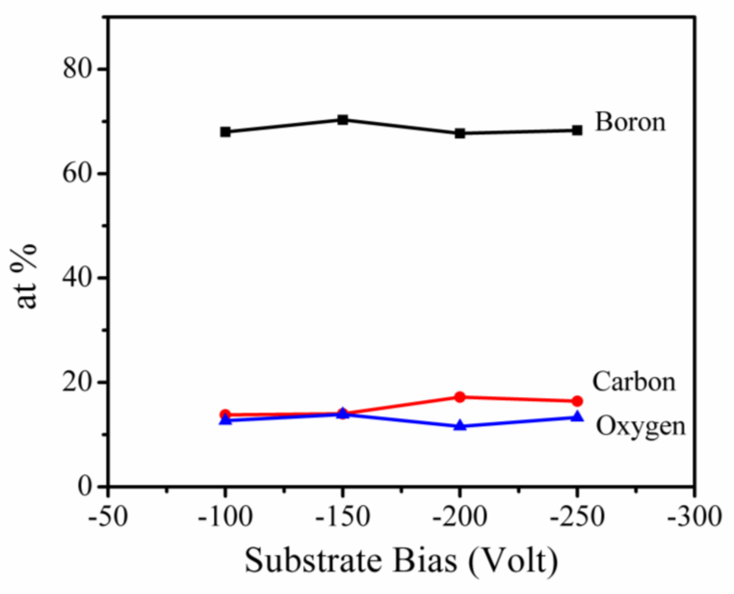

Figure 4.1: Variation of elemental atomic percentage with substrate bias in $^{nat}B_xC$ thin films.

Table 4.1: Comparison of composition, microstructure, and optical properties of $^{nat}B_xC$ thin films.

Substrate self-bias (Volt)	**B/C ratio**	**Grain Size (nm)**	**Thickness (t) (μm)**	**Refractive index (n) @ 400 nm**	**Extinction Co-efficient (*k*) @ 400 nm**	**Direct Band gap (eV)**	**Indirect Band gap (eV)**
-100	4.93	130	1.87	1.87	0.0226	3.87	2.74
-150	5.02	105	1.64	1.89	0.0391	3.83	2.55
-200	3.93	72	1.50	1.91	0.0731	3.59	2.16
-250	4.16	73	1.47	1.97	0.0990	3.48	2.02

4.3.2 Structure and grain size:

XRD scans of $^{nat}B_xC$ thin films are shown in Figure 4.2. Presence of three distinct peaks located at 22.83˚, 27.9˚ and 32.9˚ can be clearly seen in the XRD patterns. The boron carbide phases were determined by search-match comparison with standard JCPDS-ICDD data, and it has closest match with the rhombohedral boron carbide (B_4C) and orthorhombic boron oxide (B_2O_3) peaks reported in JCPDS file nos. #75-0424 and #06-0297 respectively. Peaks located at 22.83˚ and 32.9˚ corresponds to B_4C phase and the peak at 27.9˚ matches with B_2O_3 phase as seen in Figure 4.2.

Grain size for each of the films was calculated from Scherrer's equation,

$$D_p = \frac{0.94\lambda}{\beta cos\theta} \ldots\ldots\ldots\ldots\ldots\ldots\ldots\ldots\ldots (4.1)$$

Where, D_p = Average crystallite size, β = Full width half maximum (FWHM) of the most intense peak, θ = Bragg angle in radian and λ = X-ray wavelength. To calculate grain size, FWHM of 32.9˚ peak was considered as it is the most intense peak of the B_xC XRD patterns. The grain size for all films calculated from equation 4.1 is shown in Table 4.1.

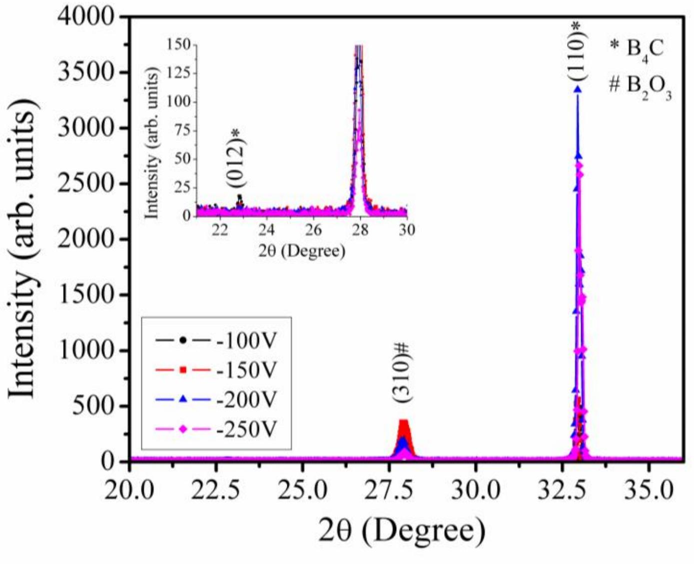

Figure 4.2: XRD patterns of $^{nat}B_xC$ thin films prepared at different substrate self-bias. Inset plot shows enlarged XRD patterns for 2θ ranging from 21-30 degree.

4.3.3 Optical properties:

Optical transmission spectra of $^{nat}B_xC$ thin films are shown in Figure 4.3. Films deposited at higher substrate self-bias exhibits lower transmission, which has been correlated mainly to variation in film stoichiometry (Figure 4.3 and Table 4.1). Optical parameters such as refractive index (n), extinction co-efficient (k), absorption co-efficient (α), and also thickness (t) of the films were derived from transmission spectra by Inverse Synthesis method [107, 108]. The experimental transmission spectra were fitted with the theoretically computed spectra to get a best match by minimizing the squared difference (χ^2). To find out the optical constants from transmission spectra, single effective oscillator model proposed by Wemple and DiDomenico was used. In this model it is assumed that the material is a congregation of individual dipole moments which are set to forced vibration upon excitation by incoming radiation. A detailed description about the inverse synthesis method and the assumptions made for the analysis is given elsewhere [109]. Assuming this single effective oscillator model, the refractive index spectrum can be described by Sellmeier relation given by:

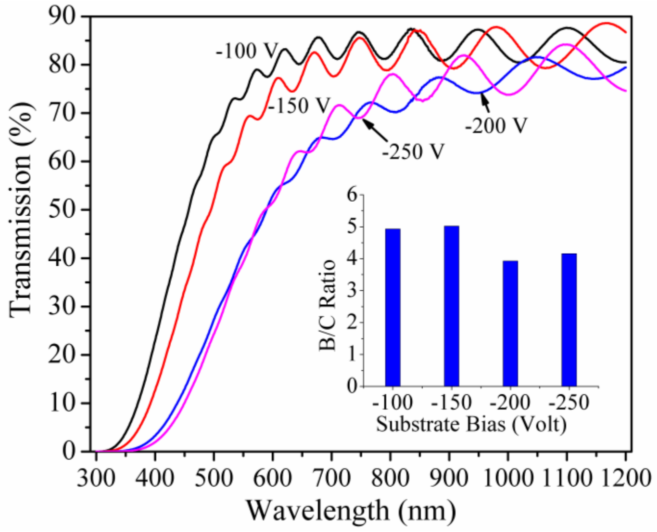

Figure 4.3: Optical transmission spectra of the $^{nat}B_xC$ thin films prepared at different substrate self-bias.

$$n(\lambda) = \sqrt{1 + \left(\frac{E_0 E_d}{E_0^2 - (1240/\lambda)^2}\right)} \text{……………………..(4.2)}$$

Where, λ is the wavelength of light, E_0 is the single oscillator energy, and E_d is the dispersion energy. The extinction co-efficient $k(\lambda)$ has been assumed to follow Urbach model [107] and expressed as,

$$k(\lambda) = \sigma exp\left(1240\beta\left(\frac{1}{\lambda} - \frac{1}{\gamma}\right)\right) \text{………………(4.3)}$$

The constants σ, β, and γ are Urbach fitting parameters. Experimental and theoretical transmission spectra were fitted using co-efficient of the dispersion model and the $^{nat}B_xC$ film thickness as fitting parameters. The value of refractive index (n), extinction co-efficient (k), and film thickness (t) were acquired from the best fit parameters of the dispersion relations. Film thicknesses obtained from the optical transmission spectra are listed in Table 4.1 while the refractive index (n) and extinction co-efficient (k) spectra of the ^{nat}boron carbide thin films deposited at different self-bias are plotted in Figure 4.4 and Figure 4.5, respectively.

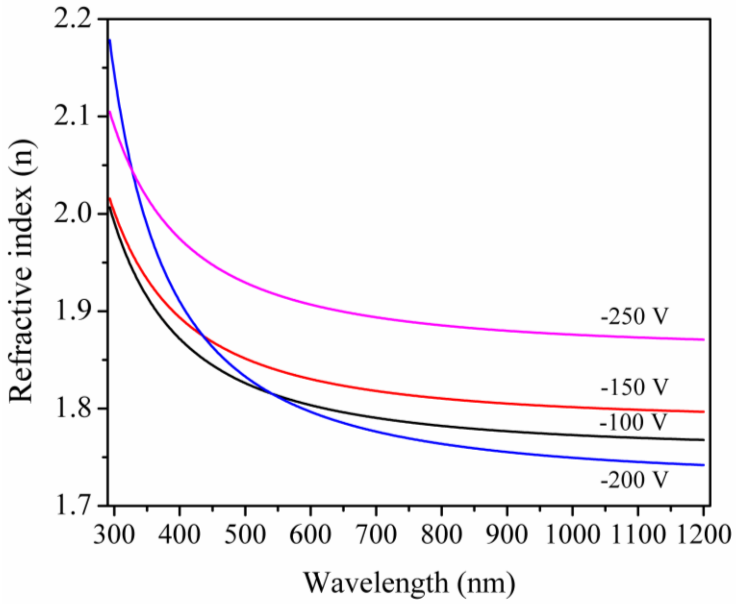

Figure 4.4: Refractive index vs. wavelength spectra of $^{nat}B_xC$ thin films.

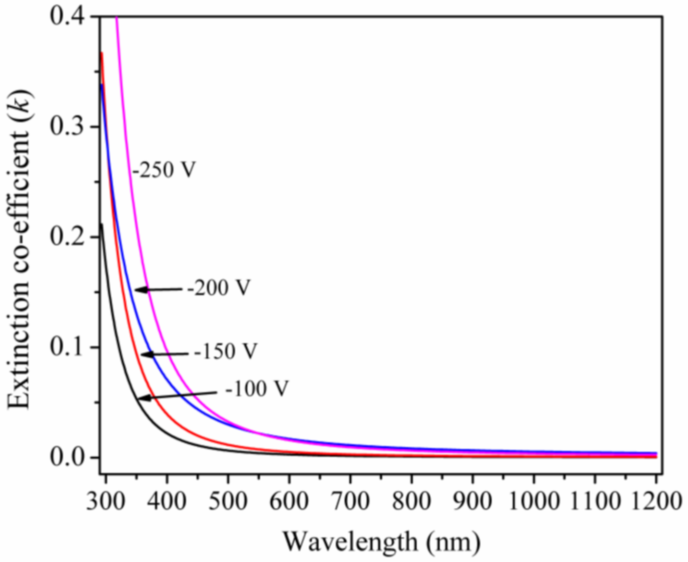

Figure 4.5: Extinction co-efficient vs wavelength spectra of $^{nat}B_xC$ thin films.

The absorption co-efficient (α) has been derived from the transmission spectra using the equation,

$$\alpha = \frac{1}{t}\ln\left(\frac{T_0}{T}\right) \ldots\ldots\ldots\ldots\ldots\ldots\ldots\ldots\ldots\ldots\ldots(4.4)$$

Where, T_0 is the transmission without sample, T is the transmission in presence of sample, and t is the sample thickness. The derived absorption spectra are shown in Figure 4.6.

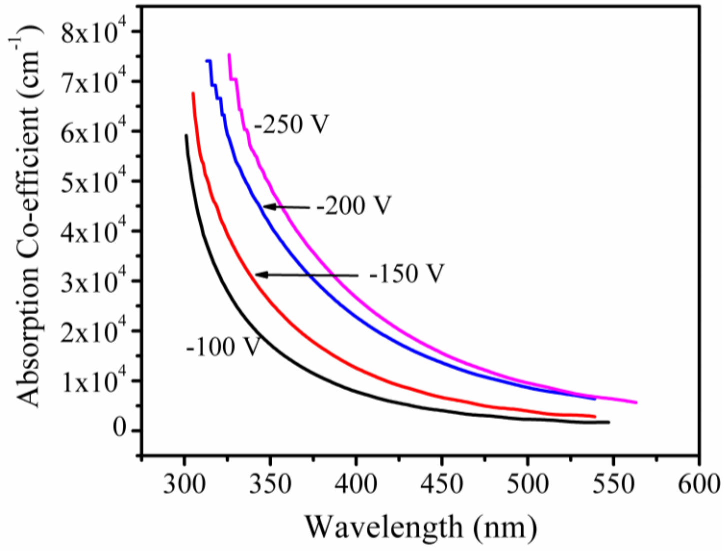

Figure 4.6: Absorption co-efficient vs. wavelength spectra of $^{nat}B_xC$ thin films.

The optical bandgap was calculated from the Tauc's relation given by:

$\alpha E = K\left(E - E_g\right)^m$ ………………………..(4.5)

Where, α is absorption co-efficient, E is the incoming photon energy, E_g corresponds to bandgap, and K is constant (Tauc parameter). Depending upon the type of transition, m takes the value *½* for allowed direct transitions or *2* for allowed indirect transitions. The Tauc plots for ${}^{nat}B_xC$ samples are given in Figure 4.7(a), and (b). Direct and indirect bandgap was calculated by extrapolating the linear portion of $(\alpha E)^2$ vs $E,$ and $(\alpha E)^{1/2}$ vs E plots, respectively. The bandgap values for different samples are listed in Table 4.1.

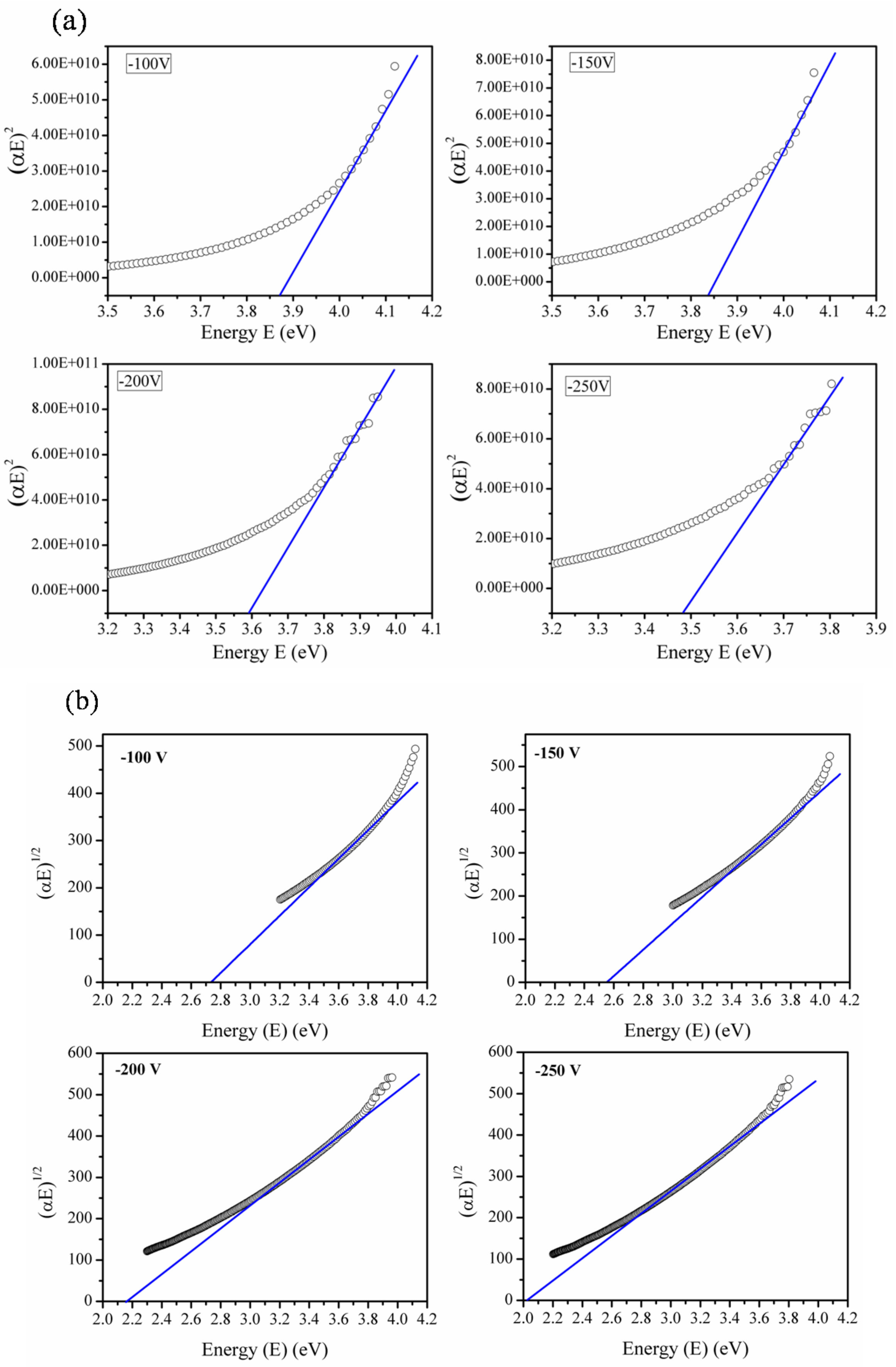

Figure 4.7: Tauc plots for (a) direct and (b) indirect bandgap estimation of $^{nat}B_xC$ films.

4.3.4 Soft X-ray reflectivity (40 Å - 360 Å) measurement:

Surface reflectivity in the X-ray region depends upon the complex refractive index of a material. The complex refractive index $(n(\lambda))$ in the X-ray region can be expressed as,

$$n(\lambda) = 1 - \delta(\lambda) - i\beta(\lambda) \ldots\ldots\ldots\ldots\ldots\ldots..(4.6)$$

Where,

$$\delta(\lambda) = \left[\frac{\rho_e r_e}{2\pi}\lambda^2\right] \ldots\ldots\ldots\ldots\ldots\ldots\ldots\ldots\ldots...(4.7)$$

and $$\beta(\lambda) = \left[\frac{\mu}{4\pi}\lambda\right] \ldots\ldots\ldots\ldots\ldots\ldots\ldots....(4.8)$$

Here, $\delta(\lambda)$ and $\beta(\lambda)$ represent the dispersion and absorption terms, λ is the wavelength of X-ray, ρ_e and r_e are density and classical electron radius, and μ is the linear absorption co-efficient of material.

Fresnel's specular reflectivity of material for an ideal surface is given by

$$R(\lambda, \theta) = \left|\frac{sin\theta - \sqrt{n(\lambda)^2 - cos^2\theta}}{sin\theta + \sqrt{n(\lambda)^2 - cos^2\theta}}\right|^2 \ldots\ldots\ldots\ldots(4.9)$$

For small incidence angles, $cos\theta = 1 - \frac{\theta^2}{2}$, $sin\,\theta = \theta$ and critical angle $(\theta_c) = \sqrt{2\delta}$

Accounting for the absorption of the X-ray beam by the material, the Fresnel reflectivity is given by,

$$R = \left|\frac{\theta - \sqrt{\theta^2 - \theta_c^2 - 2i\beta}}{\theta + \sqrt{\theta^2 - \theta_c^2 - 2i\beta}}\right|^2 \ldots\ldots\ldots\ldots\ldots\ldots\ldots(4.10)$$

This equation shows that the X-ray reflectivity decreases with increasing absorption term (β) or absorption co-efficient (μ) of material. Figure 4.8 represents grazing angle soft X-ray reflectivity spectra of the deposited $^{nat}B_xC$ samples. Results show that soft X-ray reflectivity of the samples near the K edge of boron (∼188 eV) increases till -200 V, offering a maximum reflectivity ~ 81% for -200 V sample. However for -250 V film, the reflectivity is found to be lower (~ 60%) in comparison. Above the boron K_α edge, the reflectivity can be seen to decrease for all the samples due to increased absorption.

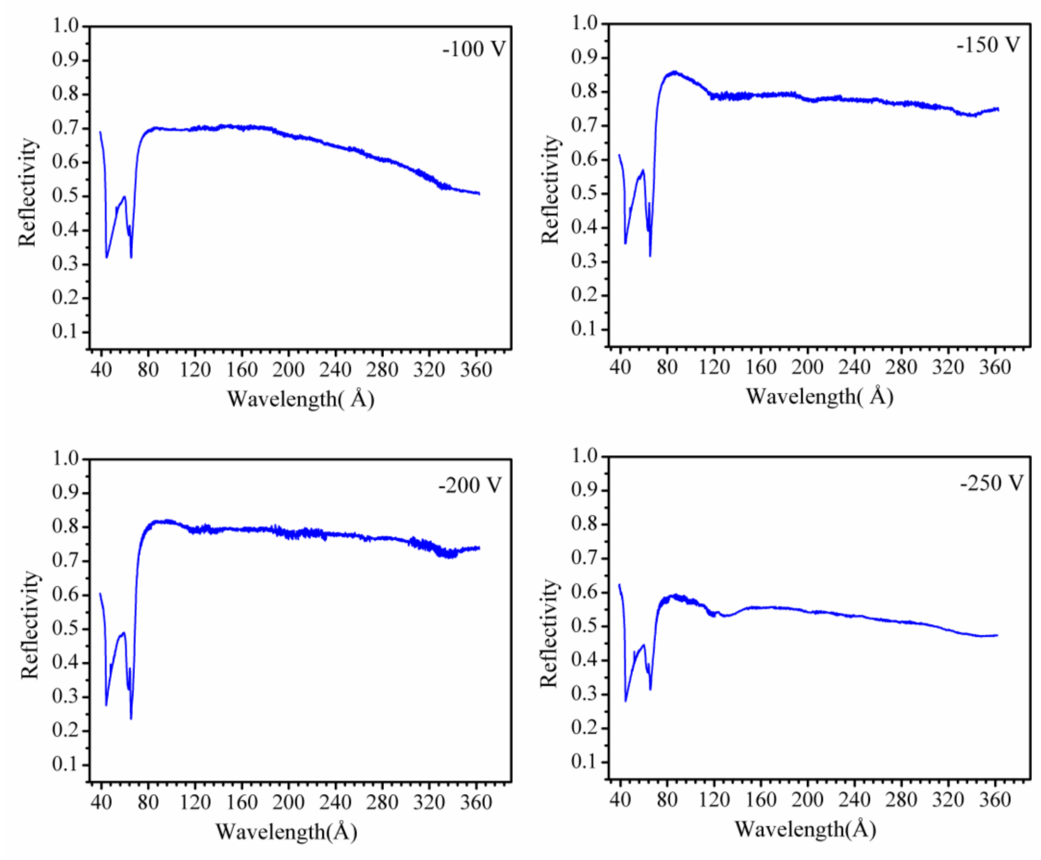

Figure 4.8: Soft X-ray reflectivity spectra of ${}^{nat}B_xC$ thin films.

4.3.5 Surface microstructure by FESEM:

Figure 4.9 represents the surface microstructure of the ${}^{nat}B_xC$ films. Though the images reveal the grainy structure of the film surfaces, the resolution is not sufficient enough to measure the grain size of individual particles. Further magnification resulted in decreased resolution causing blurring of the micrographs. For -100V film, individual grains can be noticed clearly. For other films deposited at higher self-bias, identification of individual grains becomes difficult.

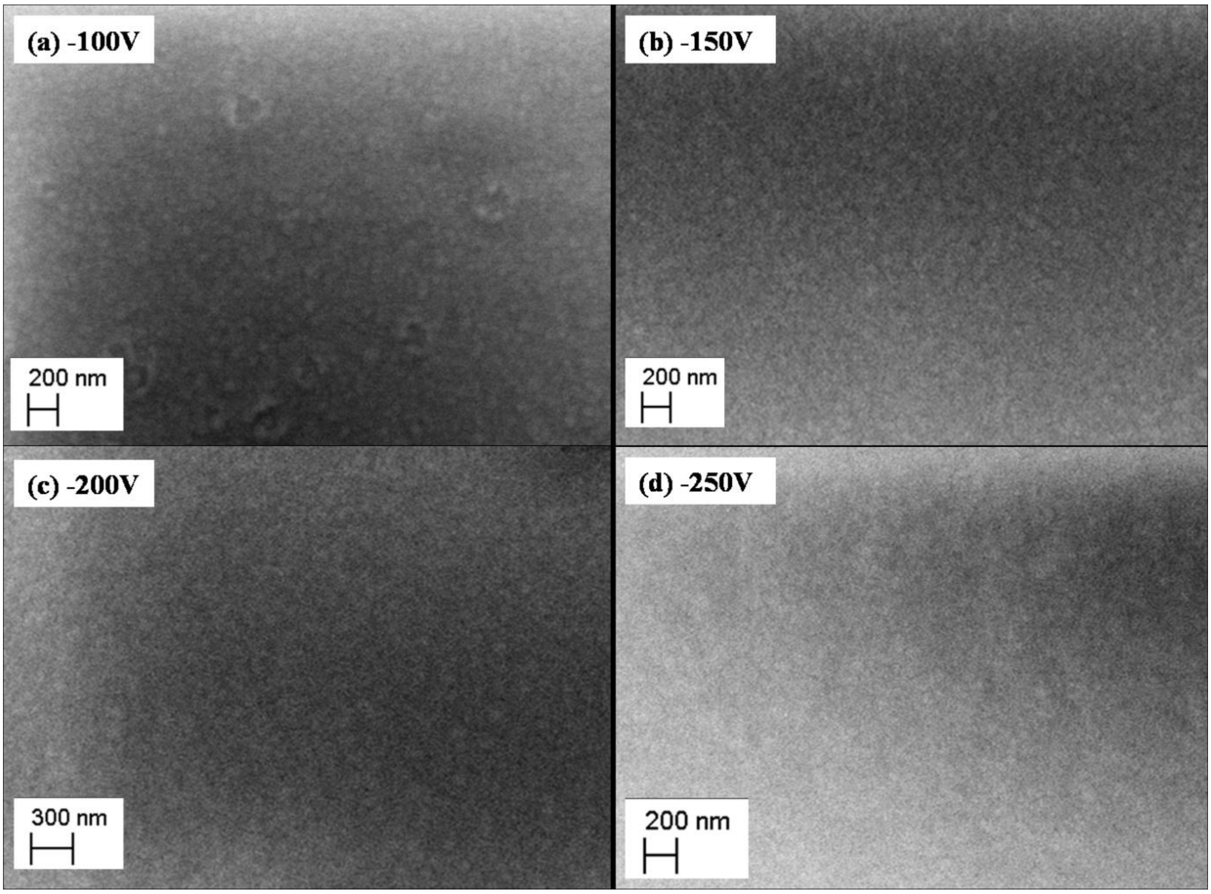

Figure 4.9: FESEM micrographs of $^{nat}B_xC$ thin films deposited at (a) -100V, (b) -150V, (c) -200V, and (d) -250V self-bias values.

4.4 Discussion:

In PECVD, various process parameters are responsible for determining material properties as well as deposition rates. Multiple process parameters such as input power, total chamber pressure, partial pressure of the reactants, gas flow rates, substrate temperature, spacing between the electrodes, discharge frequency etc. can be controlled to determine film stoichiometry [110]. The biasing parameters are especially the key factors in determining energy distribution of ions impinging on film surface during film growth. When a highly energetic ion is incident on the film surface, it collides with the surface atoms of the growing film and displaces them from their initial sites. The displacement of even a single surface bonded atom can affect the arrangement of its neighbouring atoms resulting in change in the structure of the growing film. If the energy of the impinging ions is significantly higher, it can even cause re-sputtering of the growing film [111, 112]. In our study, substrate self-bias was found to play a key role in determining film growth kinetics, hence structure and properties of the samples.

Boron carbide has a rather complex structure and is found to exist in a wide stoichiometric range as mentioned earlier. Distinguishing various phases of boron carbide by XRD is rather difficult as structural variations are very small in its rhombohedral unit cell for different stoichiometric configurations [5], hence a careful observation is required to identify different phases. In this study, typically XRD patterns correspond to rhombohedral B_4C and orthorhombic B_2O_3 (310) phases. In XRD scans of our samples, intensity of the B_4C (012) peak is much weaker as compared to other two peaks, yet its presence could be confirmed for all the samples (Figure 4.2). The B_4C (110) phase is the most dominant phase in the films as the peak has the highest intensity and it was also found to increase with substrate self-bias. Grain size in each film, calculated from XRD patterns (Equation 4.1 and Table 4.1) was found to decrease with substrate self-bias. Lower grain size facilitates higher packing density of grains. This results in increased density of the films [113] as seen in our previous study where an increase in areal density of atoms were observed on account of higher impinging ion energy [78]. Higher packing density of the grains corroborates increase in refractive index of the films with substrate self-bias as seen in Table 4.1. FESEM micrographs also reveal information about the grain size variation in the films. Though accurate particle size measurement was not possible from the micrographs, it can be clearly observed that the grain size is less than 100 nm for the films. The grain size also seems to decrease as the film surfaces appear to be smoother with increasing bias which corroborates our findings from XRD scans.

p-EBS measurement results revealed that films deposited at comparatively lower substrate self-bias (-100 V and -150 V) have higher B/C ratio and the ones deposited at higher substrate self-bias (-200 V and -250 V) have a lower B/C ratio. A considerable amount of oxygen impurity can be seen in the films due to presence of residual gases in the plasma reactor during deposition. The residual oxygen plays a substantial role in bonding. Oxygen being highly reactive upon dissociation, bonds easily with boron and carbon and forms oxy-boron carbide and/or B_2O_3 impurity species [78]. Incorporation of oxygen in the bulk of boron carbide films can disturb the lattice structure, resulting formation of amorphous films [114]. The oxygen impurities can also modify the electronic band structure of a material significantly. If the oxy- boron carbides and/ or oxides in the films had prominent effect on the optical properties, then the refractive index would have been lower than the measured value as it is reported that the typical refractive index of B_2O_3 is 1.64 [115]. However, in our samples oxide impurities in particular did not significantly affect the optical properties of ^{nat}boron carbide films as the measured band gap, refractive index and other optical constants are found to be comparable with the previously published reports for boron carbide films as discussed later in this section.

When the deposited ^{nat}boron carbide films are characterized independently via XRD and p-EBS technique for determination of film stoichiometry, the results come out to be slightly different. This might be a consequence of mixed phase growth during thin film deposition. Mixed phase growth is a common phenomenon of PECVD process [116] and during deposition it could have happened that along with the crystalline B_4C phase, some other microcrystalline and amorphous phases have also been deposited. p-EBS measurement provides a bulk average considering all the phases, crystalline and amorphous, whereas XRD peaks mainly correspond to the crystalline phases. This could be the reason behind difference in stoichiometry as determined by p-EBS and XRD technique.

The refractive index (n), extinction co-efficient (k), and absorption co-efficient (α) spectra of ^{nat}boron carbide thin films are shown in Figure 4.4, Figure 4.5 and Figure 4.6, respectively. Measured refractive index values agree reasonably with the values reported earlier [59, 117]. The refractive index of the films at a typical wavelength of 400 nm is found to increase from 1.87 to 1.97 with increasing substrate self-bias. For deposition at higher self-bias, the surface mobility of the deposited atoms increases owing to increased impinging ion energy, which results in compact films with fine grains. Thus, higher substrate self-bias results in denser films which can account for increase in refractive index. The value of extinction co-efficient at a typical wavelength of 400 nm also increases with the increase of substrate self-bias. B/C ratio listed in Table 4.1 show that the films are super stoichiometric for lower substrate self-bias, while they are sub stoichiometric for higher self-bias. Super stoichiometric films in general have been reported to have lower extinction co-efficient than films with preferred stoichiometry, hence are more transparent [118] which was also observed in our experimental findings.

Optical absorption spectrum is widely used to estimate the energy gap of a material. Absorption co-efficient (α) of amorphous semiconductors tend to follow an exponential law in the high absorption region ($\alpha \geq 10^4 cm^{-1}$) [119]. In a crystalline or polycrystalline material, both direct and indirect band transitions can take place depending upon the band structure of the material as well as the energy of incoming radiation. From Tauc plots, the direct and indirect band gap of the ^{nat}boron carbide thin films was evaluated. Our samples shows a continuous decrease of direct bandgap from 3.87 eV to 3.48 eV and indirect bandgap ranging from 2.74 eV to 2.02 eV with increase in substrate self-bias as seen in Figure 4.7(a) and (b). It is reported that $^{nat}B_xC$ thin films with higher boron concentration exhibits higher optical band gap, hence higher transperancy than the films with lower boron concentration [25]. Thus both p-EBS and optical characterization results of our samples confirm the fact that optical band gap is related to the composition of the $^{nat}B_xC$ thin films which is consistent with findings of other groups [3, 7].

Table 4.1 shows that film thickness decreases with increasing substrate self-bias. This implies a decrease in deposition rate, as deposition time for all the samples were kept constant. As discussed in previous chapter (chapter 3, section 3.4), film thickness decreases mainly on account of two competing phenomenon: increase in deposition rate due to increased fragmentation of gas phase precursor at higher self-bias, and enhanced rate of re-sputtering of deposited material [78]. Film compaction due to reduced grain size at higher impinging ion energy can also contribute to the decreased film thickness.

Generally, transmission increases with decreasing film thickness for fixed reflection, absorption and scattering losses. But sometimes, the films may possess absorbing defects due to deposition process parameters. As a result the absorption loss factor increases. Film reflectivity increases with increasing refractive index. Rough film surface, as well as, poor interface increases the scattering loss factor. Owing to these factors, even a film having lower thickness may show lower transmission. For $^{nat}B_xC$ thin films, the refractive index and absorption co-efficient increases with increasing substrate self-bias, hence both reflection and absorption of the film increase, which leads to decreasing transmission. The scattering loss may also increase with substrate self-bias due to higher surface and interface roughness, ultimately contributing to the reduced film transmission. Therefore, for our thin film samples, the transmission is not primarily dependent on thickness of the films.

X-ray reflectivity of different $^{nat}B_xC$ samples measured in a synchrotron radiation source showed that -200 V film exhibits a maximum of 81% grazing angle reflectivity (Figure 4.8) near the K_α edge of boron (67.6 Å) which is comparable with the findings of other groups [103, 104]. The reflectivity decreases slightly above the boron K_α edge for all the samples signifying increasing absorption above these values. Increased X-ray absorption and degradation of the films at higher self-bias could be the reason for decreased soft X-ray reflectivity of -250 V film. It is therefore evident from our soft X-ray reflectivity results that the ^{nat}boron carbide thin films deposited at optimal experimental conditions can be used as optical reflectors due to their reasonable grazing angle reflectivity. Single and multilayer mirrors having a low Z-element such as boron and a metal as optical elements finds application in both the soft-x-ray spectral range, as well as, at higher photon energies [104]. Therefore, boron carbide has the potential to be used as a spacing layer in a multilayer arrangement or in a single layer mirror arrangement in this spectral region of critical significance.

4.5 Summary:

Our present work reports variation in microstructure and optical properties with composition of $^{nat}B_xC$ thin films prepared by PECVD at different substrate self-bias values. Films were optically characterized by spectrophotometry and soft X-ray reflectivity measurements. Microstructure and composition of the films were determined by XRD, FESEM, and p-EBS measurements. Detailed characterization results reveal that grain size decreases with self-bias resulting in denser films. Refractive index of the films was found to increase at a typical wavelength (400 nm) as a result of increased packing density with substrate self-bias. Bandgap was related to the carbon concentration in the films and both the direct and indirect bandgap was found to decrease with increase in carbon content. Thus, in order to get denser films with higher refractive index, comparatively higher substrate self-bias is preferable. But there is an optimum value of self-bias as the optical properties of the -250 V film is found be inferior as compared to all other films. All these films also exhibit reasonable grazing angle soft X-ray reflectivity in the wavelength range 40 Å – 360 Å, therefore holding promise as optical material for this region of electromagnetic spectrum.

Chapter 5 : Tribological properties of RF-PECVD deposited ^{nat}boron carbide ($^{nat}B_xC$) thin films on stainless steel

---

5.1 Introduction:

Investigation of tribological properties of a material or thin film coating is necessary to evaluate their acceptability for various engineering applications. During tribological applications, these materials are usually exposed to high surface pressure and sliding velocities, therefore experience mild to severe wear depending on the operating conditions. Wear can even affect the performance of hardest of materials including diamond. Therefore, identifying suitable material or material-lubricant combination for specific applications becomes absolutely necessary for superior performance, and durability. Tribological evaluation of materials is an integral part of modern day engineering industry. It is essentially the study of friction and wear behavior of two interacting material surfaces in relative motion. Often solid, liquid, or gaseous lubrication is used to reduce friction, and control wear between two surfaces [120] in contact. Use of coatings over one or both the surfaces in contact to improve tribological properties is an effective and relatively economical method of solid lubrication, which can significantly enhance the tribological performance of engineering materials [121]. Since the tribo-coatings are subjected to considerable amount of external stress, they must possess good adhesion, and high thermal stability to provide better performance [122]. Selection of appropriate thin film coating suitable for a particular application is quite tricky as response of a coating- counter material system under tribologically stressed condition is complicated and depends on various factors including the properties of the thin films and the counterparts, operating conditions, substrate, and the interface.

Increased tribological demands of present day industries have necessitated a search for functional solid lubricants. As a result, many new deposition techniques and various tribological materials are being investigated, providing the users with an opportunity with a selection of the materials. In terms of commercial application of these tribological thin films, a major goal was achieved with the use of titanium carbide, and titanium nitride thin films as protective tribological coatings on cutting tools [123], since then a number of materials have been investigated. Boron carbide as a candidate material is attractive because of its unique blend of physical and chemical properties. Its physical properties like low density (2520 kg/ m^3), low thermal expansion co-efficient, high hardness (~ 40 GPa), and chemical stability makes it a suitable candidate for different tribo-mechanical applications [124]. It has found many industrial applications as protective coatings on cutting tools, automobile components, military armor, and for aerospace applications [2]. Under certain conditions where tribologically stressed components cannot be lubricated by other thin films because of the flash heating of the surfaces in contact and associated tribochemical effects [125], boron carbide as a protective tribological coating becomes extremely useful by virtue of its high thermal stability.

Various physical vapor deposition (PVD) and chemical vapor deposition (CVD) techniques have been employed [126-128] for synthesis of boron carbide thin films including plasma enhanced chemical vapor deposition (PECVD) technique [129, 130]. Several reports recording tribological response of magnetron sputter deposited boron carbide thin films exist [131-135]. Most of the studies reported have dealt with tribological response of magnetron sputter deposited boron carbide thin films. As far as PECVD deposited $^{nat}B_xC$ films are concerned, there is a scarcity of report presenting the tribological behaviour of such films and their dependence on the PECVD deposition parameters. CVD techniques are preferred for deposition of thin films as these deposition processes allow a wide selection of materials in different compositions like carbides, nitrides, oxides etc. and forms such as nanostructures, crystalline, polycrystalline and amorphous [136, 137]. As mentioned in earlier chapters, PECVD is advantageous over other CVD techniques because it can provide uniform coverage on substrates having complex geometry with increased adhesion [4]. Also, physical and chemical properties of the film can be easily controlled by adjusting deposition parameters [78] during PECVD.

Study of tribological processes involving two surfaces in relative motion is complex as it includes friction, wear, and deformation mechanisms at different length scales. In our study we analyzed tribological properties of the $^{nat}B_xC$ - SS 316 thin film- substrate system under three different applied normal load values. Efforts were made to investigate the effect of composition and thickness of the ^{nat}boron carbide ($^{nat}B_xC$) thin films on the measured tribological properties. A careful analysis of the characterization results provided the opportunity to optimize properties of the $^{nat}B_xC$ thin film coatings in order to achieve the required friction and wear performance.

5.2 Materials and methods:

5.2.1 Deposition of ^{nat}boron carbide ($^{nat}B_xC$) thin films:

A fixed frequency (13.56 MHz) capacitively coupled RF-PECVD system was used to deposit the ^{nat}boron carbide ($^{nat}B_xC$) thin films using a single source solid precursor o-carborane (o-$C_2B_{10}H_{12}$) (99.99% pure). Details of the components of the PECVD system and schematic of the deposition system have been described elsewhere [78] (chapter 2, section 2.1.1.). Two separate sets involving three films in each set were deposited on SS 316 (stainless steel) discs ($24\,mm$ diameter, $8\,mm$ thickness, composition: carbon 0.08 wt.%, chromium 18 wt.%, manganese 2 wt.%, silicon 0.75 wt.%, phosphorous 0.045 wt.%, sulphur 0.03 wt.%, nickel: 10-14 wt.%, molybdenum: 2-3 wt.%, nitrogen 0.1 wt.%, iron: balance) under defined deposition conditions. Relevant substrate cleaning procedures followed are discussed in details in section 2.3 of chapter 2. Typical surface roughness of the stainless steel discs was around 40 nm. For preparation of first set of samples DC substrate self-bias was chosen as control parameter and deposition runs were carried out at substrate bias of -75, -125, and -175 V, respectively. In the next set, only deposition time was varied to obtain films of different thickness, keeping all other parameters constant during each deposition run. For a fixed value of substrate self-bias -175 V, three deposition runs were conducted for 10, 20, and 30 minutes of deposition times to achieve variation in film thickness. Prior to each deposition run, the SS substrates were sputter cleaned in Ar Plasma for 20 minutes at 2×10^{-2} mbar chamber pressure. Depositions were carried out in He plasma post sputter cleaning. The total chamber pressure during deposition was 3×10^{-2} mbar. For both sputtering and deposition, laboratory grade 99.8% pure gases were used.

5.2.2 Characterization:

Film thicknesses were measured by Taylor Hobson 3D optical profilometer (Green light, Resolution 0.1 Å). Area and volume (V) of wear tracks were also estimated utilizing the same profilometer. Morphology of the wear tracks were investigated in a desktop mini scanning electron microscope (SEM) (Model SNE 3000M, SEC engineering, Korea) for 200X and 500X magnification. Film structures were determined by X-ray diffraction (XRD) (RIGAKU make) analysis in Bragg-Brentano geometry with 2θ angle in the range of 20°-30° in angular steps of 0.02° using Cu-K_{α} (λ=1.5406 Å) radiation. Grain size was calculated from XRD peaks using Scherrer's equation (equation 4.1). Proton elastic backscattering spectrometry (p-EBS) has been employed to determine composition of the films. The measurements have been performed using 2.0 – 3.0 MeV proton beam obtained from a 3 MV Tandetron, for normal incidence on the sample surface. Atomic percentages of boron, carbon and oxygen in the film were calculated from the p-EBS data and from that boron to carbon (B/C) ratio was determined.

5.2.3 Tribological characterization:

Wear and friction performance of the as-deposited ${}^{nat}B_xC$ films were probed by a reciprocating tribometer using a conventional ball on disc configuration (TE-70, Phoneix Tribology Ltd, UK). The stainless steel substrate - ${}^{nat}B_xC$ thin film coating system and the chrome steel ball counterpart (SS52100, composition: carbon 0.95-1.10 wt.%, chromium 1.30-1.60 wt.%, manganese 0.25-0.45 wt.%, silicon 0.15-0.35 wt.%, phosphorous 0.025 wt.% max., sulphur 0.025 wt.% max.) was subjected to relative oscillatory movement keeping the oscillation frequency at 5 Hz and angle of displacement of 15° during each measurement. Sliding tests were performed at ambience in dry lubricated conditions at 5, 10, and 15 N applied normal load values for 15 minutes and 4500 sliding cycles. Tests were performed in ambience with humidity ~ 70% and temperature 27°C. Specific wear rate W_s was calculated from the following relationship,

$$W_s = \frac{V}{FL}\left(\frac{mm^3}{Nm}\right) \quad \ldots\ldots\ldots\ldots\ldots\ldots\ldots\ldots\ldots\ldots(5.1)$$

Where, L is total sliding distance, F is the applied normal load, and V is the volume of wear tracks. Surface hardness was measured using micro-hardness measurement equipment (Future Tech FM-7 model) using Knoop method as it is particularly suitable for thin specimen and for testing of brittle material. Measurements were performed using a Knoop indenter at 0.25 N applied normal load. Dwell time for each of the measurements was kept 10 seconds. For each sample, hardness measurement was performed under ambient condition (atmospheric pressure, 300 K temperature and 70% relative humidity) at five different locations on the sample surface and an average value of hardness was calculated. Hardness is expressed in terms of Knoop's hardness number (HK) calculated with the help of the following expression:

$$HK = \frac{14.229\,F}{D^2} \quad \ldots\ldots\ldots\ldots\ldots\ldots\ldots\ldots\ldots\ldots\ldots(5.2)$$

Where, $F =$ Applied Load, $D =$ Length of the indentation along its long axis, and 14.229 is a correction factor related to the shape of the indenter.

5.3 Results:

5.3.1 Film thickness and surface roughness:

Our 3D optical profilometry measurement results showed that films deposited at -75 and -125 V had thicknesses of 2.5 µm, while film deposited at -175 V had a thickness ~ 3 µm. Films deposited at a fixed substrate bias voltage (-175 V) but for different duration had different thicknesses as expected. Measured film thicknesses as a function of time for -175 V films are 0.5, 1.5 and 3 µm respectively. Surface roughness of the films was also obtained by defining a line profile on the thin film side during the profilometry measurement and these values are listed in Table 5.1. It can be seen that as we go from lower to higher substrate self-bias values, the surface roughness decreases. Also increase in film thickness from 0.5 to 3 µm improves the surface roughness.

5.3.2 Microhardness:

Hardness of the films was measured by the micro-hardness tester and represented by Knoop’s hardness number (HK) given in Table 5.1. Substrate self-bias and also film thickness were found to have prominent influence on hardness of the $^{nat}B_xC$ films. Films deposited at a higher substrate self-bias (-175 V) was found to have lower hardness ~ 2000 HK, compared to the ones deposited at lower substrate self-bias values (2800 HK for -75V film and 2368 HK for -125 V film). Also, films having similar composition as a result of being deposited at same substrate self-bias value -175 V but of different thickness, exhibit similar hardness values ~ 2000 HK except for the one having lowest thickness (0.5 µm) where HK ~ 1500.

5.3.3 Structure and grain size:

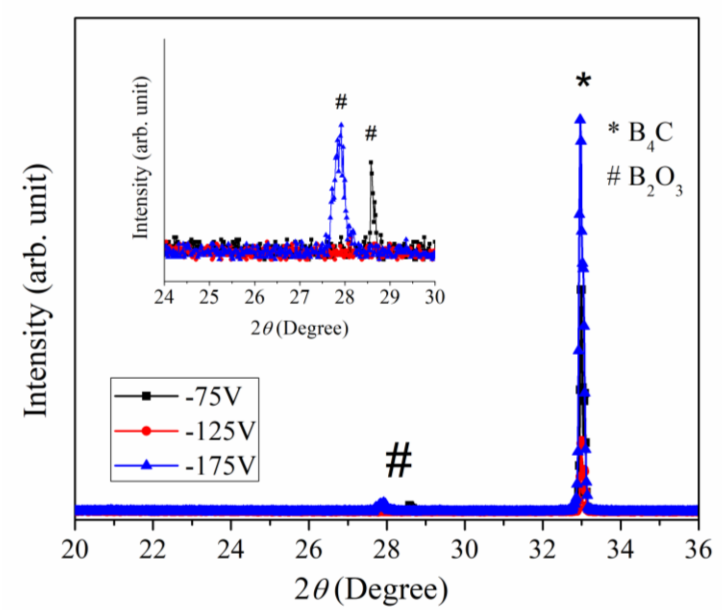

Figure 5.1: XRD diffractogram of $^{nat}B_xC$ thin films deposited at different substrate self-bias. The inset plot shows enlarged XRD diffractogram for $\mathbf{2\theta}$ ranging from $\mathbf{24^\circ - 30^\circ}$.

XRD scans of $^{nat}B_xC$ thin films are shown in Figure 5.1. Two distinct sets of peaks located near 2θ values 28° and 33° appear in the XRD patterns. All peaks were identified via search-match comparison with standard JCPDS-ICCD database and the closest match was found with JCPDS file nos. $\#44-1206, \#75-0424$, and $\#06-0297$. Peaks located at 33° represents rhombohedral boron carbide ($B_{10}C$ (021) and/ or B_4C (110)) phases and the ones near 28° belong to cubic boron oxide (B_2O_3 (310)) phases. Slight shift can be observed in oxide peak positions located near 28° for different samples. Peaks representing boron carbide ($^{nat}B_xC$) phases were the most dominant peaks for all the films as compared to the boron oxide peaks.

Average grain size for these microcrystalline phases was estimated using Scherrer's equation (equation 4.1). FWHM of the peak at 33° was considered for grain size calculation as it was the most intense peak for all films characterized via XRD. Calculated gain size is listed in Table 5.1 which shows decrease in grain size with increasing self-bias value.

5.3.4 Film composition:

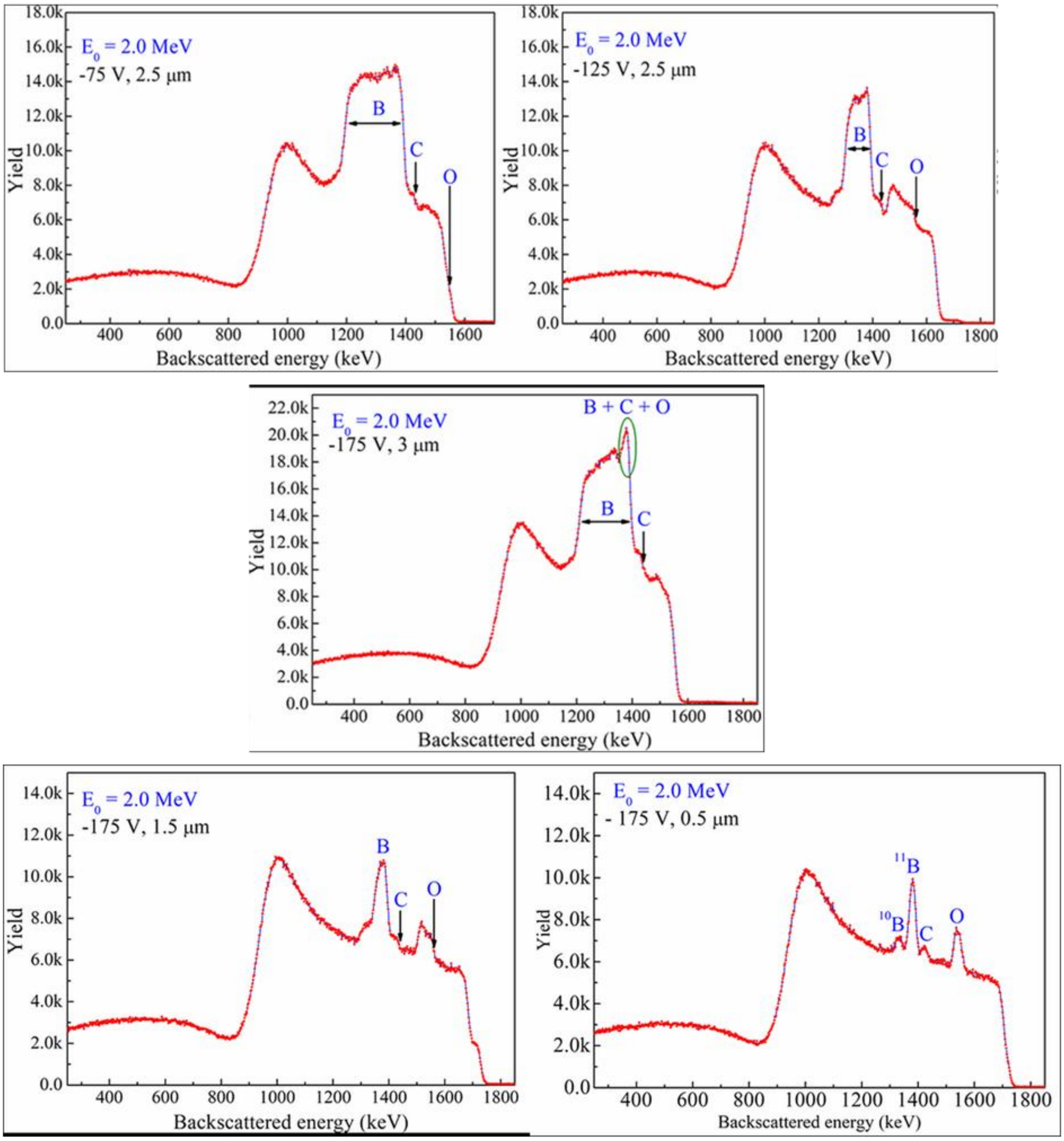

Figure 5.2: Typical Energy profiles of the p-EBS spectra for all $^{nat}B_xC$ samples.

Atomic percentages of the constituent elements of $^{nat}B_xC$ films, boron and carbon and also oxygen impurities in the bulk were determined by p-EBS technique. Typical p- EBS energy profiles for the samples are shown in Figure 5.2. Composition measurement results from this analysis are listed in Table 5.1 and Figures 5.3(a), (b), and (c). It can be seen that films deposited at lower substrate self-bias possess higher B/C ratio, offering a maximum of 9.95 at -125 V. Films deposited at -175 V self-bias possesses comparatively lower B/C ratio (~ 4). Such variation in film stoichiometry as a function of substrate self-bias is in agreement with our previous findings [78, 138]. For the set of films having different film thicknesses deposited at -175 V self-bias, film having 0.5 μm thickness offers B/C ratio as low as 3.69. Other two films having film thickness 1.5 and 3 μm have B/C ratios 4.65 and 3.75 respectively. Hence, for the same substrate self-bias values -175 V, slight variation in film stoichiometry was observed.

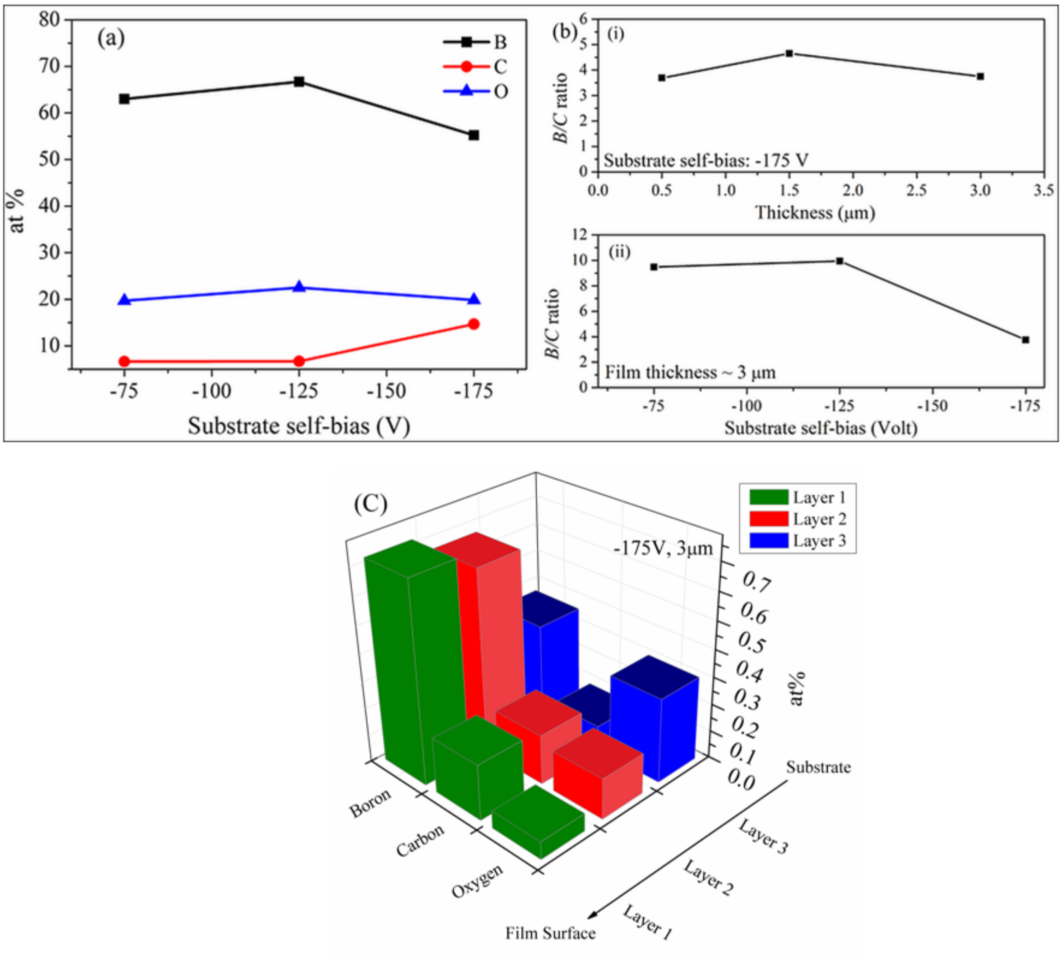

Figure 5.3: (a) Atomic percentage of elements in the ^{nat}boron carbide thin films determined via p-EBS technique, (b) Variation in B/C ratio in the films with (i) film thickness and (ii) substrate self-bias, and (c) Typical variation of boron, carbon and oxygen in the bulk layers of -175 V, 3 μm film.

Figure 5.3(a) depicts variation of atomic percentage of boron, carbon, and oxygen in the bulk of the films as a function of substrate self- bias. Significant oxygen impurity can be seen to be present in the bulk of the films (Figure 5.3(a)). Variation of B/C ratio as a function of film thickness and substrate self-bias is shown in Figure 5.3(b). A typical distribution of the constituent elements boron, carbon and oxygen within different bulk layers of a film deposited at a typical self-bias value of -175 V having 3 μm thickness is shown in Figure 5.3(c). To find out the homogeneity of the composition in the bulk, this layer-wise analysis of the thin film was performed. Three different layers was considered: Layer 1 was taken as the one starting from the film surface and extended to the bulk, Layer 2 was the pristine bulk layer, and Layer 3 was the one starting from the bulk and reaching the substrate. The atomic percentage of carbon is more in Layer 1 as this layer is in contact with the ambiance directly, as seen in Figure 5.3 (c). The substrate surface always tends to have a native oxygen layer and even after substrate cleaning, tiny amount of that native oxygen layer still tends to exist on the substrate surface. That is why the relative atomic percentage of oxygen can be seen to be higher in Layer 3, which is in direct contact with the substrate surface. The overall uncertainty in p-EBS measurement is taken as 5% [106]. Apart from B, C and O, presence of slight amount of hydrogen is expected in the films as seen in one of our earlier investigations [78].

Table 5.1: Comparison of composition, microstructure, thickness, and tribological properties of PECVD deposited $^{nat}B_xC$ thin films.

Variables		% B	% C	B/C ratio	Knoop Hardness No. (HK)	Surface Roughness of the films (nm)	Grain Size (nm)
Substrate self-bias (in Volt)	-75V	63	6.65	9.47	2799	74	71
	-125V	66.7	6.7	9.95	2368	105	69
	-175V	55.2	14.7	3.75	2021	15	65
Film Thickness (μm) (at fixed substrate self-bias -175 V)	0.5 μm	43.6	11.8	3.69	1560	24	-
	1.5 μm	40.2	8.64	4.65	1980	12	-
	3 μm	55.2	14.7	3.75	2021	15	65

5.3.5 Tribological properties:

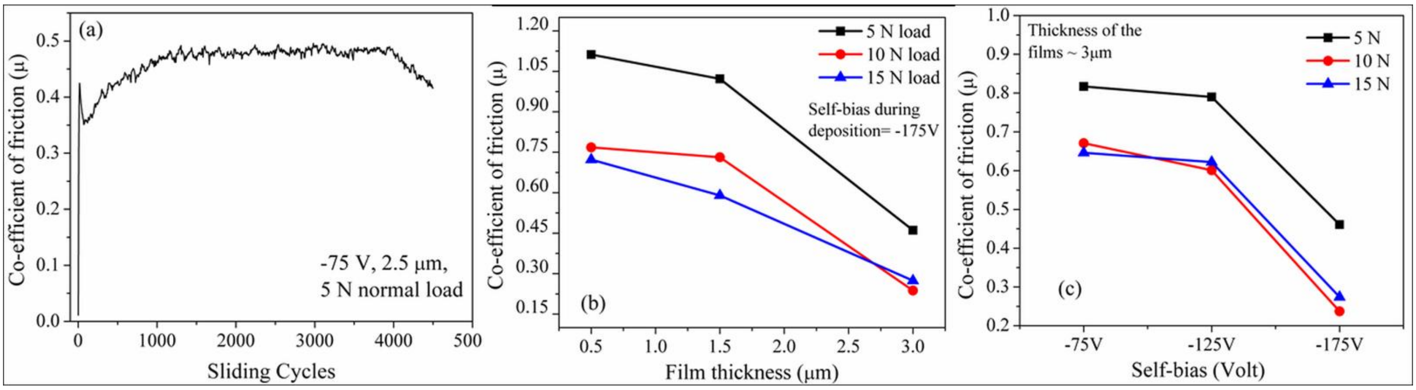

Figure 5.4: (a) Typical evolution of co-efficient of friction with sliding cycles for -75 V, 2.5 μm film, Variation of co-efficient of friction with (b) film thickness and (c) substrate self-bias at different load values.

5.3.5.1 Coefficient of friction (COF):

For determination of tribological properties of $^{nat}B_xC$ films, ball on disc sliding measurements were performed under dry lubricated conditions in ambience with chrome steel ball counterpart and the results are shown in Figure(s) 5.4, 5.5, and 5.6. Deposition parameters; substrate self-bias and deposition time were found to have significant effect on the co-efficient of friction (COF) and wear rate of the thin film coatings. Figure 5.4(a) represents typical variation of COF over 4500 sliding cycles for film deposited at -75 V self-bias having 2.5 µm thickness under 5 N of applied vertical load. It is observed that COF increases gradually from the initial value of 0.35 till 1200 sliding cycles and then stabilizes around 0.45. It can be seen in Figure 5.4(b) that COF decreases with increasing film thickness for each load value. Also, for films having comparable thickness, the friction co-efficient is found to decrease with increasing substrate self-bias, for each load value (Figure 5.4(c)). For a particular film thickness and/ or fixed substrate self-bias value, COF was found to decrease with increasing external load (5 - 15 N).

5.3.5.2 Wear rate:

Effect of applied normal load on total wear volume after 4500 oscillation cycles is shown in Figure(s). 5.5(a), and (b). Figure 5.5(a) shows that $^{nat}B_xC$ films deposited at same substrate self-bias (-175 V), having different film thickness have different wear volumes. Moreover, wear volume was found to increase with increasing load from 5 N to 15 N, irrespective of film thicknesses. The -175 V film having 1.5 µm thickness shows highest wear with wear volume $9.999 \times 10^{-3}\ mm^3$ at 15 N load. The -175 V film having 0.5 µm thickness exhibits lowest wear having wear volume $2.07 \times 10^{-3} mm^3$ at 5 N load. This is simply because at this film thickness there is not enough material, i.e. ^{nat}boron carbide for the counter material to remove before it sees the substrate. Consequently the wear volume is lowest. Figure 5.5(b) represents variation of wear volume in $^{nat}B_xC$ films having comparable thickness (~ 3 µm) but different film composition. For -75 V film, at all applied load values, no wear track was seen under microscope; therefore wear volume could not be measured. Film deposited at -175 V self-bias shows lower wear volume for each load value, $i.e. 2.219 \times 10^{-3} mm^3$ at 10 N and $4.533 \times 10^{-3} mm^3$ at 15 N load in comparison with -125 V film. From the value of wear volumes, specific wear rate was calculated using equation 5.1.

Variation in specific wear rate, as a function of applied vertical load for different film thickness and substrate self-bias values are shown in Figure(s) 5.6(a) and (b), respectively.

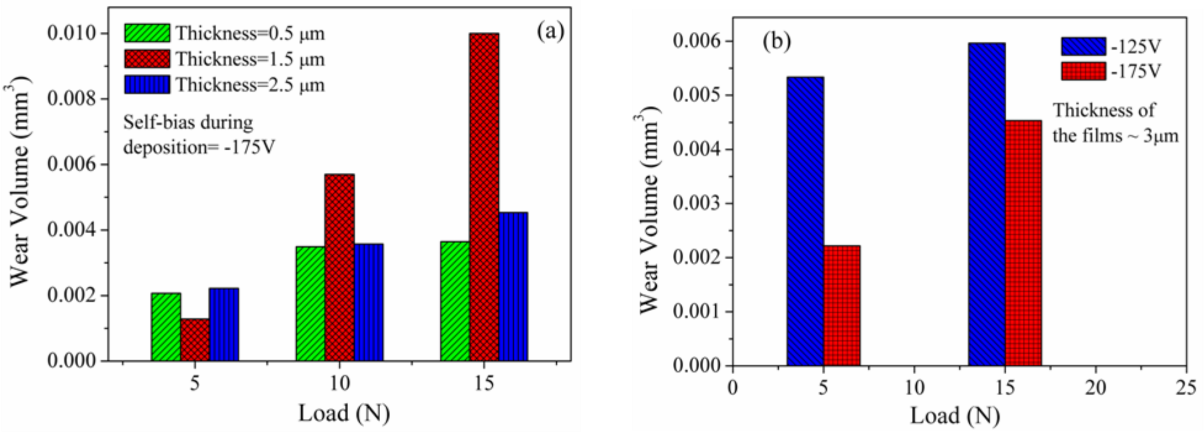

Figure 5.5: Change in wear volume with applied load at different (a) film thickness and (b) different self-bias values.

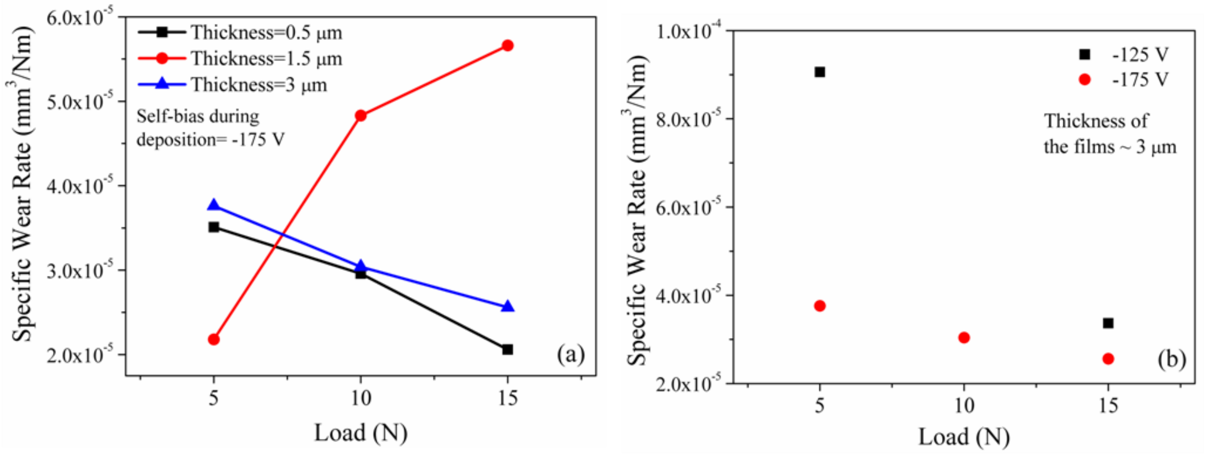

Figure 5.6: Variation in specific wear rate with applied normal load (a) for films of similar composition but different thickness and (b) for films deposited at different self-bias values having similar thicknesses.

The plots (Figure 5.6(a)) show that for film thicknesses 0.5 μm and 3 μm the specific wear rate decreases with increasing applied normal load. However for 1.5 μm film, the specific wear rate increases with increasing load from $2.18 \times 10^{-5}\, mm^3/Nm$ at 5 N to $5.66 \times 10^{-5}\, mm^3/Nm$ at 15N. The 0.5 μm film exhibits lowest wear rate at all applied normal load values; $3.51 \times 10^{-5}\, mm^3/Nm$ at 5 N, $2.96 \times 10^{-5}\, mm^3/Nm$ at 10 N and $2.06 \times 10^{-5}\, mm^3/Nm$ at 15 N respectively. With reference to Figure 5.6(b), the -125 and -175 V film having comparable thickness shows decrease in wear rate with increased load from 5 to 15 N. For 10 N load value, no wear mark was seen in -125 V sample, therefore wear rates of -125 and -175 V film could not be compared for that particular load. Also, for -75 V film, since no wear tracks were formed on the surface during ball on disc measurement, measurement of wear volume and calculation of wear rate was not possible as mentioned earlier.

5.3.5.3 Optical micrographs of the wear tracks:

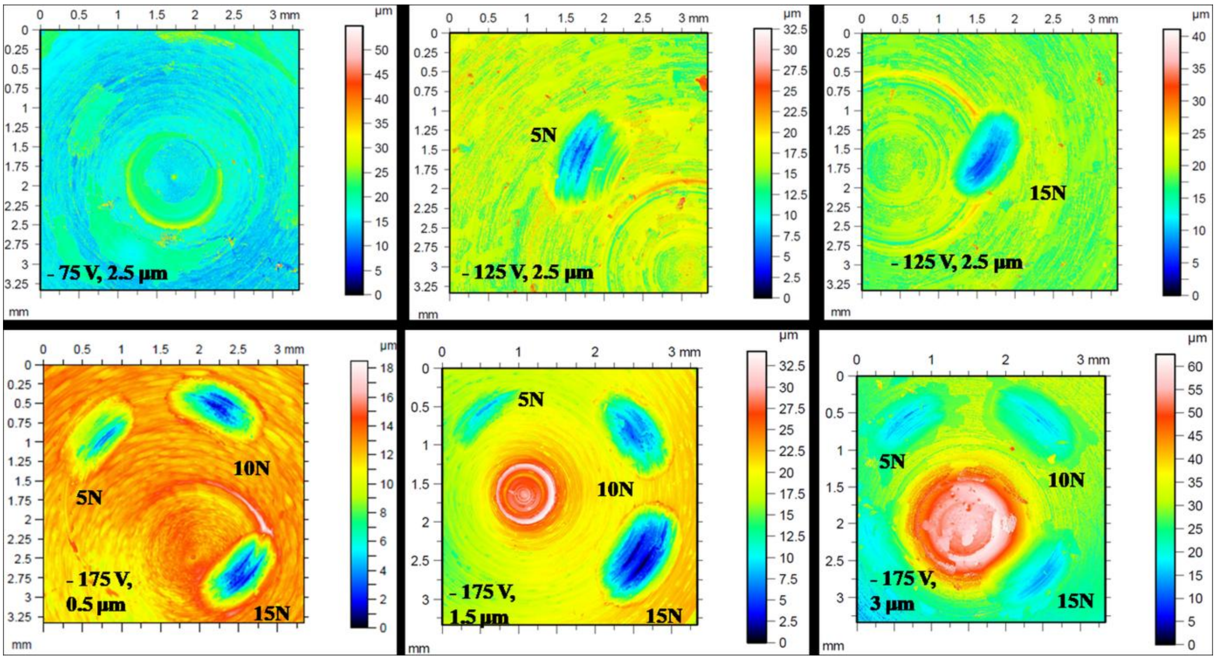

Figure 5.7: Optical micrographs of wear tracks on the ${}^{nat}B_xC$ sample surface.

Optical micrographs of the worn surfaces are shown in Figure 1. For -75 V film, no wear track formation can be seen for all applied vertical load values during tribological measurements. For -125 V film, the wear tracks corresponding to 5 and 15 N applied load values can be seen clearly, however for 10 N load, no wear track formation was seen. For -

175 V samples, for all three different thicknesses, wear tracks were present for each load values.

5.3.5.4 Morphology of the wear tracks in dry lubricated conditions:

From the SEM micrographs of the wear tracks on the sample surfaces (Figure(s). 5.8(a), (b), and (c)), dominant wear mechanisms were identified. In Figure 5.8(a), for film deposited at -75 V, original machining marks were visible. No distinct wear marks were seen, indicating very low or nil wear. However some chips/ wear debris are visible on the surface which can accumulate due to the transfer of counter-face material *i.e.* chrome steel ball as a result of abrasive wear. Figure 5.8(b) represents worn surfaces of -125 and -175 V samples at different applied normal load values. For films deposited at different bias values (-125 and -175 V), wear mechanisms are somewhat different at 5 and 15 N loads. Dominant wear mechanism for -125 V sample at 5 and 15 N load is abrasion and de-lamination wear coupled with some crack formation, while the dominant wear mechanism for -175 V sample at 5 N load (Figure 8(b)) is indicating ploughing and wedge formation with some crack formation in the $^{nat}B_xC$ thin film. For 15 N load, the dominant wear mechanisms for -175 V sample are de-lamination, coupled with polishing at some places. Presence of wear debris can be seen at different locations for all the samples. Figure 5.8(c) represents SEM micrographs of worn surfaces of -175 V $^{nat}B_xC$ films having different film thicknesses, for different applied normal load values. For 5 N normal load, the film of lowest thickness *i.e.* 0.5 μm shows de-lamination wear and cracking. As the thickness increase to 1.5 μm, the dominant wear mechanism changes to a combination of ploughing and wedge formation coupled with crack formation at some places. Primary wear mechanisms do not change as the film thickness is increased further to 3 μm. As the applied normal load is increased to 10 N, for 0.5 μm film, the cracking and de-lamination wear becomes more prominent. Some groove formation can also be noted in the samples. For 1.5 μm film, cracking and de-lamination along with abrasive wear becomes more pronounced at increased applied load. As the film thickness is increased further to 3 μm, some mild polishing at few locations can be observed along with abrasion and cracking. For the highest applied normal load value for our measurement *i.e.* 15 N, dominant wear mechanisms for 0.5 μm film is cracking and de-lamination. As the thickness is increased further to 1.5 μm, along with cracking and de-lamination wear, abrasive failure of the thin film coating is also visible. For 3 μm film, cracking and de-lamination is the prominent wear mechanism. For all the samples, for 15 N applied normal load value, mild polishing can be observed. After 4500 sliding cycles for each measurement, partial adhesive failure of the $^{nat}B_xC$ thin film coating can be observed for the all the applied vertical load values due to fatigue wear.

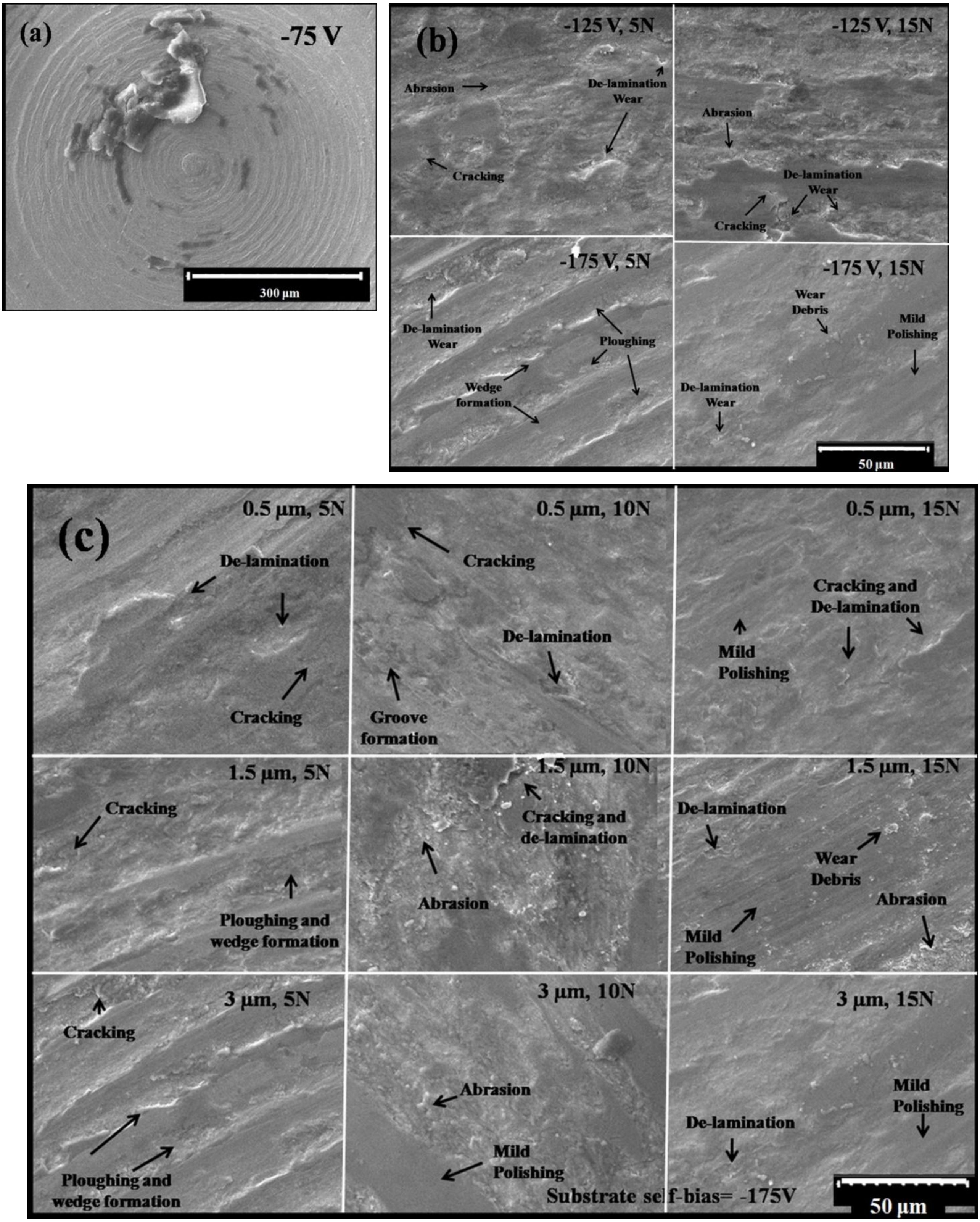

Figure 5.8: Typical SEM micrographs of worn surfaces of $^{nat}B_xC$ films deposited at (a) -75 V self-bias having 2.5 µm thickness, (b) -125 and -175 V self-bias values having comparable thickness, and (c) same self-bias value (-175 V) having different thicknesses.

5.4 Discussion:

It is established from our previous studies that thin film deposition techniques and process parameters have a significant effect on the properties of the as deposited films [139]. In this study, $^{nat}B_xC$ thin films have been deposited on SS 316 substrates by RF-PECVD technique. There are several deposition parameters in PECVD that can affect film properties [138]. For our study, two deposition parameters were chosen as independent variables: substrate self-bias and deposition time, for preparation of two set of $^{nat}B_xC$ films, keeping all other parameters undisturbed during each set of deposition runs. Tribological properties, composition, and structure of the films have been investigated with the help of requisite characterization techniques.

3D optical Results exhibit that (Table 5.1) film surfaces are smoother when deposited at higher substrate self-bias values owing to lower grain size. During nucleation and growth of the films on the substrate surface, high energy ion bombardment results in increase in areal density of atoms [78] which can account for decreased grain size, hence improved surface roughness [140].

To identify various crystalline phases, XRD peaks were matched with JCPDS-ICDD database which revealed that, along with rhombohedral boron carbide phase (Figure 5.2), cubic boron oxide (B_2O_3 (310)) phase is also present in the samples. Peak present at 33° corresponds to either $B_{10}C$ (021) phase and/ or B_4C (110) phase and deposition of this boron rich $B_{10}C$ stochiometric phase is confirmed by our p-EBS measurement results for -75 and -125 V films respectively. However, -175 V film mainly possess B_4C stochiometric phase of boron carbide. Comparatively high intensity of the diffraction peaks for -175 V film indicates a possible enhancement in crystallinity at higher self-bias values.

Composition measurement by p-EBS technique revealed deposition of stoichiometrically different films at each self-bias bias values, having higher B/C ratio at lower self-bias (B/C

~ 9.5 at - 75 V and B/C ~ 4 at -175 V) and vice versa, which is consistent with our previous findings [78, 138]. As already described earlier, boron carbide has a complex rhombohedral unit cell with 12 atomic icosahedral clusters at each of its vertices and 3 atomic linear chain along its body diagonal. To achieve boron rich boron carbide structures, carbon atoms must be replaced by boron atom either in icosahedra or in chain site. Also, this boron rich carbides can be formed by replacement of C–B–C and/ or C–B–B chains by a planar intericosahedron linking component (B4) group [141, 142]. Plasma, being a medium with high internal energy can assist in deposition of such boron rich polytypes of boron carbide. The films deposited at same self-bias -175 V having different thicknesses, exhibited a slight variation in composition with B/C ratios 3.75, 4.65, and 3.69 for film thicknesses 0.5, 1.5 and 3 µm respectively. Ideally, if all other deposition parameters including substrate self-bias is constant, the film composition should not change as a function of deposition time, hence film thickness. But, practically, achieving exact repeatability of plasma conditions in each deposition run is extremely difficult. Also, distribution of atoms in each layer of the films is different, giving inhomogeneity in composition of the films in bulk. These two factors can account for our obtaining stochiometrically different films for different film thicknesses (Table 5.1) at same substrate self-bias value. A typical variation in composition within different layers of the $^{nat}B_xC$ film is exhibited in Figure 5.4(c). Clearly, distribution of constituent elements boron and carbon is not uniform within different layers of the thin film. Presence of significant amount of oxygen impurity can also be seen in the bulk of the films (Figure 5.4(a)) which mostly gets incorporated from the residual gases in the plasma chamber during deposition. Oxygen being highly reactive dissociates and bonds easily with boron and carbon atoms and forms oxide phases. The presence of the oxide phase (B_2O_3) is also confirmed in the XRD data shown in Figure 5.2. Also, the surface of the films when exposed to the ambience, reacts with environmental moisture and forms boric acid over time which also enhances oxygen content in the films [143].

Presence of slight amount of hydrogen can be expected in the films originating from the precursor. In our earlier study we have observed signature of hydrogen bonding with boron atoms (~ $2600\ cm^{-1}$) via Fourier transform infrared (FTIR) spectroscopy [78], as shown in Figure 3.5 in chapter 3. In that study, it was found that the hydrogen content in the films mainly depends on the power coupled to the plasma during deposition, and this finding is similar to the one reported earlier by B. J. Nordell et al..[75]. In Figure 3.5, with increase in substrate self-bias, (hence increase in coupled power), the intensity of the B-H absorption peak decreased, indicating decrease in hydrogen incorporation in the films. It has also been reported earlier that a majority of the hydrogen atoms are removed during precursor fragmentation and re-sputtering of the deposited material in the highly energetic plasma environment [75, 144] which is consistent with our findings. Also, presence of significant amount of hydrogen in the thin films sample often makes the sample softer [145]. However, for our present samples, the -75 V film which possesses more hydrogen is found to have highest hardness and the -175 V film has shown lowest hardness [78] despite having lowest hydrogen content. It have been reported by researchers that, hydrogen incorporation changes wear behaviour of the material [143, 146]. Typically, the film with more hydrogen exhibits reduced COF [143, 146]. Contrarily in our samples; the-75V film having highest hydrogen content shows highest value of COF. Thus, it appears that the tribological behaviour of our samples is mostly dominated by the B/C composition and structural variation.

In our study, boron-rich stoichiometry is achieved at lower substrate self-bias. But areal density of atoms in the films increases at higher substrate self-bias [138] which should result in improved hardness. However, film hardness was found to decrease with increasing magnitude of self-bias having values 2799 HK at -75 V to 2021 HK at -175 V for films of thickness ~ 3 μm. It has been reported earlier that with increasing boron content, the micro-hardness of $^{nat}B_xC$ coatings increases [146] which is consistent with our findings. Also, it is seen in our previous study (Chapter 3) that during PECVD, at significantly higher substrate bias, highly energetic ion bombardment on the growing films results in defects and micro-crack formation [78, 100]. The degradation of the films at higher self-bias values and the sensitivity of micro-hardness measurement technique to micro-carcks [146] may be the reason behind the decreased film hardness at higher self-bias. Presence of oxygen impurity can also affect the hardness of the film remarkably. Due to its high electro-negativity, oxygen weakens the neighbouring bonds and gives rise to defects in the material, thereby reducing hardness [147].

Wear of a tribologically stressed system is not an inherent material property; it is a reaction of the tribosystem to the externally applied stresses which can drastically change with minute variation in dynamic experimental parameters, environmental parameters or material composition [148]. During the wear testing of the films, neither distinguishable wear marks were seen on the surface of -75 V $^{nat}B_xC$ film (Figure 5.8(a)), nor de-lamination of the film was observed during the tests. Therefore measurement of wear volume and calculation of wear rate was not possible for this particular sample. COF of $^{nat}B_xC$ films was found to decrease with increasing substrate self-bias (Figure 5.4(c)). This could have occurred on account of three possible factors: decreased surface roughness, increasing carbon content and possible formation of self-lubricating layer on the film surface. Our results exhibit that, by modifying process parameters, the COF can be reduced up to 0.23 for -175 V film, and this film has the lowest COF and specific wear rate (Figure 5.4(c) and Figure 5.6(b)) for each load value. During wear test, due to the tiny size of the indenter, flash temperatures can be generated at the point of contact whose magnitude can reach up to 1000°C [149]. Boron carbide being susceptible to oxidation even in ambience might get selectively oxidized locally at the point of contact due to elevated temperature and form boric acid. The boric acid could act as highly lubricating agent and help in reducing the COF of the $^{nat}B_xC$ films [125, 150]. It can be observed from Figure(s). 5.4(b), and (c) that films having higher thickness (~ 3 µm) exhibit lower COF. For comparison of wear rate of the films with thickness, the fatigue wear of the samples for the whole measurement cycle (4500 sliding cycles) must be considered. The fatigue life of thin protective films have been reported to be larger than thick films [123]. Under similar external stresses, thicker films will experience higher internal stress and might develop cracks with higher crack lengths, offering lower fatigue life as compared to the thinner ones. This could account for our observations of low specific wear rate of 0.5 µm thick -175 V $^{nat}B_xC$ film, than the 3 µm thick film at all applied load values. The 1.5 µm film (-175 V) shows an anomalous behaviour in comparison to the other two films, which could probably be due to cracking and de-lamination effects in the film.

SEM micrographs of wear tracks of $^{nat}B_xC$ film surfaces are shown in Figure(s). 5.8(a), (b), and (c). Wear maps provide a graphical technique to understand wear behaviour of a material in response to the operational parameters of the tribometer such as load, sliding speed etc.. They are extremely useful for understanding different wear mechanisms and help in identifying the acceptable operating conditions. Figure 5.8(a) represents the wear map for -75 V film, with no obvious wear tracks as mentioned earlier in this section. Instead, some wear debris can be seen which could have been transferred to film surface from the worn counter-face material during sliding tests. The chrome steel counter-face material has much lower value of hardness than $^{nat}B_xC$ thin films coatings and therefore faces abrasive wear when rubbed against the film. Asperities present on film surface aggravate the wear process. Formation of self-lubricating surface oxide layer might also contribute to the enhancement of lubricity of the -75 V film [143, 151]. Similar observation was recorded during the wear testing of the -125 V $^{nat}B_xC$ film with 10 N normal load.

Figure 5.8(b) revealed that wear mechanisms for compositionally different $^{nat}B_xC$ samples prepared at different self-bias values are quite different. For -125 V sample, as applied normal load increases from 5 to 15 N, wear scars due to de-lamination and cracking of $^{nat}B_xC$ thin film are intensified. Also, wear scars due to abrasion becomes more prominent as a result of repetitive rubbing of wear debris between coating and the counter face material. For -175 V film as applied normal load changes from 5 to 15 N, micro-scale wear mechanism changes from ploughing and wedge formation to de-lamination wear with some mild polishing (Figure 5.8(b)). This reduced ploughing can account for reduction of friction co-efficient and wear rate as seen in Figure(s). 5.4(c), 5.5(b), and 5.6(b). Figure 5.8(c) represents wear maps of -175 V films having different film thicknesses. Although the thickness of 0.5 μm film might not be sufficient to support externally applied load, the film protects substrate surface from undergoing ploughing wear. With increase in applied normal load from 5 to 15 N, cracking and de-lamination wear becomes more prominent, however, significant material removal is not observed. For film of 1.5 μm thickness, ploughing and wedge formation can be noticed at the lowest applied load, *i.e.* 5 N. As the applied load increases to 10 N, cracking and de-lamination of the $^{nat}B_xC$ coatings can be observed coupled with abrasion due to wear debris. As the load is increased further to 15 N, along with the previously mentioned wear mechanisms, mild polishing is observed. Abrasion of a tribo-coating can cause severe wear to the substrate material where the film is de-laminated from the substrate surface. The same phenomenon has been observed for -175 V, 1.5 μm film, where specific wear rate is found to increase with increasing load. For -175 V film of 3 μm thickness, dominant wear mechanisms are ploughing and wedge formation at 5 N applied load value, similar to 1.5 μm thick film. The wear mechanism changes to abrasion along with mild polishing for 3 μm film at 10 N load, which reduces the specific wear rate as seen in Figure 5.6(a). Further increase of applied load to 15 N results in slight de-lamination of the film, but the polishing on the surface also increases, which again decreases specific wear rate.

5.5 Summary:

This study describes our investigations of microstructure, chemical composition, surface morphology, and tribological properties of ^{nat}boron carbide ($^{nat}B_xC$) thin films on stainless steel, deposited via RF-PECVD technique. Studies involving tribological properties as a function of composition and thickness revealed that both substrate self-bias and film thickness have prominent effect on the composition, microstructure, and ambient stability of the films which in turn affect their tribological properties. Lower self-bias (-75 V) seems advantageous for synthesis of $^{nat}B_xC$ films having superior hardness ~ 2800 HK on account of higher boron content. Lower self-bias is also advantageous for superior wear performance as the -75 V film was devoid of wear marks in tribo-tests. Higher film thickness is preferable to improve friction properties as COF is found to decrease with thickness (~ 0.23 for 3 µm film), for a given film composition at all applied external load values. Higher thickness can also be accounted for reduced wear volume as seen in Figure 5.6(a). Availability of more dry lubricant due to increased film thickness leads to improvement in friction and wear performance of the films. In addition, probable formation of self-lubricating layer on the $^{nat}B_xC$ film surfaces enhances friction behaviour of the films. This study demonstrates feasibility of optimization of tribological properties of $^{nat}B_xC$ film on the basis of composition and thickness by RF-PECVD technique.

Chapter 6 : ^{nat}Boron carbide thin films deposited by RF-PECVD and PLD technique: comparison of structure, optical properties, and residual stress.

6.1 Introduction

Boron carbide is an important non-metallic material, much investigated for various scientific and technological applications [140, 143, 152, 153]. As per requirement, it is used in different forms including powder, sintered bulk material, nano- particles, composites, and thin films. Specific deposition and synthesis techniques are employed for preparation of different boron carbide allotropes [2, 154]. These techniques mainly belong to two categories: chemical vapour deposition (CVD) and physical vapour deposition (PVD). Microstructure and associated thin film properties deposited either by CVD or PVD depends on many factors; predominantly on the energy of incoming adatoms and their surface mobility. Film growth mechanism is also affected by additional processes like re-sputtering, shadowing, reflected neutrals, and ion implantation. In CVD, thin film deposition is governed by non-equilibrium chemical reactions of the decomposed precursor species, therefore, deposited thin films have a significantly different composition, microstructure, and other derivative properties from the source materials [34].

As mentioned in chapter 1, for thin film deposition, one has the opportunity to choose from several existing PVD and CVD processes depending upon the material being deposited. PECVD is a widely accepted technique for thin film deposition. Its advantage over other CVD and PVD techniques emanates from the prominent role played by plasma. The high internal energy state of the plasma medium assists in the efficient fragmentation of vapour phase precursor. It also provides necessary activation energy to initiate the preferred chemical reaction on the substrate surface to form the thin film, prompting efficient depositions at a low process temperature. PECVD technique also enables the deposition of conformal thin films over substrates of complex geometry, at high deposition rate, with precise thickness control, better adhesion, and reproducibility [155, 156]. However, PECVD technique, like any other deposition technique suffers some limitation. The disadvantage of PECVD process is that films deposited by PECVD technique often contain unwanted precursor fragments that affect the stoichiometric purity of the deposited films. To get a perspective about the variation in properties one can observe if we want to choose between a PVD and a CVD technique for deposition of boron carbide thin films, this particular study was performed.

The reason behind choosing the PLD as our PVD technique is that it provides relatively better stoichiometric purity. PLD is quite popular for deposition of thin films of a variety of materials including boron carbide [22, 79]. In PLD, a pulsed laser beam with optimized fluence is incident on a target and induces heating of the target. Subsequently, surface temperature of the target increases, and evaporation of atoms, molecules, and ions takes place from the interaction volume. The dense plume from the target expands in vacuum and gets deposited on a substrate that is usually held perpendicular to the plume. PLD process is advantageous as it is reproducible, can be precisely controlled, and this technique works for almost all materials.

In the past, few researchers have evaluated and compared chemical, structural, mechanical, optical, electrical, and electronic properties of various thin films deposited by PECVD and other PVD techniques [157-159]. For example, Joseph et al. [158] studied the composition, structure, and properties of amorphous Si films deposited with e-beam evaporation and compared them with PECVD deposited films. While the density of the e-beam deposited film was comparable with the PECVD deposited one, the former possesses higher internal stresses. The surface roughness was found to be an order of magnitude less for e-beam deposited films than the PECVD deposited one. Kim et al. [112] investigated TiN thin films deposited by chemical vapour deposition and atomic layer deposition (ALD) method. In another study by Weiss et al. [160], Metallorganic CVD (MOCVD) and PVD deposited copper seed layers were compared concerning step coverage, electrical resistivity, texture, and adhesion behaviour. MOCVD process provided better conformal coatings in comparison with the PVD process. The PVD deposited films were crystalline, while the MOCVD deposited ones turned out to be amorphous. Moreover, PVD deposited films had improved surface roughness, and lower electrical resistivity. All these reports prompted us to find data on comparative study including variation of composition, structure and associated derivative properties of ^{nat}boron carbide thin films deposited by different PVD and CVD techniques. Although, there is a significant amount of work reported by various researchers regarding the dependence of boron carbide thin film composition and properties on the deposition condition for both CVD and PVD techniques, there appears to be few reports about the comparative study of the same [75, 135, 161-164].

In present work, efforts have been made to compare various physical, chemical, and structural properties of PECVD and PLD deposited $^{nat}B_xC$ films. Differences in film properties are expected to arise mainly on account of different characteristic deposition methodologies of the two techniques. Film deposition rate, the extent of adhesion, crystal structure, and chemical composition of two such typical samples has been compared. Mechanical properties like hardness, coefficient of friction, and adhesion have been investigated, these being primary requirements for many functional applications. Because of recently gained importance of boron carbide as optical material [103, 104], optical properties, such as refractive index and extinction coefficient of the $^{nat}B_xC$ thin films have been studied by analysing optical reflection spectra. Finally, the total residual stress distribution in the films has been studied with the help of optical interferometry. The utility of each deposition technique for fabrication of boron carbide ($^{nat}B_xC$) films has been discussed based on these film properties.

6.2 Experimental:

6.2.1 Deposition:

$^{nat}B_xC$ thin films were deposited on Si (100) substrates via PECVD technique inside a stainless-steel plasma reactor, using a capacitively coupled fixed frequency (13.56 MHz RF) power source, described in details in earlier chapters. Prior to loading in the process chamber, Si (100) substrates were cleaned for removal of organic, ionic, and oxide contaminants. Sputter cleaning of the samples was done in Ar environment for 20 minutes at a chamber pressure of 0.190 mbar at $-200\,V$ self-bias, before commencement of each deposition run. Deposition was carried out at a chamber pressure 0.300 mbar at $-100\,V$ self-bias value for 10 minutes at a substrate temperature $400\ ^\circ C$.

Another set of ^{nat}boron carbide ($^{nat}B_4C$) thin film was prepared by PLD technique in a stainless-steel deposition chamber under a vacuum of 10^{-5} mbar. Details of the deposition conditions have been described in section 2.1.2, Chapter 2, earlier. Films were deposited for different substrate temperatures; room temperature, 200 °C, and 400 °C. Films deposited at room temperature and 200 °C were found to be soft and had poor adhesion making them unsuitable for subsequent applications and characterization.

For comparison studies, PECVD deposited $^{nat}B_xC$ film synthesized at -100 V self-bias (400 °C substrate temperature) and PLD deposited B_4C film deposited at 400 °C substrate temperature were chosen. For ease of discussion, PLD deposited boron carbide film will henceforth be identified as PLD 400C and the one deposited by PECVD technique will be identified as PECVD -100V, respectively.

6.2.2 Characterization:

The local chemical environment of constituent elements of ^{nat}boron carbide thin films was investigated via ex-situ X-ray photoelectron spectroscopy (XPS). Measurements were performed using a VG make model CLAM-2 hemispherical analyser with Mg K_α source (1253.6 eV) with a step size of 0.1 eV. Detailed scans were taken with pass energy 50 eV to acquire the electron spectra of individual elements. The microstructure of the films was studied using X-ray diffraction (XRD) and Grazing angle X-ray diffraction (GIXRD) technique. GIXRD data was recorded at an angle of incidence 0.6 deg. To compare optical constants of the films, optical reflection spectra were recorded using a spectrophotometer (UV-3101PC, SHIMADZU) in the spectral range of 200 nm- 1200 nm. Film thicknesses were also estimated via analysis of these absorption spectra. Optical interferometry was employed for precise measurement of the radius of curvatures [165] of samples. Residual stress in the films has been evaluated using Stoney formula from the differential substrate curvature of the samples measured via a laser Fizeau interferometer before and after thin film deposition.

Surface hardness was measured by a microhardness tester (Future Tech FM-7 model) using Knoop indenter with 0.25 N normal load. Dwell time for each of the measurements was 10 seconds. Multiple readings were performed for each sample at five different locations and the average values of the hardness have been reported here. Scratch-adhesion test was performed on the film surfaces using a CSM Revetester scratch adhesion tester. The scratch indenter used was a 200 µm tip radius Rockwell type diamond indenter. Tests were performed in single pass; Progressive Load Scratch Test (PLST) mode in which applied normal load was linearly increased with time. The starting contact load was 1 N and the end value of the load was 30 N for all the samples. The scratch length was 3 mm and the slide velocity of the applied normal load was kept at 2 mm/ min.

6.3 Results:

6.3.1 Thickness, deposition rate, and hardness:

Thickness of the films was calculated from the optical reflection spectra, details of the analysis method are given in section 6.3.5. The results show that PLD 400C film was much thinner than PECVD -100 V film despite longer deposition time owing to a lower deposition rate (Table 6.1). Deposition rates for PECVD -100V and PLD 400C films were found to be 124.2 nm/ min and 5.3 nm/ min, respectively. Hardness of the PECVD -100V and PLD 400C films were found to be 2798 HK and 1467 HK, respectively (Table 6.1).

Table 6.1: Physical properties of PECVD and PLD deposited ^{nat}boron carbide thin films.

Samples	**Thickness (nm)**	**Deposition rate (nm/min)**	**Knoop Hardness (HK)**	**Coefficient of Friction**	**Refractive index at λ = 600 nm**	**Residual Stress (MPa)**	**Critical load (in N)**		
							L_{C1}	**L_{C2}**	**L_{C3}**
PECVD-100V	1242	124.2	2798 ± 8%	0.03 ± 3%	1.82	25	20.3 ±0.5	25.8 ±0.5	29.5 ±1
PLD 400C	318	5.3	1467 ± 5%	0.04 ± 4%	1.80	-1001	7.6 ±0.5	20.0 ±1	28.1 ±2

Where **L_{C1}** = critical load at which the brittle failure initiates.

L_{C2} = critical load at which significant cracks are generated.

L_{C3} = critical load where partial removal of thin film from the substrate was observed.

6.3.2 Scratch-adhesion test:

Optical micrographs of the scratch tracks of PECVD -100V and PLD 400C films recorded during the scratch-adhesion test in PLST modes are shown in Figures 6.1(a), and (b), respectively. Scratch tracks were recorded via an optical microscope immediately after the indentation to identify various coating failure mechanisms at different applied normal load values. For PECVD -100V film, Figure 6.1(a) shows that the indenter scratches start to appear on the film surface at around 12 N loads, subsequently becoming more prominent around 20.3 N. Well defined coating failure occurs when the coating is stripped off exposing the substrate underneath and the value of the applied normal load at which this happens is called critical load (L_c) for coating failure [79]. For PECVD -100V sample, the critical load (L_c) is 25.8 N. Interfacial detachments occur near 29 N normal load value. Figure 6.1(b) shows that for PLD 400C film, a series of nested micro-cracks start appearing within the scratch groove at the load of 7.6 N which become prominent around 10.4 N. Film de-lamination occurs near 25.1 N. Friction coefficients for the films was also derived from the scratch test as a ratio of the tangential force and normal force. The software readily gives the variation of the friction coefficient as a function of applied normal load and the average value of friction coefficient. For PECVD -100V film, friction coefficient was 0.03 (± 3%) in the coating zone up to 25.8 N load, after which it increased to 0.05 (± 10%) in the failure zone. For PLD 400C film, friction coefficient was 0.04 (± 4%) in the coating zone up to 20 N load, after which it increased to 0.05 (± 5%) in the failure zone.

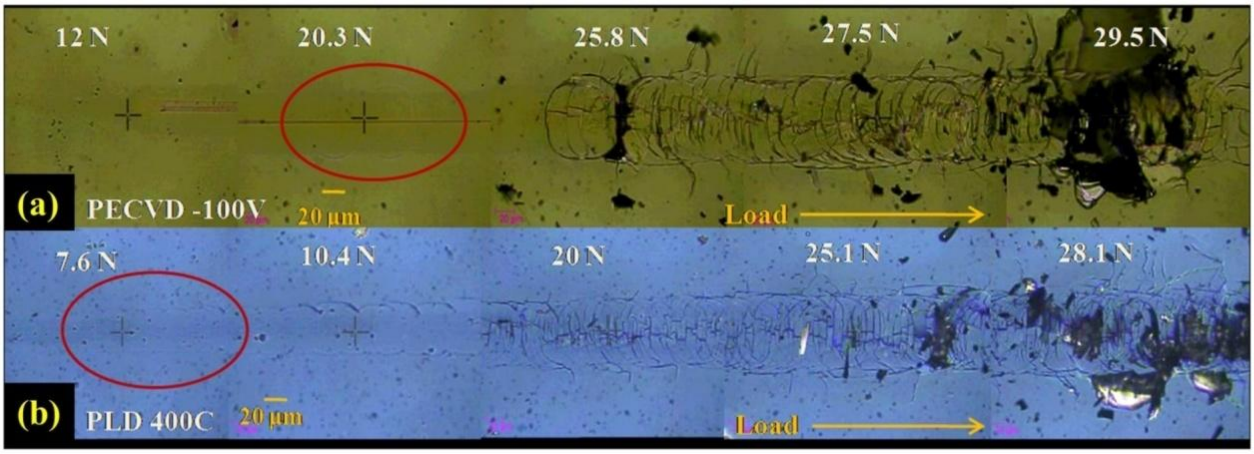

Figure 6.1: Optical micrographs of scratch tracks and critical loads (L_c) for coating failure for (a) PECVD -100V and (b) PLD 400C ^{nat}boron carbide thin films.

6.3.3 Microstructure:

XRD and GIXRD scans of ^{nat}boron carbide samples and the $^{nat}B_4C$ target used during PLD are shown in Figures 6.2(a), and (b), respectively.

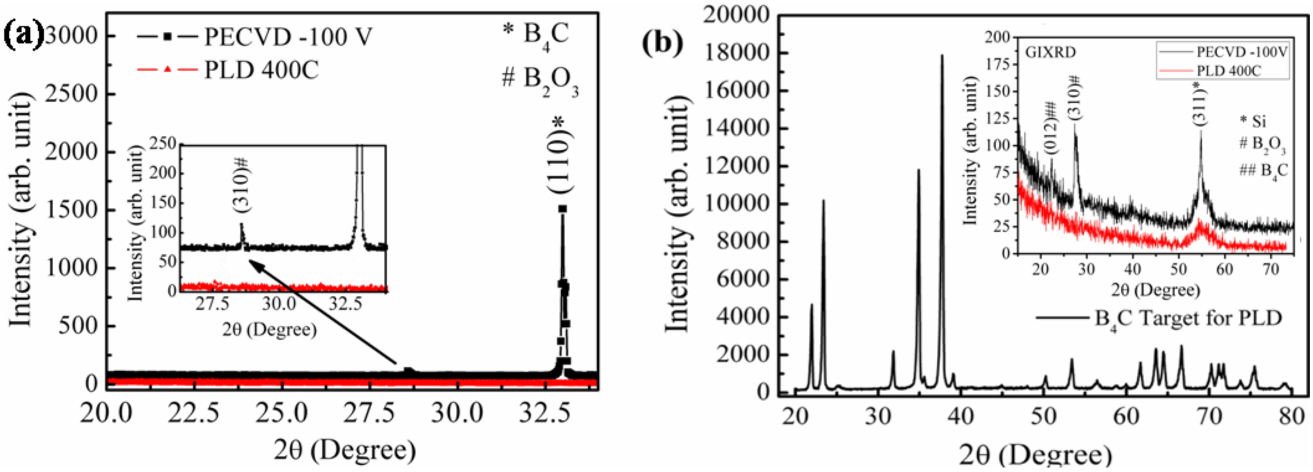

Figure 6.2: (a) XRD diffractogram of ^{nat}boron carbide thin films. The inset plot shows enlarged XRD diffractogram for 2θ ranging from 27°- 33°, (b) XRD diffractogram of $^{nat}B_4C$ target used for PLD. The inset plot shows GIXRD patterns of ^{nat}boron carbide thin films.

In XRD scans (Figure 6.2(a)), although characteristic peaks of boron carbide and boron oxide phases were seen for PECVD deposited sample, the same was not observed for PLD deposited films. For PECVD -100V film, boron carbide phases were identified by search-match comparison with JCPDS ICDD database. Experimentally found peak positions had the closest match with the peak positions listed in the JCPDS file nos. #75-0424 and #06-0297. Peaks located at 28° (Figure 6.2(a)) represents the orthorhombic B_2O_3 phase and the one located at 33° corresponds to the rhombohedral B_4C phase which is consistent with our previous findings [138]. Since in XRD scans for PLD deposited film, the signature boron carbide peaks were not seen, GIRXD patterns for the sample were recorded to get information about the microstructure of these deposited thin film. As seen in the inset of Figure 6.2(b), for PLD deposited film, absence of characteristic boron carbide peak and oxide peak suggested amorphous nature of the film as seen in the GIXRD patterns. For PECVD -100V film, prominent boron oxide (B_2O_3) peak at 28° in GIXRD in addition to characteristic B_4C peak at 22.9° was once again observed as in case of XRD.

6.3.4 X-ray photoelectron spectroscopy (XPS):

The local chemical bonding environment of two main constituent elements of ^{nat}boron carbide thin films, boron (B), and carbon (C) was investigated using XPS technique. B 1*s* and C 1*s* spectra are shown in Figure(s) 6.3(a) and (b) respectively. Precaution was taken during data analysis to fit the minimum number of relevant peaks and χ^2 value was kept near 1. In B 1*s* spectra for PECVD -100V film, most dominant peak is situated at 187.5 eV corresponding to super stoichiometric B_xC $(x > 4)$ phase [78, 86]. Signature of stoichiometric boron carbide phase (B_4C) is also present in the XPS spectra at 188.5 eV along with sub-stoichiometric $BC_{3.4}$ phase situated around 189.8 eV [86]. The peaks present in higher binding energy side of B 1*s* spectra belong to the oxy-boron carbide and boron oxide phases BCO_2 and B_2O_3, at 191.5 eV and 192.3 eV respectively [87].

In contrast, stoichiometric B_4C phase is the most dominant phase in the PLD 400C film. Peaks corresponding to stoichiometric B_4C and super stoichiometric B_xC $(x > 4)$ phases appear at the same positions as PECVD -100V film, *i.e.* at 188.5 eV and 187.5 eV respectively. Also, presence of sub-stoichiometric $BC_{3.4}$ phase can be seen around 189.8 eV. Although, B_2O_3 oxide phase observed in PECVD -100V film cannot be seen in the PLD 400C film, peak belonging to oxy- boron carbide phases BCO_2 appear at 191.5 eV [88].

C 1*s* spectra of PECVD -100V film (Figure 6.3(b)) has the most dominant peak situated at 285 eV referring to the adventitious carbon on the surface. Oxy-boron carbide phases appear near 283.8 eV. Peak representing B-C bond appears at 282.9 eV. Adventitious carbon continues to be the most dominant peak in case of PLD 400C film also. Similarly, the peaks corresponding to oxy-boron carbide phases and B-C bond appear at the same position as PECVD -100V film. Peaks appearing towards the higher binding energy side represent bonding of carbon atoms with oxygen. Peaks at 286.2 eV and 288.2 eV correspond to C-O and C=O bonds respectively [88, 92]. In both the B 1*s* and C 1*s* spectra for all samples, presence of prominent oxide peaks is a clear indication of significant amount of oxygen incorporation in the surface layer.

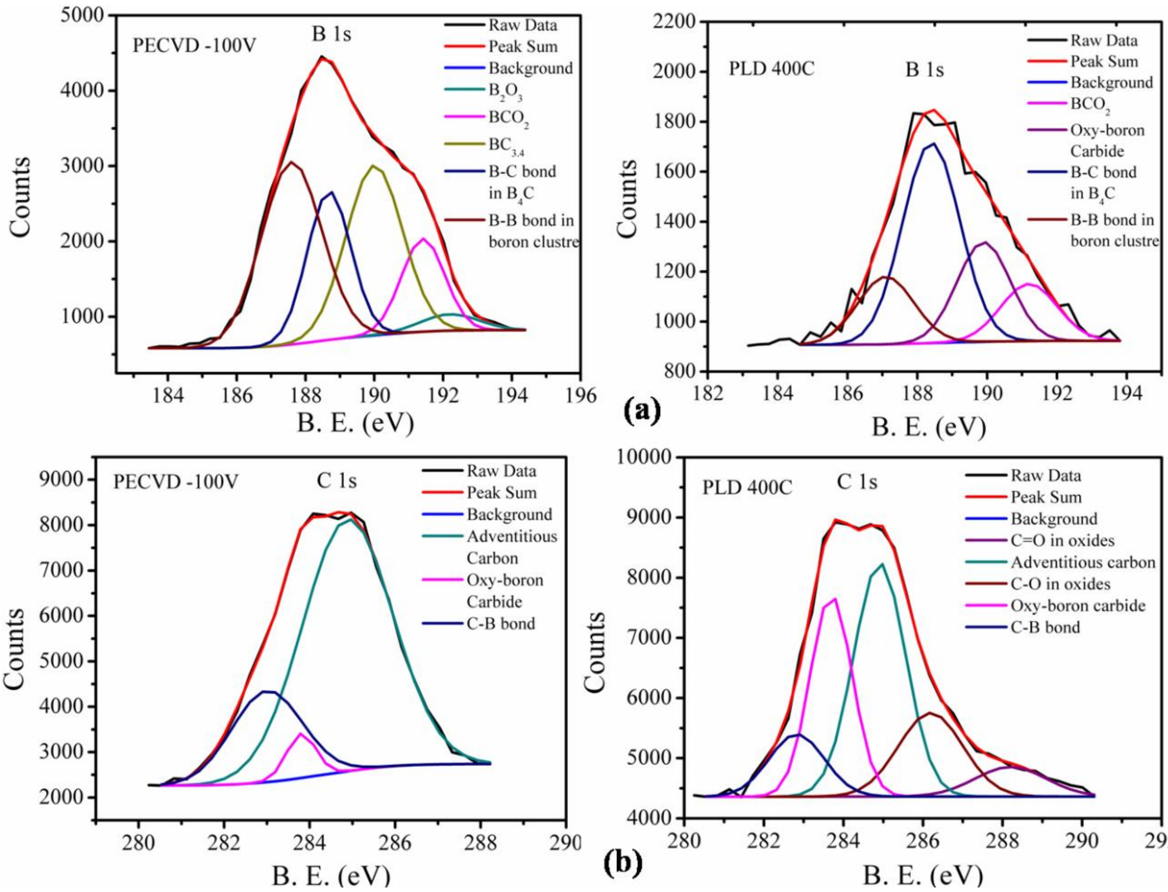

Figure 6.3: Core level XPS spectra of (a) B 1s and (b) C 1s lines of the PECVD and PLD deposited natboron carbide films.

6.3.5 Optical properties:

Optical properties: refractive index(n), extinction coefficient(k), and also thickness (d) of ^{nat}boron carbide thin films deposited by PECVD and PLD technique have been determined from their measured normal reflection spectrum using Inverse synthesis method. In this method, the measured spectrum is fitted with a theoretically generated spectrum using suitable dispersion models. For theoretical modeling, the thin film is assumed to be isotropic and optically homogeneous. Films are deposited on a substrate and during reflection measurement, the film-substrate system is surrounded by air having refractive index $n_0 = 1$. Light is incident normal to the thin film-substrate system. Thin film of thickness d has complex refractive index $N = n + i\,k$, where n and k are the refractive index and extinction coefficient of the film. The substrate has complex refractive index $N_s = n_s + i\,k_s$. Substrate thickness (d_s) satisfies the condition $d_s \gg d$. Since the optical path difference inside the film is less than the coherence length of the incident light, multiple reflections occur inside the film that generates interference fringes. The back-surface reflection of the substrate is neglected because of its absorbing nature. Reflection of the thin film-substrate optical system as a function of wavelength of light λ at normal incidence is given by the following expressions [166-168]:

$$R = \frac{R_1+R_2+2(R_1R_2)^{1/2}\cos(x-\delta_1+\delta_2)}{1+R_1R_2+2(R_1R_2)^{1/2}\cos(x+\delta_1+\delta_2)} \ldots\ldots\ldots\ldots(6.1)$$

where,

$$R_1 = \frac{(n-1)^2+k^2}{(n+1)^2+k^2} \ldots\ldots\ldots\ldots\ldots\ldots\ldots\ldots\ldots\ldots(6.2)$$

$$R_2 = \exp(-2a)\,\frac{(n_s-n)^2+(k_s-k)^2}{(n_s+n)^2+(k_s+k)^2} \ldots\ldots\ldots\ldots\ldots(6.3)$$

$$x = \frac{4\pi n d}{\lambda} \ldots\ldots\ldots\ldots\ldots\ldots\ldots\ldots\ldots\ldots\ldots\ldots(6.4)$$

$$a = \frac{4\pi k d}{\lambda} \ldots\ldots\ldots\ldots\ldots\ldots\ldots\ldots\ldots\ldots\ldots\ldots(6.5)$$

$$\tan\delta_1 = \frac{2k}{1-n^2-k^2} \ldots\ldots\ldots\ldots\ldots\ldots\ldots\ldots\ldots\ldots(6.6)$$

$$\tan\delta_2 = \frac{2nk_s-2n_sk}{(n^2-n_s{}^2)+(k^2-k_s{}^2)} \ldots\ldots\ldots\ldots\ldots\ldots\ldots(6.7)$$

Here, x and a are the real and imaginary part of the phase factor. δ_1 and δ_2 are the phase shifts at the air-film, and film-substrate interfaces, respectively. The measured reflection spectrum is a set of experimental data (λ_j, R_j^{Exp}), j =1, 2, 3,...., N. The optical constants n, k and thickness d have to be determined from this experimental data. This implies that for all j = 1, 2, 3,......, N, the calculated reflection $R_j^{\,Cal}$ must satisfy the equation: $R_j^{\,Cal}[\lambda_j, n_s(\lambda_j), n(\lambda_j), k(\lambda_j), d] = R_j^{Exp}$ for all wavelengths λ_j. The three unknowns $n(\lambda)$, $k(\lambda)$, and d are obtained through an iterative optimization procedure. The functional forms of $n(\lambda)$ and $k(\lambda)$ are assumed using single oscillator and Urbach model [107, 169], respectively as follows.

$$n(\lambda) = \sqrt{1 + \left(\frac{E_0 E_d}{E_0^2 - (hc/\lambda)^2}\right)} \text{......................}(6.8)$$

$$k(\lambda) = \alpha\, exp\left(1240\beta \left(\frac{1}{\lambda} - \frac{1}{\gamma}\right)\right) \text{..............}(6.9)$$

Where, λ is the wavelength of light, E_0 is the single oscillator energy, and E_d is the dispersion energy. The constants *α, β,* and *γ* are the fitting parameters of the extinction coefficient. The fitting is then carried out by minimizing the squared difference (χ^2) between the experimentally measured and calculated values of reflection given by:

$$\chi^2 = \frac{1}{(2N-P)} \sum_{j=1}^{N} \left[\left(R_j^{Exp} - R_j^{Cal}\right)^2\right] \text{...........}(6.10)$$

Where, R_j^{Exp} and R_j^{Cal} are the experimental and calculated reflectances, respectively. *N* and *P* are the number of data points and the number of model parameters. The optimization is done using the Levenberg-Marquardt algorithm. After a fine adjustment of the parameters, a good fitting can be achieved. The fitting parameters are used to determine the thickness(d), refractive index (n), and extinction coefficients (k) of the films. Figure 6.4 shows the measured reflection spectra along with the best-fit theoretically generated spectra of the ^{nat}boron carbide thin films prepared by PECVD and PLD method. The calculated thicknesses of the PECVD -100V and PLD 400C films are 1242 nm and 318 nm, respectively. The refractive index and extinction coefficient spectra obtained from the fitting parameters are plotted in Figure 6.5(a), and (b). For a typical wavelength of 600nm, refractive index values for PLD 400C film was 1.80 whereas a value of 1.82 was obtained for the PECVD -100V film. From the extinction coefficient spectra shown in Figure 6.5(b), at a typical wavelength 600 nm, the value of the extinction coefficient of PLD deposited film was found to be higher than that of PECVD deposited film.

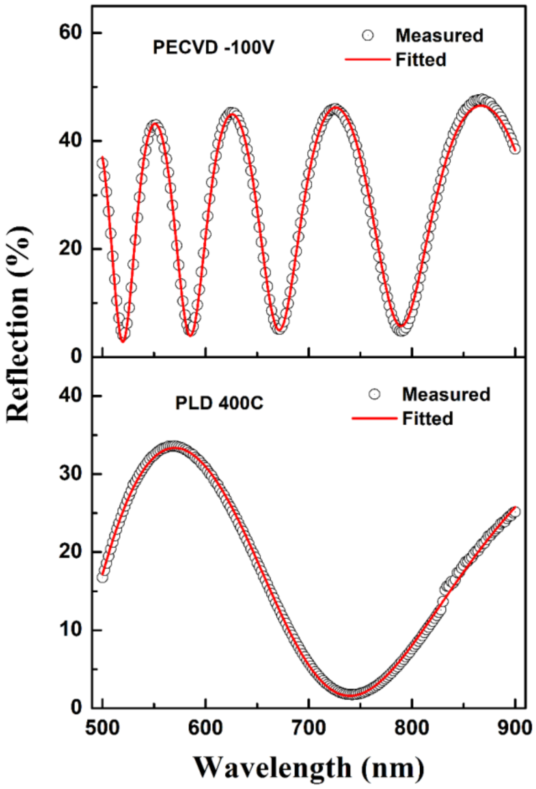

Figure 6.5: Measured optical reflection spectra of natboron carbide thin films with best fit theoretical simulation.

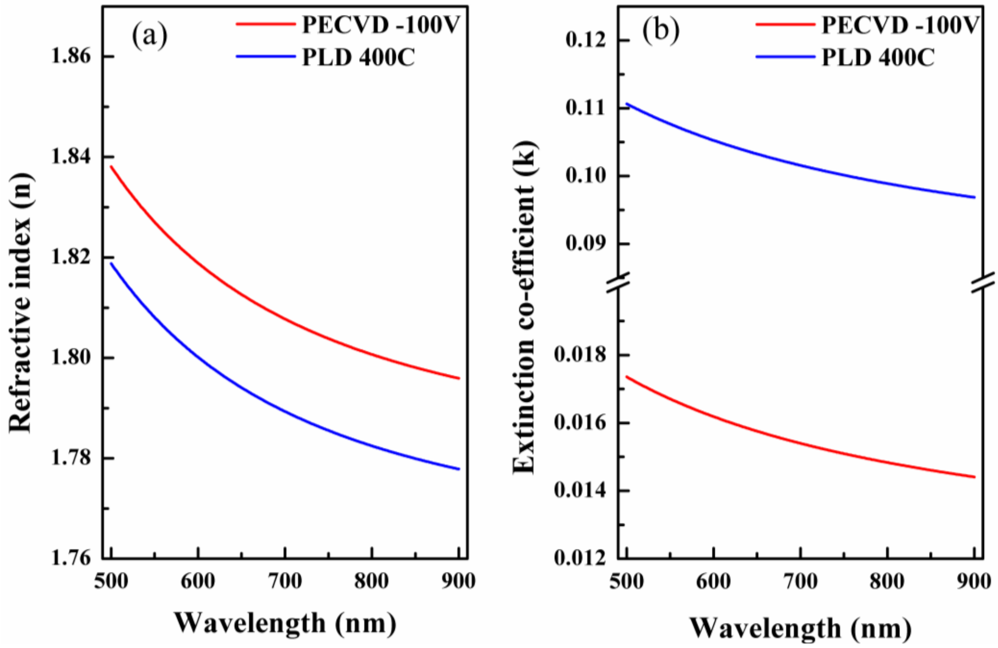

Figure 6.4: (a) Refractive index and (b) Extinction coefficient spectra of the natboron carbide thin films.

6.3.6 Residual stress:

There are numerous experimental techniques for determining residual stress in a thin film. Of these, the substrate curvature method is preferred on account of precision and simplicity of measurement. Moreover, this technique does not require information about the mechanical parameters of the thin films such as bi-axial elastic modulus, Poison's ratio etc., which are sometimes unknown. Only the curvature of the substrate before and after thin film deposition is used for determination of the residual stress in the films. The 2D substrate surface profiles before and after deposition of ^{nat}boron carbide thin films are shown in Figure 6.6.

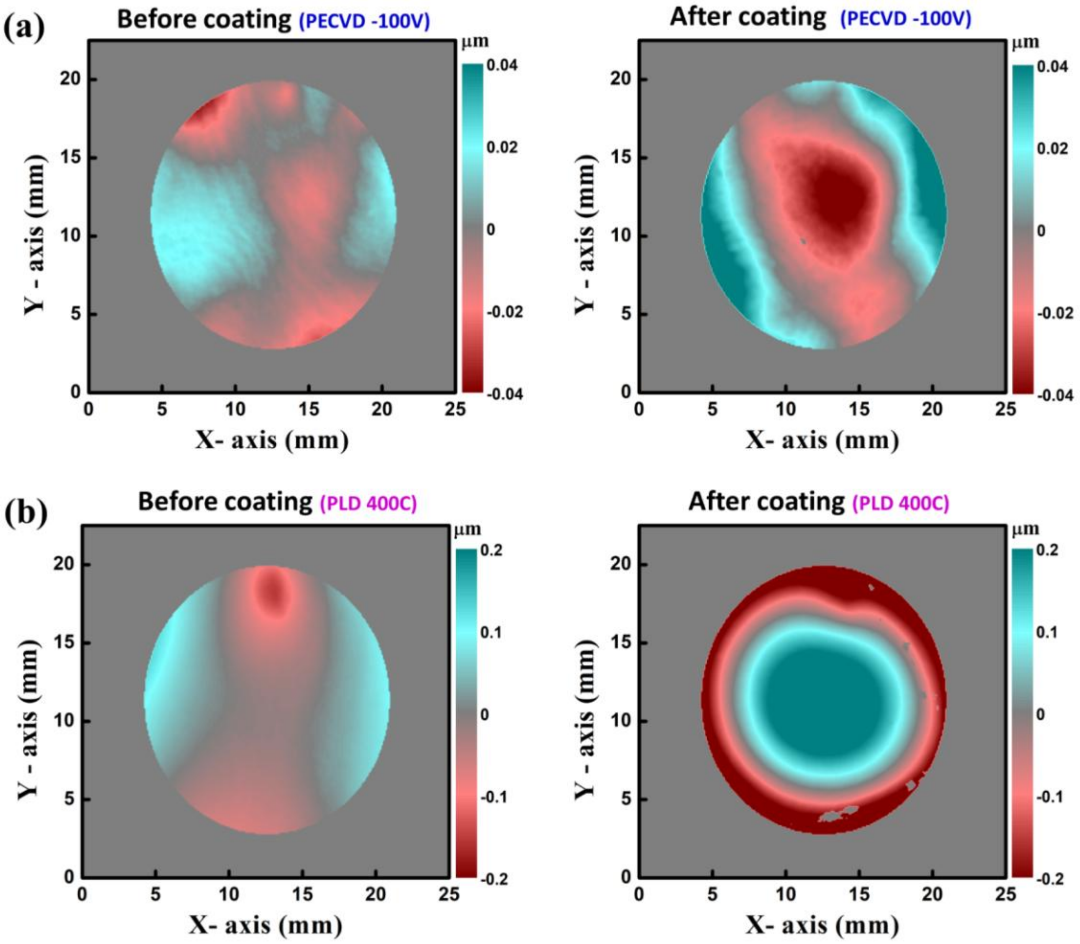

Figure 6.6: 2D surface contour map of substrates before and after deposition of PECVD -100V and PLD 400C ^{nat}boron carbide thin films.

The surface profiles were obtained by analyzing interference patterns formed between the sample and an optical flat in a laser Fizeau interferometer, described in detail elsewhere [170]. The spherical shape component was extracted from the surface profile data using Zernike polynomial. Various coefficients of this polynomial are a measure of contributing surface errors. One of the coefficients, known as defocus term that represents the length of Sagitta (s) of the spherical shape component, which is used for the calculation of the radius of curvature of the surface using the following equation [171]:

$$R = \frac{r^2}{2s} + \frac{s}{2} \ldots\ldots\ldots\ldots\ldots\ldots\ldots\ldots\ldots\ldots\ldots\ldots\ldots\ldots\ldots (6.11)$$

Where, r(~ 8.75 mm) is the radius of circular-shaped surface under consideration, and s is the sag in the curvature profile. Subsequently, residual stress in the films has been derived from the measured curvatures using the Stoney's equation [169, 172]:

$$\sigma = \frac{1}{6}\left(\frac{E_s}{1-\upsilon_s}\right)\left(\frac{1}{R_a} - \frac{1}{R_b}\right)\left(\frac{d_s^2}{d}\right) \ldots\ldots\ldots\ldots\ldots\ldots (6.12),$$

where, R_a and R_b is the radius of curvature of the substrate before and after deposition, respectively, E_s is the young's modulus, υ_s is the Poisson's ratio of the substrate, d_s and d are the thicknesses of the substrate and the film, respectively where $d \ll d_s$. Equation (6.12) is valid for isotropic and homogeneous stress distribution in the film, when deformations due to internal stress are very small compared to the film thickness. Following convention, tensile stress has been considered positive and compressive stress has been considered negative. The parameters of Si (100) substrates used in Equation (6.12) are $E_s = 130$ GPa, $\upsilon_s = 0.26$, and $d_s = 0.5$ mm. The thicknesses of the $^{nat}B_xC$ films as calculated from the reflection spectra were used in Equation (6.12). As mentioned earlier, estimated thicknesses (d) of PECVD -100V and PLD 400C films are 1242 nm and 318 nm, respectively. Utilizing Equations (6.11) and (6.12), residual stresses in the films were calculated and it was found that residual stress is tensile in nature for PECVD -100V and has a magnitude 25 MPa. Stress for PLD 400C

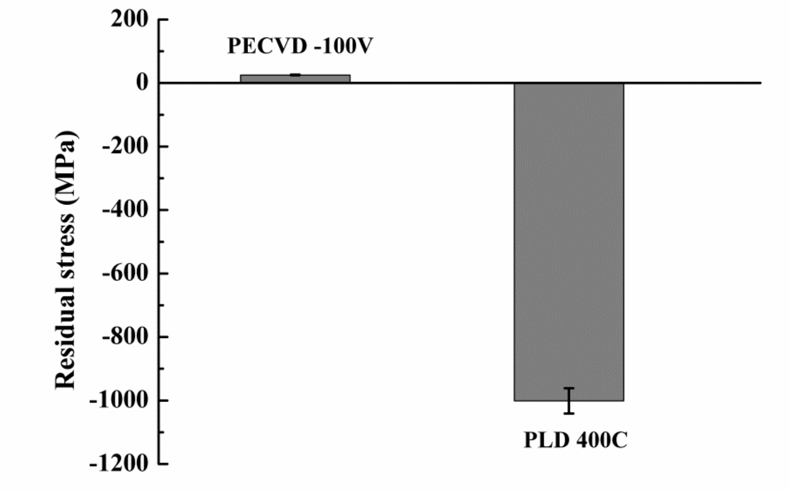

Figure 6.7: Residual stresses of PECVD and PLD deposited ^{nat}boron carbide thin films.

film is compressive in nature and has a magnitude -1001 MPa. A plot of the estimated residual stresses for the ^{nat}boron carbide samples is shown in Figure 6.7.

4. Discussion

Deposition mechanisms:

Both PECVD and PLD techniques are favoured for thin film deposition and depending upon the nature of application, there are strong reasons to use either process successfully. Deposition mechanisms are essentially different in PECVD and PLD techniques, which results in the deposition of thin films having different physical and chemical properties. During PECVD, substrate surfaces in contact with plasma are subjected to a bombardment of different particles such as: slow and fast neutrals, electrons, ions, radicals, complex molecules, and photons. Each of these species plays useful role depending on the application of interest. For PECVD of thin films, the role of radicals, energetic ions, electrons, and fast neutrals becomes extremely important. When the precursor molecules enter the plasma environment, energetic electrons ensures the efficient fragmentation of precursors. The degree of precursor fragmentation can be controlled by changing plasma conditions such as: plasma power, precursor feed rate, and partial pressure of the plasma reactor. Once the precursor is fragmented, the radicals, ions, and partially fragmented precursor molecules travel towards substrate surface, and participate in deposition of thin films by chemical reaction. Moreover, the configuration of the deposition chamber used for PECVD in our study allows the ionic species to bombard the surface of the growing film. Energetic ion bombardment can significantly influence the processes of adsorption of molecules onto substrate surface and their subsequent reactions. Molecular ions from the precursor can fragment further upon impinging on the substrate surface and their fragments can further participate in various surface processes. Thus, ion irradiation during thin film deposition affects the microstructure, microchemistry, and hence derivative physical properties of as-deposited layers [34].

On the other hand, in PLD, a high-power laser beam is focused on a small area of the target surface. This laser energy, when absorbed, is utilized to ablate a small fraction of material from the solid target. During the ablation process, molecules of the target material are evaporated or ejected in a particular direction depending upon the deposition geometry. The evaporated target material usually consists of ions, molecules, neutrals, and free radicals in their ground and excited states. Often, these particles further absorb energy from the incident high energy laser beam and produce a plasma plume directed towards the substrate. The generated vapour plume expands away from the target, different constituent particles of the plume have different velocity distribution in the forward direction. In our study, the typical deposition geometry was such that the substrate was usually kept at ~ 4.5 cm distance, parallel to the target. Ultimately, the ablated species condense on the substrate surface, forming a thin film. Usually stoichiometry of the target material is preserved in this laser based material ablation process. Simultaneous evaporation of all the constituent elements of the target, irrespective of their binding energies ensures this preservation of stoichiometry. Accumulation of ablated target material on the substrate from a sequence of laser pulses leads to the gradual formation of thin film. During PLD, laser parameters such as fluence, wavelength, pulse duration, pulse repetition rate can be controlled. Also, deposition conditions and system configurations such as target to substrate distance, substrate temperature, background gas, deposition time, and chamber pressure can be varied. All of these aforementioned parameters and configurations can affect the film growth kinetics, structure, crystallinity, and associated film properties [34, 173].

Selection of samples for comparison

In this study, both the aforementioned processes were utilized for the deposition of $^{nat}B_xC$ thin films on Si (100) substrates. The substrate temperature was kept at 400 °C in both the cases as substrate temperature is known to affect the film structure and properties significantly. Several characterization techniques have been employed to investigate deposition rate, roughness, friction coefficient, adhesion, chemical environment of the constituent elements, film crystallinity, optical constants, and residual stress. During PECVD, ^{nat}boron carbide films were deposited at -100 V DC self-bias at the powered electrode. This DC self-bias plays a significant role in determining film composition as both the ion bombardment energy and ion flux can be regulated by DC self-bias. For PLD deposition of boron carbide films, commercially available 99.9% pure sintered B_4C pellets were used as target materials. During PLD, ^{nat}boron carbide films deposited at substrate temperatures lower than 400 °C turned out to be quite soft which delaminated from the substrate easily. At elevated substrate temperatures, the adatoms from the atomic clusters on the substrate surface coming from the target have a higher mobility due to their higher kinetic energy which can affect the arrangement of atoms [174] during nucleation and growth of the films. Also, heating of the substrate before or during deposition can help in removing traces of moisture on the surface which in turn leads to better adhesion of the thin film with the substrate. During deposition, in presence of moisture, boron atoms in boron carbide have been reported to react with the oxygen and form boric acid, leading to softer films [125, 150] in case of PLD. This might be the reason for the ^{nat}boron carbide films being stable and having comparatively good adhesion with the substrate when deposited at substrate temperatures 400°C and above.

Phase structure of the films

XRD and GIXRD scans of the ^{nat}boron carbide samples (Figures 6.2(a), and (b)) show that for same substrate temperature, PECVD -100V film possesses crystalline phases of boron carbide, whereas PLD deposited film is largely amorphous in nature. XRD patterns of the $^{nat}B_4C$ target was also recorded to extract information regarding the crystalline phase of the target material (Figure 2(b), JCPDS # 35-0798, # 06-0555) that was employed for PLD and it was found to be highly crystalline. The crystalline nature of thin films depends on the arrangement of the atomic cluster/ adatoms on the substrate surface, which in turn is dependent on the ad-atom mobility. Again, surface adatom mobility is mainly influenced by kinetic energy of the incoming atoms and the substrate temperature [175]. The incorporated adatoms having sufficient energy try to reach the equilibrium lattice sites, forming crystalline structure. In addition to unfavourable deposition conditions such as low energetic deposition, hence low surface adatom mobility, very high energetic deposition also result in particle implantation, defect and stress formation, all leading to amorphous films [176]. In our study, both PLD and PECVD are energetic deposition techniques, but the mechanisms for thin film deposition are different.

In this study, for pulsed laser deposition of samples, the laser fluence was kept at$15\, J/\, cm^2$. At such laser fluence, the energy of the incoming particles lie in the range of hundreds of electron volts. These energetic species can cause implantation of additional material in the already grown film resulting in high compressive stress and amorphous film structure [176] discussed in detail later in this section. Choice of suitable deposition conditions such as laser fluence and substrate temperature [176-178] could perhaps help in formation of crystalline ^{nat}boron carbide thin films via PLD. On the other hand, thin film deposition mechanism in PECVD is completely different from PLD. Several favorable chemical reactions take place in the in highly-energetic plasma environment, as well as, on the substrate surface, which otherwise would not have taken place due to lack of required activation energy, which aid in formation of crystalline ^{nat}boron carbide thin films. Besides, energetic ion bombardment due to “self-bias” coupled with substrate temperature facilitates the surface ad-atom mobility and supplies enough energy to the adatoms to arrange themselves in crystalline stable boron carbide phases.

Comparison of thin film-substrate adhesion

For any functional thin film, good adhesion between the deposited thin film and substrate is a primary requirement. A comparison of adhesion properties of different thin film samples is only valid if the failure modes are similar in the samples under consideration [179, 180]. In this study, the thin film-substrate system is a “moderately hard substrate- hard coating” (Si (100) - ^{nat}boron carbide thin film) system. The scratch- adhesion test of the samples revealed that both PECVD and PLD deposited thin films suffer brittle failure and the subsequent critical load values (L_c) for various failure mechanisms are listed in Table 6.1. In PECVD -100V sample (Figure 6.1(a)), at the critical load L_{C1} near 20.3 N, formation of the Hertzian ring cracks represent typical through-thickness cracking mode for brittle materials. As the load increased further, several of these Hertzian cracks intersect and give rise to a crack network along the scratch track (L_{c2} = 25.8 N). At the location in the thin film coating where the density of the scratch network is more intense, considerable chipping takes place and the coating is partially delaminated from the substrate (L_{C3} = 29.5 N). Some cracking can also be noted on either side of the scratch track along with the Hertzian rings. PLD 400C film (Figure 6.1(b)) show similar failure modes as PECVD -100V film but the critical load values were different. For this film, partial delamination occurred at 28.1 N. Hence, for similar substrate temperature 400 °C, PECVD deposited $^{nat}B_xC$ film is found to have slightly better adhesion than the PLD deposited film.

Typically thin-film substrate bonding can take place by virtue of the following mechanism: mechanical interlocking, physical bonding, and chemical bonding. A single mechanism usually dominates the adhesion behavior of the thin film. In mechanical interlocking, the film is held on the substrate by virtue of mechanical joints between the film and the substrate. The incoming adatoms fills the pores and defects on the substrate surface, and creates the mechanical bonds. Physical bonding is the most prominent adhesion mechanism between most of the substances. These bonds are almost exclusively, exceptionally weak dispersion bonds. Physical bonds are not strong enough to ensure better adhesion of the films. Chemical bonds on the other hand can form either by inter-diffusion of the film and substrate, or by a chemical reaction between the film and the substrate to form strong bonds in that manner. Chemical bonds are much (2 to 20 times) stronger than physical bonds, and act over a much shorter distance (typically an atom diameter) [181]. In PLD deposited films, the bonding between the ^{nat}boron carbide thin film and Si (100) substrate is mostly diffusion bonding. In PECVD, the bonding between thin film and substrate comprises of diffusion of deposited material into the substrate surface, as well as, interfacial chemical rection [34, 181]. The crystalline structure and strong interfacial bonding which could account for the slightly increased adhesion observed in case of PECVD -100 V film.

Surface composition

XPS technique revealed the local chemical environment of two main constituent elements: boron and carbon in the films. Deconvoluted B 1*s* XPS spectra of PECVD -100V and PLD 400C films show the signature of multiple stoichiometric and non-stoichiometric boron carbide and boron oxide phases on the surface (Figure 6.3(a)). Most dominant stoichiometric phase for PLD 400C film is B_4C, whereas for PECVD -100V film, super-stoichiometric B_xC $(x > 4)$ phase is the most dominant one in the surface accompanied by stoichiometric B_4C and sub-stoichiometric $BC_{3.4}$ phases. PLD technique is known to produce thin films having stoichiometric purity since in this technique the material from the target is ablated and deposited on the substrate without significant change in the composition. Slight compositional changes appearing on the deposited film might be a consequence of deposition conditions. This is the reason for the dominance of stoichiometric boron carbide phase in the PLD 400C film. In PECVD technique, organic or inorganic precursors undergo disintegration and radical polymerization upon exposure to highly energetic plasma environment and then undergo a series of favorable chemical reaction on the substrate surface followed by thin film deposition [182]. For PECVD -100V film the deposition conditions were perhaps favourable for deposition of super-stoichiometric B_xC $(x > 4)$ phase. For both the samples, boron oxide and oxy-carbide peaks appear in the higher binding energy side [78]. Oxide phases arise in both the films due to bonding of boron with oxygen, coming from disintegration of residual gases and moisture in the process chamber during deposition. Oxygen can also get incorporated in the films after deposition, during storage due to exposure in the ambiance. In C 1*s* spectra for both PECVD -100V and PLD 400C samples (Figure 6.3(b)), adventitious carbon is the most dominant peak which might have been incorporated in the substrate surface due to exposure in the ambient environment. The signature peak representing C-B bond is also present in each sample. Signature of oxide and oxy-carbide peaks in C 1*s* spectra indicates that oxygen impurities, apart from bonding with boron, react with carbon as well.

Optical properties

Complex refractive index spectra (Figure 6.5(a)) show that both PECVD -100V and PLD 400C films possess similar refractive indices at typical wavelength 600 nm lying in the wavelength measurement range of 500- 900 nm, having values 1.82 and 1.80, respectively. A slightly higher value of the refractive index for PECVD -100V film could be a result of higher film density as compared to the PLD 400C film. For another PLD deposited ^{nat}boron carbide film, when prepared at slightly higher substrate temperature of 600 °C, the refractive index spectra was generated and it was found that the film have slightly higher refractive index 1.805 at 600 nm. Adatoms from the atomic clusters on the substrate surface coming from the target have relatively higher mobility due to thermal excitation at a higher substrate temperature which can affect the arrangement of atoms [174] during nucleation and growth of the films, resulting in film compaction hence higher film density [183]. For both PECVD and PLD techniques, structural densification is the reason for increase in refractive index. From the extinction coefficient spectra (Figure 6.5(b)), it can be seen that PLD 400C films have higher absorption as compared to that of PECVD -100V films at the wavelength range of 500- 900 nm. It is seen from XPS analysis that PLD 400C film is dominantly stoichiometric while PECVD -100V film is dominantly super-stoichiometric. These super-stoichiometric films have been reported to have a lower extinction coefficient and are therefore less absorbing in this region [118, 138].

Total residual stress

Residual stress calculations by wafer curvature method revealed that the nature of stress was tensile for PECVD -100V film, while it was compressive for the PLD 400C film (Table 6.1). Several internal and external factors can result in residual stresses in the films, such as thermal stress, internal stresses arising from the lattice mismatch between the film and substrate during grain growth [184, 185], various defects, and compositional changes due to exposure in ambiance after deposition. Synthesis of thin films occurs by formation of islands by adatoms, followed by grain growth, and coalescence of the grains/ grain boundary formation. Neighboring grains tend to form grain boundaries via island coalescence in order to reduce interfacial energy leading to formation of continuous films on the surface of the substrate. Grain boundary formation is considered to be the origin of the tensile stresses in the films [186]. The internal stress of another PECVD deposited film prepared at -150 V self-bias (identified as PECVD -150V film) was measured. It was in fact found to be compressive in nature with a magnitude -108 MPa. Change of stress profile from tensile to compressive in this case could have occurred due to diffusion and accumulation of adatoms across grain boundaries [187], owing to the increased kinetic energy of the incoming adatoms at higher substrate self-bias. As mentioned earlier, PLD technique also yields films with compressive internal stress with magnitude much higher than PECVD deposited films. The thin film stress behavior primarily depends on the deposited material, but it is also dependent on the temperature of the substrate and growth rate of the films. In our study, PECVD deposited films have much higher growth rate (124 nm/ min) than PLD films (5 nm/ min). Owing to this fact, the diffusion and incorporation of ad-atoms across the grain boundary decreases as the growth rate increases, resulting in decreased compressive stress [188]. This explains our observations on the PLD 400C film where we found high compressive stress. When depositions are carried out at increased substrate temperature from 400 °C to 600 °C in case of PLD, internal stress was found to increase slightly, still remaining compressive. Film thickness is also found to affect total residual stress in the films. With increasing thickness, the grain size in the films increases, reducing interfacial stresses in the grain boundaries, which reduce overall residual stresses in the films [187]. In this study, the higher thickness (1242 nm) of PECVD -100V film as compared to PLD 400C film (318 nm) can be correlated to the lower value of residual stress in PECVD films.

5. Summary:

This study describes a comparative study on use of PECVD and PLD techniques for deposition of ^{nat}boron carbide ($^{nat}B_xC$) thin films. Adhesion, crystallinity, chemical bonding, optical properties, and residual stress of the deposited films have been investigated and compared. Such films contain certain prominent dissimilarities in the derivative properties, as a consequence of using two essentially different deposition techniques.

(1) Both the films were observed to have multiple phases of boron carbide, stoichiometric B_4C phase being dominant in PLD deposited film while super-stoichiometric B_xC (x >4) phase was the dominant one in PECVD deposited film.

(2) Film deposited by PLD technique turned out to be amorphous, while the PECVD deposited one was crystalline, for the same substrate temperature 400 °C.

(3) Both films have a low coefficient of friction, PECVD deposited film showing slightly better lubricity and adhesion.

(4) PECVD technique offers a much higher deposition rate compared to PLD which is advantageous when deposition of thicker films (~ μm) is a necessity.

(5) Refractive index spectra were similar for both the films with PECVD deposited film showing slightly higher value in the entire measurement range (500- 900 nm).

Residual stress for PECVD -100V film was found to be tensile while the same for PLD 400C film was compressive. In conclusion, the PECVD technique provides conformal, crystalline, super-hard $^{nat}B_xC$ films at a high deposition rate. The PLD technique is useful for stoichiometric or near-stoichiometric thin film deposition. A careful analysis of the characterization results reveals that it is possible to utilize each of the processes successfully to deposit high quality functional $^{nat}B_xC$ thin films.

Chapter 7 : Conclusion(s) and Future Scope:

7.1 Conclusion(s):

In this study, capacitively coupled radio frequency (13.56 MHz) PECVD system was utilized to deposit single layered ^{nat}boron carbide thin films on different substrates for various applications. During depositions, substrate “self-bias” and deposition time was chosen as variables keeping all other parameters constant. As-deposited samples were investigated with the help of requisite characterization techniques to study different physical and chemical properties. Efforts have been made to establish correlation between structure, composition, and morphology of the samples with the derivative properties.

First section of the study was focused on deposition of environmentally stable, good-quality ^{nat}boron carbide thin films and determination of total macroscopic cross section (Σ_t) for thermal neutrons for the same. Five samples were deposited at different self-bias values to achieve compositional variation on Si (100) and Aluminium substrates. Deposition rate, chemical composition, oxidation state, bonding between different constituent elements, and surface morphology was investigated as a function of DC self-bias. In addition, total macroscopic cross-section (Σ_t) for neutron absorption of the films was investigated as a function of boron to carbon atomic ratio ($\boldsymbol{B/C}$) with the help of neutron transmission measurement technique. This study led to the conclusion that DC “self-bias” indeed is a deterministic factor for film composition, as well as Σ_t. Lower self-bias (-75V) during deposition lead to formation of super-stoichiometric films with $\boldsymbol{B/C}$ ratio > 5. However, Σ_t was found to increase with self-bias (Σ_t ~ 273.38 $\boldsymbol{cm^{-1}}$) as a result of structural densification. This study enabled us to determine optimum deposition conditions for synthesis of ^{nat}boron carbide thin films with reasonable Σ_t and good environmental stability.

After successful deposition of stable ^{nat}boron carbide thin films on metallic (Aluminium) and semiconducting (Si (100)) substrates for assessment of their neutron absorption cross section, we investigated optical properties of the films in the wavelength range 300nm -1200 nm, as a function of film composition. Optical constants: refractive index (n), extinction co-efficient (k), absorption co-efficient (α) and also film thickness (t) were derived from the optical transmission spectra. Interesting details of the analytical method and modeling used for determining the optical constants have also been included. Direct and indirect band gap of the ^{nat}boron carbide films were calculated using Tauc plots. It was found that band gap is mainly dependent on the composition, and both direct and indirect band gap was found to decrease with increase in carbon content in the films. Soft X-ray reflectivity measurement in the range 40Å - 360Å using a synchrotron source revealed that the films offer a maximum of 81% grazing angle reflectivity near boron K_α edge for -200V film which decreases at higher self-bias owing to film degradation. This study demonstrated the usefulness of ^{nat}boron carbide thin films as optical material in soft x-ray region. In addition, transparency of the deposited films in the NIR range indicated utility of the films as protective and anti-reflecting optical material in that region. Tunability of optical properties with careful control of deposition parameters was also established.

^{nat}Boron carbide thin films have already been established as useful material for tribological applications; however there is a scarcity of reports presenting the tribological behaviour of the films having dependence on the PECVD process parameters. Third section of this study narrates the findings regarding investigation of tribological properties of ^{nat}boron carbide thin films: mainly friction and wear behavior as a function of film composition and thickness. Lower self-bias was found to be advantageous for synthesis of films having superior hardness. Lower self-bias was also found to be advantageous for superior wear performance. Higher film thickness was found to improve friction properties.

Lastly, a comparative study of physical, chemical, and structural properties of PECVD and PLD deposited $^{nat}B_xC$ films were performed. Differences in film properties were expected to arise mainly on account of different characteristic deposition methodologies of the two techniques. Mechanical properties like hardness, coefficient of friction and adhesion were investigated, these being primary requirements for many functional applications. In addition to optical properties, total residual stress in the films has been studied with the help of optical interferometry and it was found that total residual stress in PLD deposited films was almost 10 times higher in magnitude than PECVD films. PECVD technique provided conformal, crystalline, super-hard $^{nat}B_xC$ films at a higher deposition rate. PLD technique was found to be useful for stoichiometric $^{nat}B_xC$ thin film deposition. This study revealed that depending upon the requirement; it is possible to utilize each of the process successfully to deposit high quality functional $^{nat}B_xC$ thin films.

7.2 Future scope:

The work described in this thesis needs to be taken forward in terms of both experimental and theoretical simulations. Following are some recommendations for further studies:

i. Boron carbide thin films are excellent material for neutron detection. In addition, they are potential candidate for micro and nano-electronic applications. Hence electronic properties of these films needs to be studied as a function of plasma parameters to investigate their usefulness as p-n junction semiconductor and also hetero-junction based portable solid state neutron detectors.

ii. Plasma parameters can be studied for this RF-PECVD system via intrusive and non-intrusive plasma diagnostic methods. Since we are using RF frequency for plasma generation, specifically designed probe, for example RF compensated Langmuir probe is necessary for plasma diagnostics. Optical emission spectroscopy can also be employed which will provide an understanding of the plasma conditions during depositions. It will also help in establishing a correlation of the plasma parameters with the composition and structure of the deposited films.

iii. Simulation studies of the thin film growth mechanism under well studied experimental conditions will enable fine control for growth of ^{nat}boron carbide thin films of choice.

iv. The boron carbide thin films needs to be investigated further as thermoelectric material also as electro-catalyst.

Chapter 8 : References:

[1] S. Mondal, E. Bykova, S. Dey, S.I. Ali, N. Dubrovinskaia, L. Dubrovinsky, G. Parakhonskiy, S. Van Smaalen, Disorder and defects are not intrinsic to boron carbide, Scientific reports, 6 (2016) 19330.

[2] A. Suri, C. Subramanian, J. Sonber, T.C. Murthy, Synthesis and consolidation of boron carbide: a review, International Materials Reviews, 55 (2010) 4-40.

[3] V. Domnich, S. Reynaud, R.A. Haber, M. Chhowalla, Boron carbide: structure, properties, and stability under stress, Journal of the American Ceramic Society, 94 (2011) 3605-3628.

[4] A.O. Sezer, J. Brand, Chemical vapor deposition of boron carbide, Materials Science and Engineering: B, 79 (2001) 191-202.

[5] S. Adenwalla, P. Welsch, A. Harken, J.I. Brand, A. Sezer, B.W. Robertson, Boron carbide/n-silicon carbide heterojunction diodes, Applied physics letters, 79 (2001) 4357-4359.

[6] S.D. Hwang, D. Byun, N. Ianno, P.A. Dowben, H. Kim, Fabrication of boron‐carbide/boron heterojunction devices, Applied physics letters, 68 (1996) 1495-1497.

[7] S. Lee, J. Mazurowski, G. Ramseyer, P.A. Dowben, Characterization of boron carbide thin films fabricated by plasma enhanced chemical vapor deposition from boranes, Journal of applied physics, 72 (1992) 4925-4933.

[8] A. Caruso, P.A. Dowben, S. Balkir, N. Schemm, K. Osberg, R. Fairchild, O.B. Flores, S. Balaz, A. Harken, B.W. Robertson, The all boron carbide diode neutron detector: Comparison with theory, Materials Science and Engineering: B, 135 (2006) 129-133.

[9] Y.C. Kausala Mylvaganam, Weidong Liu, Mei Liu, Liangchi Zhang, Hard thin films: Applications and challenges, in: M. Aliofkhazraei (Ed.) Anti-abrasive nanocoatings : current and future applications Woodhead Publishing2015, pp. 543-567.

[10] A. West, ’Solid State Chemistry’John willey & Sons, Singapore, 2003.

[11] R.D. Gould, S. Kasap, A.K. Ray, Thin Films, in: S. Kasap, P. Capper (Eds.) Springer Handbook of Electronic and Photonic Materials, Springer International Publishing, Cham, 2017, pp. 1-1.

[12] J. Thirumalai, Introductory Chapter: The Prominence of Thin Film Science in Technological Scale, in: J. Thirumalai (Ed.) Thin Film Processes IntechOpen2017.

[13] P. Savale, Physical vapor deposition (PVD) methods for synthesis of thin films: A comparative study, Arch. Appl. Sci. Res, 8 (2016) 1-8.

[14] M. Rao, M. Shekhawat, A brief Survey on Basic Properties of thin Films for Device Application, International Journal of Modern Physics: Conference Series, World Scientific, 2013, pp. 576-582.

[15] Y. Gao, H. Niu, C. Zeng, Q. Chen, Preparation and characterization of single-crystalline bismuth nanowires by a low-temperature solvothermal process, Chemical physics letters, 367 (2003) 141-144.

[16] K. Robbie, G. Beydaghyan, T. Brown, C. Dean, J. Adams, C. Buzea, Ultrahigh vacuum glancing angle deposition system for thin films with controlled three-dimensional nanoscale structure, Review of Scientific Instruments, 75 (2004) 1089-1097.

[17] A.K. Khanra, Production of boron carbide powder by carbothermal synthesis of gel material, Bulletin of Materials Science, 30 (2007) 93-96.

[18] M.M. Balakrishnarajan, P.D. Pancharatna, R. Hoffmann, Structure and bonding in boron carbide: The invincibility of imperfections, New Journal of Chemistry, 31 (2007) 473-485.

[19] C. Kunka, A. Awasthi, G. Subhash, Crystallographic and spectral equivalence of boron-carbide polymorphs, Scripta Materialia, 122 (2016) 82-85.

[20] K.B.a.S.K.S. R.M. Mohanty, Evolution of Crystallographic Structures and Phases in Micropyretically Formed Boron Rich Boron Carbide – a New Material System, in: C. Sikalidis (Ed.) Advances in Ceramics, IntechOpen2011.

[21] M. Bouchacourt, F. Thevenot, Analytical investigations in the B・ C system, Journal of the less common metals, 82 (1981) 219-226.

[22] J. Sun, H. Ling, W. Pan, N. Xu, Z. Ying, W. Shen, J. Wu, Chemical structure and micro-mechanical properties of ultra-thin films of boron carbide prepared by pulsed-laser deposition, Tribology Letters, 17 (2004) 99-104.

[23] C. Wood, Transport properties of boron carbide, AIP Conference Proceedings, AIP, 1986, pp. 206-215.

[24] AZoM, Boron Carbide (B4C) - Properties and Information about Boron Carbide, 2001.

[25] S. Mondal, A.K. Banthia, Low-temperature synthetic route for boron carbide, Journal of the European Ceramic Society, 25 (2005) 287-291.

[26] K.S.S. Harsha, Principles of Physical Vapor Deposition of Thin Films
Elsevier Science, Great Britain, 2006, pp. 1176.

[27] J. George, Preparation of thin films, Marcel Dekkar, Inc., New York, 1992.

[28] K.L. Chopra, Thin film phenomena, McGraw-Hill Book Company, New York, 1969.

[29] J.H.O.a.J.M.B.J. C. F. Powell, Vapor Deposition, Wiley, New York, 1967.

[30] K.K. Ajay Vasudeo Rane, V.K. Abitha, Sabu Thomas, Methods for Synthesis of Nanoparticles and Fabrication of Nanocomposites, in: O.S.O. Sneha Mohan Bhagyaraj, Nandakumar Kalarikkal, Sabu Thomas (Ed.) Synthesis of Inorganic Nanomaterials, Woodhead Publishing2018.

[31] M.A.a.N. Ali, PVD Technology in Fabrication of Micro- and Nanostructured Coatings, in: G.F.B. Saleem Hashmi, Chester J. Van Tyne, Bekir Yilbas (Ed.) Comprehensive Materials Processing, Elsevier2014, pp. 49-84.

[32] H. Geng, Semiconductor Manufacturing Handbook, McGraw-Hill, New York, 2004.

[33] U. Helmersson, M. Lattemann, J. Bohlmark, A.P. Ehiasarian, J.T. Gudmundsson, Ionized physical vapor deposition (IPVD): A review of technology and applications, Thin solid films, 513 (2006) 1-24.

[34] P.M. Martin, Handbook of deposition technologies for films and coatings: science, applications and technology, William Andrew2009.

[35] F.S. Jamie H. Warner, Alicja Bachmatiuk and Mark H. Rümmeli, Methods for Obtaining Graphene, in: F.S. Jamie H. Warner, Alicja Bachmatiuk and Mark H. Rümmeli (Ed.) Graphene, Elsevier2013, pp. 129-228.

[36] M.F.V. V.G. Varanasi, T. Odatsu, A. Ilyas, S.M. Iqbal and P.B. Aswath, Surface Modifications and Surface Characterization of Biomaterials Used in Bone Healing, in: S.B.a.A. Bandyopadhyay (Ed.) Materials for Bone Disorders, Academic Press2017, pp. 405-452.

[37] F.F. Chen, Introduction to plasma physics and controlled fusion, Springer1984.

[38] N.R. Council, P.S. Committee, Plasma processing of materials: scientific opportunities and technological challenges, National Academies Press1991.

[39] PIE Scientific LLC., 2018.

[40] Y.A. Lebedev, Microwave discharges: generation and diagnostics, Journal of Physics: Conference Series, IOP Publishing, 2010, pp. 012016.

[41] A. Breen, V. Milosavljević, D.P. Dowling, Influence of gas type on the thermal efficiency of microwave plasmas for the sintering of metal powders, Plasma Chemistry and Plasma Processing, 31 (2011) 771.

[42] A.G.a.R.D. Tarey, Understanding plasma sources, Current science, 83 (2002).

[43] H. Conrads, M. Schmidt, Plasma generation and plasma sources, Plasma Sources Science and Technology, 9 (2000) 441.

[44] A. Bogaerts, E. Neyts, R. Gijbels, J. Van der Mullen, Gas discharge plasmas and their applications, Spectrochimica Acta Part B: Atomic Spectroscopy, 57 (2002) 609-658.

[45] M. Mehdizadeh, Plasma applicators at RF and microwave frequencies, in: M. Mehdizadeh (Ed.) Microwave/RF Applicators and Probes, William Andrew Publishing2015, pp. 335-363.

[46] V. Godyak, R. Piejak, Abnormally low electron energy and heating-mode transition in a low-pressure argon rf discharge at 13.56 MHz, Physical review letters, 65 (1990) 996.

[47] Y. Okuno, Y. Ohtsu, C. Komatsu, H. Fujita, Measurements of electron energy distribution function in an asymmetric radio‐frequency discharge plasma, Journal of applied physics, 73 (1993) 1612-1616.

[48] Y. Ohtsu, Y. Okuno, H. Fujita, Observation of radio‐frequency discharges at various driving frequencies, Journal of applied physics, 73 (1993) 2155-2159.

[49] P. Fauchais, A. Vardelle, Thermal plasmas, IEEE Transactions on Plasma Science, 25 (1997) 1258-1280.

[50] J. Heberlein, New approaches in thermal plasma technology, Pure and applied chemistry, 74 (2002) 327-335.

[51] E. Pfender, Thermal plasma technology: Where do we stand and where are we going?, Plasma chemistry and plasma processing, 19 (1999) 1-31.

[52] J. Heberlein, A.B. Murphy, Thermal plasma waste treatment, Journal of Physics D: Applied Physics, 41 (2008) 053001.

[53] S. Vepřek, S. Rambert, M. Heintze, F. Mattenberger, M. Jurčik-Rajman, W. Portmann, D. Ringer, U. Stiefel, Development of plasma CVD and feasibility study of boron carbide in-situ coatings for tokamaks, Journal of Nuclear Materials, 162 (1989) 724-731.

[54] J. Winter, H. Esser, H. Reimer, L. Grobusch, J. Von Seggern, P. Wienhold, Borontrimethyl B (CH3) 3—A less hazardous substance for boronization, Journal of Nuclear Materials, 176 (1990) 486-489.

[55] V.K. Alimov, D. Bogomolov, M. Churaeva, A. Gorodetsky, S. Kanashenko, A. Kanaev, S.Y. Rybakov, V. Sharapov, A. Zakharov, R.K. Zalavutdinov, Characterization of aB/C: H films deposited from different boron containing precursors, Journal of nuclear materials, 196 (1992) 670-675.

[56] O. Buzhinsky, E. Azizov, A. Belov, S. Grashin, A. Krasilnikov, I. Kovan, C. Mirnov, A. Petrov, V. Petrov, D. Portnov, A simple boronization technique for T-3M and T-11M tokamak chambers, Journal of nuclear materials, 191 (1992) 1413-1416.

[57] H. Künzli, P. Gantenbein, R. Steiner, P. Oelhafen, Influence of B2H6/CH4 and B (CH3) 3 as process gas on boron carbide coatings: an in situ photoelectron spectroscopy study, Journal of nuclear materials, 196 (1992) 622-626.

[58] D. Byun, B. Spady, N. Ianno, P. Dowben, Comparison of different chemical vapor deposition methodologies for the fabrication of heterojunction boron-carbide diodes, Nanostructured Materials, 5 (1995) 465-471.

[59] A.A. Ahmad, N. Ianno, P. Snyder, D. Welipitiya, D. Byun, P.A. Dowben, Optical properties of boron carbide (B5C) thin films fabricated by plasma‐enhanced chemical‐vapor deposition, Journal of applied physics, 79 (1996) 8643-8647.

[60] K.-W. Lee, S.J. Harris, Boron carbide films grown from microwave plasma chemical vapor deposition, Diamond and related materials, 7 (1998) 1539-1543.

[61] P.A. Dowben, O. Kizilkaya, J. Liu, B. Montag, K. Nelson, I. Sabirianov, J.I. Brand, 3d transition metal doping of semiconducting boron carbides, Materials Letters, 63 (2009) 72-74.

[62] U. Kuhlmann, H. Werheit, K. Schwetz, Distribution of carbon atoms on the boron carbide structure elements, Journal of alloys and compounds, 189 (1992) 249-258.

[63] H. Werheit, Boron-rich solids: a chance for high-efficiency high-temperature thermoelectric energy conversion, Materials Science and Engineering: B, 29 (1995) 228-232.

[64] R. Schmechel, H. Werheit, Correlation between structural defects and electronic properties of icosahedral boron-rich solids, Journal of Physics: Condensed Matter, 11 (1999) 6803.

[65] H. Werheit, M. Laux, U. Kuhlmann, Interband and Gap State Related Transitions in β‐Rhombohedral Boron, physica status solidi (b), 176 (1993) 415-432.

[66] H. Werheit, U. Kuhlmann, M. Laux, T. Lundström, Structural and Electronic Properties of Carbon‐Doped β‐Rhombohedral Boron, physica status solidi (b), 179 (1993) 489-511.

[67] U. Kuhlmann, H. Werheit, On the microstructure of boron carbide, Solid state communications, 83 (1992) 849-852.

[68] H. Werheit, U. Kuhlmann, H. Rotter, S. Shalamberidze, Isotopic effects on the phonon modes in boron carbide, Journal of Physics: Condensed Matter, 22 (2010) 395401.

[69] H. Werheit, T. Au, R. Schmechel, S. Shalamberidze, G. Kalandadze, A. Eristavi, IR-active phonons and structure elements of isotope-enriched boron carbide, Journal of Solid State Chemistry, 154 (2000) 79-86.

[70] H. Werheit, S. Shalamberidze, Advanced microstructure of boron carbide, Journal of Physics: Condensed Matter, 24 (2012) 385406.

[71] J. Liu, G. Luo, W.-N. Mei, O. Kizilkaya, E.D. Shepherd, J.I. Brand, P.A. Dowben, The local structure of transition metal doped semiconducting boron carbides, Journal of Physics D: Applied Physics, 43 (2010) 085403.

[72] N. Hong, L. Crow, S. Adenwalla, Time-of-flight neutron detection using PECVD grown boron carbide diode detector, Nuclear Instruments and Methods in Physics Research Section A: Accelerators, Spectrometers, Detectors and Associated Equipment, 708 (2013) 19-23.

[73] E. Echeverria, B. Dong, G. Peterson, J.P. Silva, E.R. Wilson, M.S. Driver, Y.-S. Jun, G.D. Stucky, S. Knight, T. Hofmann, Semiconducting boron carbides with better charge extraction through the addition of pyridine moieties, Journal of Physics D: Applied Physics, 49 (2016) 355302.

[74] B. Dong, R. James, J.A. Kelber, PECVD of boron carbide/aromatic composite films: Precursor stability and resonance stabilization energy, Surface and Coatings Technology, 290 (2016) 94-99.

[75] B.J. Nordell, C.L. Keck, T.D. Nguyen, A. Caruso, S.S. Purohit, W.A. Lanford, D. Dutta, D. Gidley, P. Henry, S.W. King, Tuning the properties of a complex disordered material: Full factorial investigation of PECVD-grown amorphous hydrogenated boron carbide, Materials Chemistry and Physics, 173 (2016) 268-284.

[76] M. Nastasi, G. Peterson, Q. Su, Y. Wang, N. Ianno, N. Benker, E. Echeverría, A.J. Yost, J. Kelber, B. Dong, Electrical and structural characterization of neutron irradiated amorphous boron carbide/silicon pn heterojunctions, Nuclear Instruments and Methods in Physics Research Section B: Beam Interactions with Materials and Atoms, 432 (2018) 48-54.

[77] A. Oyelade, A.J. Yost, N. Benker, B. Dong, S. Knight, M. Schubert, P.A. Dowben, J.A. Kelber, Composition-Dependent Charge Transport in Boron Carbides Alloyed with Aromatics: Plasma Enhanced Chemical Vapor Deposition Aniline/Orthocarborane Films, Langmuir, 34 (2018) 12007-12016.

[78] A. Bute, R. Kar, S. Chopade, S. Desai, M. Deo, P. Rao, N. Chand, S. Kumar, K. Singh, D. Patil, Effect of self-bias on the elemental composition and neutron absorption of boron carbide films deposited by RF plasma enhanced CVD, Materials Chemistry and Physics, 182 (2016) 62-71.

[79] Z. Ying, D. Yu, H. Ling, N. Xu, Y. Lu, J. Sun, J. Wu, Synthesis of BCN thin films by nitrogen ion beam assisted pulsed laser deposition from a B4C target, Diamond and related materials, 16 (2007) 1579-1585.

[80] Ortho-carborane, WIKIMEDIA, 2019.

[81] A. Auroux, Calorimetry and thermal methods in catalysis, DOI (2013).

[82] M. Walock, Nanocomposite coatings based on quaternary metalnitrogen, Paris, ENSAM, 2012.

[83] INSTRON, INSTRON, Massachusetts, US, 2019.

[84] R.S. Kalidindi, R. Subasri, Sol-gel nanocomposite hard coatings, Anti-Abrasive Nanocoatings, Elsevier2015, pp. 105-136.

[85] T. Ichiki, T. Momose, T. Yoshida, Effects of the substrate bias on the formation of cubic boron nitride by inductively coupled plasma enhanced chemical vapor deposition, Journal of applied physics, 75 (1994) 1330-1334.

[86] M.A. Mannan, M. Nagano, T. Kida, N. Hirao, Y. Baba, Characterization of BCN films synthesized by radiofrequency plasma enhanced chemical vapor deposition, Journal of Physics and Chemistry of Solids, 70 (2009) 20-25.

[87] R. Bao, D.B. Chrisey, Chemical states of carbon in amorphous boron carbide thin films deposited by radio frequency magnetron sputtering, Thin Solid Films, 519 (2010) 164-168.

[88] I. Lopez-Quintas, M. Oujja, M. Sanz, A. Benitez-Canete, R.J. Chater, M.V. Canamares, J.F. Marco, M. Castillejo, Micrometric rods grown by nanosecond pulsed laser deposition of boron carbide, Applied Surface Science, 328 (2015) 170-176.

[89] W. Cermignani, T.E. Paulson, C. Onneby, C.G. Pantano, Synthesis and characterization of boron-doped carbons, Carbon, 33 (1995) 367-374.

[90] T.T. Xu, J.-G. Zheng, N. Wu, A.W. Nicholls, J.R. Roth, D.A. Dikin, R.S. Ruoff, Crystalline boron nanoribbons: synthesis and characterization, Nano Letters, 4 (2004) 963-968.

[91] R. James, F.L. Pasquale, J.A. Kelber, Plasma-enhanced chemical vapor deposition of ortho-carborane: structural insights and interaction with Cu overlayers, Journal of Physics: Condensed Matter, 25 (2013) 355004.

[92] L. Jacobsohn, R. Schulze, M.M. Da Costa, M. Nastasi, X-ray photoelectron spectroscopy investigation of boron carbide films deposited by sputtering, Surface Science, 572 (2004) 418-424.

[93] S. Massey, D. Roy, A. Adnot, Study of natural ageing of polypropylene by X-ray photoelectron spectroscopy, Nuclear Instruments and Methods in Physics Research Section B: Beam Interactions with Materials and Atoms, 208 (2003) 236-241.

[94] C.-R. Lin, H.-M. Chang, C.-K. Chang, Fabrication of high transparency diamond-like carbon film coating on D263T glass at room temperature as an antireflection layer, International Journal of Photoenergy, 2013 (2013).

[95] K. Shirai, S. Emura, S.i. Gonda, Y. Kumashiro, Infrared study of amorphous B1− x C x films, Journal of applied physics, 78 (1995) 3392-3400.

[96] R.E. Clark, Nuclear fusion research: understanding plasma-surface interactions, Springer Science & Business Media2005.

[97] P. Konarski, A. Mierzejewska, B4C/Mo/Si and Ta2O5/Ta nanostructures analysed by ultra-low energy argon ion beams, Applied surface science, 203 (2003) 354-358.

[98] A. Grill, Cold Plasma in Materials Fabrication from Fundamentals to Applications' IEEE Press, DOI (1993).

[99] J. Ye, S. Ulrich, K. Sell, H. Leiste, M. Stüber, H. Holleck, Correlation between plasma particle fluxes, microstructure and properties of titanium diboride thin films, Surface and Coatings Technology, 174 (2003) 959-963.

[100] P. de Almeida, J. Räisänen, Atomic displacement in solids: analysis of the primary event and the collision cascade. Part I: Neutron and positive ion irradiation, European journal of physics, 26 (2005) 371.

[101] T. Stoto, L. Zuppiroli, J. Pelissier, Absence of defect clusters in electron irradiated boron carbide, Radiation effects, 90 (1985) 161-170.

[102] G. Blumenstock, R.A. Keski-Kuha, Ion-beam-deposited boron carbide coatings for the extreme ultraviolet, Applied optics, 33 (1994) 5962-5963.

[103] R. Soufli, A.L. Aquila, F. Salmassi, M. Fernández-Perea, E.M. Gullikson, Optical constants of magnetron-sputtered boron carbide thin films from photoabsorption data in the range 30 to 770 eV, Applied optics, 47 (2008) 4633-4639.

[104] P. Boher, P. Houdy, P. Kaikati, R.J. Barchewitz, L. Van Ijzendoorn, Z. Li, D.J. Smith, J. Joud, Comparative study of carbon and boron carbide spacing layers inside soft x-ray mirrors, Advanced X-ray/EUV radiation sources and applications, International Society for Optics and Photonics, 1991, pp. 165-179.

[105] C. Chiang, H. Holleck, O. Meyer, Properties of RF sputtered B4C thin films, Nuclear Instruments and Methods in Physics Research Section B: Beam Interactions with Materials and Atoms, 91 (1994) 692-695.

[106] C. Murray, C. Flannery, I. Streiter, S. Schulz, M. Baklanov, K. Mogilnikov, C. Himcinschi, M. Friedrich, D. Zahn, T. Gessner, Comparison of techniques to characterise the density, porosity and elastic modulus of porous low-k SiO2 xerogel films, Microelectronic Engineering, 60 (2002) 133-141.

[107] S. Jena, R. Tokas, S. Thakur, N. Sahoo, Optical properties of electron beam evaporated ZrO 2: 10% SiO 2 thin films: dependence on structure, Indian Journal of Physics, 90 (2016) 951-957.

[108] S. Jena, R. Tokas, N. Kamble, S. Thakur, D. Bhattacharyya, N. Sahoo, Investigation of elastic and optical properties of electron beam evaporated ZrO2–MgO composite thin films, Thin Solid Films, 537 (2013) 163-170.

[109] N. Kamble, R. Tokas, A. Biswas, S. Thakur, D. Bhattacharyya, N. Sahoo, Determination of the optical constants of HfO2–SiO2 composite thin films through reverse fitting of transmission spectra, Vacuum, 86 (2011) 422-428.

[110] P.W. Carey, Plasma Enhanced Chemical Vapour Deposition of Thin Carbon Films, School of Electronic Engineering, Dublin City University, Dublin, Ireland, 1989.

[111] H. Hey, B. Sluijk, D. Hemmes, Ion bombardment: A determining factor in plasma CVD, Solid State Technology, 33 (1990) 139-145.

[112] B.-Y. Kim, S.-H. Lee, S.-G. Park, K.-Y. Oh, J. Song, D.-H. Kim, Comparison study for TiN films deposited from different method: chemical vapor deposition and atomic layer deposition, MRS Online Proceedings Library Archive, 672 (2001).

[113] D. Li, M. Carette, A. Granier, J. Landesman, A. Goullet, Effect of ion bombardment on the structural and optical properties of TiO2 thin films deposited from oxygen/titanium tetraisopropoxide inductively coupled plasma, Thin Solid Films, 589 (2015) 783-791.

[114] H. Pedersen, M. Chubarov, H. Högberg, J. Jensen, A. Henry, On the effect of water and oxygen in chemical vapor deposition of boron nitride, Thin solid films, 520 (2012) 5889-5893.

[115] V. Dimitrov, S. Sakka, Electronic oxide polarizability and optical basicity of simple oxides. I, Journal of Applied Physics, 79 (1996) 1736-1740.

[116] G. Koster, G. Rijnders, In situ characterization of thin film growth, Elsevier2011.

[117] C. Ronning, D. Schwen, S. Eyhusen, U. Vetter, H. Hofsäss, Ion beam synthesis of boron carbide thin films, Surface and Coatings Technology, 158 (2002) 382-387.

[118] J. Jensen, A. Oelkers, R. Toivola, D.C. Johnson, J. Elam, S. George, X-ray reflectivity characterization of ZnO/Al2O3 multilayers prepared by atomic layer deposition, Chemistry of materials, 14 (2002) 2276-2282.

[119] O. Stenzel, The Physics of Thin Film Optical Spectra, vol. 44, Springer Series in Surface Sciences, 9 (2005) 1689-1699.

[120] M.A. Abdullah, S. Saleman, N. Tamaldin, M.S. Suhaimi, Reducing wear and friction by means of lubricants mixtures, Procedia Engineering, 68 (2013) 338-344.

[121] D. Teer, New solid lubricant coatings, Wear, 251 (2001) 1068-1074.

[122] A. Koutsomichalis, N. Vaxevanidis, G. Petropoulos, E. Xatzaki, A. Mourlas, S. Antoniou, Tribological coatings for aerospace applications and the case of WC-Co plasma spray coatings, Tribology in industry, 31 (2009) 37-42.

[123] K. Holmberg, A. Matthews, Coatings tribology: properties, mechanisms, techniques and applications in surface engineering, Elsevier2009.

[124] J.C. Qian, Z. Zhou, C. Yan, D. Li, K. Li, S. Descartes, R. Chromik, W. Zhang, I. Bello, L. Martinu, Tailoring the mechanical and tribological properties of sputtered boron carbide films via the B1− xCx composition, Surface and Coatings Technology, 267 (2015) 2-7.

[125] Y.G. Gogotsi, A. Koval'chenko, I. Kossko, Tribochemical interactions of boron carbides against steel, Wear, 154 (1992) 133-140.

[126] T. Hu, L. Steihl, W. Rafaniello, T. Fawcett, D.D. Hawn, J.G. Mashall, S.J. Rozeveld, C.L. Putzig, J.H. Blackson, W. Cermignani, Structures and properties of disordered boron carbide coatings generated by magnetron sputtering, Thin Solid Films, 332 (1998) 80-86.

[127] S. Ulrich, H. Ehrhardt, J. Schwan, R. Samlenski, R. Brenn, Subplantation effect in magnetron sputtered superhard boron carbide thin films, Diamond and related materials, 7 (1998) 835-838.

[128] J. Hershberger, F. Kustas, Z. Rek, S. Yalisove, J. Bilello, Structure Determination of B 4 C and SiC Thin Films Via Synchrotron High-Resolution Diffraction, MRS Online Proceedings Library Archive, 505 (1997).

[129] S.H. Lin, B.J. Feldman, D. Li, Microhardness study of amorphous hydrogenated boron carbide deposited on a cathode substrate by plasma deposition, Applied physics letters, 69 (1996) 2373-2375.

[130] A. Annen, M. Saß, R. Beckmann, A. Von Keudell, W. Jacob, Structure of plasma-deposited amorphous hydrogenated boron-carbon thin films, Thin Solid Films, 312 (1998) 147-155.

[131] H.-S. Ahn, P. Cuong, K.-H. Shin, K.-S. Lee, Tribological behavior of sputtered boron carbide coatings and the influence of processing gas, Wear, 259 (2005) 807-813.

[132] T. Eckardt, K. Bewilogua, G. Van der Kolk, T. Hurkmans, T. Trinh, W. Fleischer, Improving tribological properties of sputtered boron carbide coatings by process modifications, Surface and Coatings technology, 126 (2000) 69-75.

[133] O. Knotek, E. Lugscheider, C. Siry, Tribological properties of B—C thin films deposited by magnetron-sputter-ion plating method, Surface and Coatings Technology, 91 (1997) 167-173.

[134] M. Abad, J. Sánchez-López, M. Brizuela, A. García-Luis, D. Shtansky, Influence of carbon chemical bonding on the tribological behavior of sputtered nanocomposite TiBC/aC coatings, Thin Solid Films, 518 (2010) 5546-5552.

[135] C. Wang, Y. Yang, Y.-W. Chung, Y. Zhang, S. Ouyang, Z. Xiao, K. Song, P. Li, Microstructure, hardness and toughness of boron carbide thin films deposited by pulse dc magnetron sputtering, Ceramics International, 42 (2016) 6342-6346.

[136] T. Maruyama, S. Arai, Electrochromic properties of niobium oxide thin films prepared by radio ‐ frequency magnetron sputtering method, Applied physics letters, 63 (1993) 869-870.

[137] R.F. Foster, H.E. Rebenne, R.E. LeBlanc, C.L. White, R. Arora, Rotating susceptor semiconductor wafer processing cluster tool module useful for tungsten CVD, Google Patents, 1994.

[138] A. Bute, S. Jena, D. Bhattacharya, S. Kumar, N. Chand, N. Keskar, S. Sinha, Composition dependent microstructure and optical properties of boron carbide (BxC) thin films deposited by radio frequency-plasma enhanced chemical vapour deposition technique, Materials Research Bulletin, 109 (2019) 175-182.

[139] P.W. Carey, Plasma Enhanced Chemical Vapour Deposition of Thin Carbon Films, School of Electronic Engineering, Dublin City University
Ireland, 1989.

[140] D. Reigada, R. Prioli, L. Jacobsohn, F. Freire Jr, Boron carbide films deposited by a magnetron sputter–ion plating process: film composition and tribological properties, Diamond and Related Materials, 9 (2000) 489-493.

[141] X. Yang, W.A. Goddard III, Q. An, Structure and Properties of Boron-Very-Rich Boron Carbides: B12 Icosahedra Linked through Bent CBB Chains, The Journal of Physical Chemistry C, 122 (2018) 2448-2453.

[142] K. Shirai, K. Sakuma, N. Uemura, Theoretical study of the structure of boron carbide B 13 C 2, Physical Review B, 90 (2014) 064109.

[143] A. Erdemir, C. Bindal, G. Fenske, Formation of ultralow friction surface films on boron carbide, Applied physics letters, 68 (1996) 1637-1639.

[144] J. Liu, The Photofragmentation Processes of the closo-Carborane and the Local Structure of Transition Metal Doped Semiconducting Boron Carbide Thin Films, DOI (2011).

[145] T. Zhang, D. Xie, N. Huang, Y. Leng, The effect of hydrogen on the tribological behavior of diamond like carbon (DLC) coatings sliding against Al2O3 in water environment, Surface and Coatings Technology, 320 (2017) 619-623.

[146] C. Cheng, K.M. Reddy, A. Hirata, T. Fujita, M. Chen, Structure and mechanical properties of boron-rich boron carbides, Journal of the European Ceramic Society, 37 (2017) 4514-4523.

[147] Y. Liu, Z. Pei, J. Gong, C. Sun, Effect of carbon content on microstructures, mechanical and tribological properties and thermal stability in WBC films, Surface and Coatings Technology, 291 (2016) 276-285.

[148] R.G. Bayer, R.G. Bayer, Mechanical wear prediction and prevention, M. Dekker New York1994.

[149] N. Vashishtha, S. Sapate, Effect of experimental parameters on wear response of thermally sprayed carbide based coatings, Materials Research, 22 (2019).

[150] S. Liza, N. Ohtake, H. Akasaka, J.M. Munoz‐Guijosa, Tribological and thermal stability study of nanoporous amorphous boron carbide films prepared by pulsed plasma chemical vapor deposition, Science and technology of advanced materials, 16 (2015) 035007.

[151] S. Miyake, S. Watanabe, M. Murakawa, R. Kaneko, T. Miyato, Tribological study of cubic boron nitride film, Thin Solid Films, 212 (1992) 262-266.

[152] E. Pascual, E. Martınez, J. Esteve, A. Lousa, Boron carbide thin films deposited by tuned-substrate RF magnetron sputtering, Diamond and related materials, 8 (1999) 402-405.

[153] M. Shokrieh, G. Javadpour, Penetration analysis of a projectile in ceramic composite armor, Composite structures, 82 (2008) 269-276.

[154] F. Thevenot, Boron carbide—a comprehensive review, Journal of the European Ceramic society, 6 (1990) 205-225.

[155] H. Takatsuka, M. Noda, Y. Yonekura, Y. Takeuchi, Y. Yamauchi, Development of high efficiency large area silicon thin film modules using VHF-PECVD, Solar Energy, 77 (2004) 951-960.

[156] R. Reif, Plasma enhanced chemical vapor deposition of thin crystalline semiconductor and conductor films, Journal of Vacuum Science & Technology A: Vacuum, Surfaces, and Films, 2 (1984) 429-435.

[157] H. Wojcik, M. Junige, W. Bartha, M. Albert, V. Neumann, U. Merkel, A. Peeva, J. Gluch, S. Menzel, F. Munnik, Physical characterization of PECVD and PEALD Ru (-C) films and comparison with PVD ruthenium film properties, Journal of The Electrochemical Society, 159 (2011) H166-H176.

[158] J. Joseph, S.G. Singh, S.R.K. Vanjari, Ultra-smooth e-beam evaporated amorphous silicon thin films–A viable alternative for PECVD amorphous silicon thin films for MEMS applications, Materials Letters, 197 (2017) 52-55.

[159] C. Cibert, H. Hidalgo, C. Champeaux, P. Tristant, C. Tixier, J. Desmaison, A. Catherinot, Properties of aluminum oxide thin films deposited by pulsed laser deposition and plasma enhanced chemical vapor deposition, Thin Solid Films, 516 (2008) 1290-1296.

[160] K. Weiss, S. Riedel, S. Schulz, M. Schwerd, H. Helneder, H. Wendt, T. Gessner, Development of different copper seed layers with respect to the copper electroplating process, Microelectronic Engineering, 50 (2000) 433-440.

[161] S.W. King, M. French, G. Xu, B. French, M. Jaehnig, J. Bielefeld, J. Brockman, M. Kuhn, Valence band offset and Schottky barrier at amorphous boron and boron carbide interfaces with silicon and copper, Applied Surface Science, 285 (2013) 545-551.

[162] P. Chaudhari, A. Singh, A. Topkar, R. Dusane, Hot wire chemical vapor deposited boron carbide thin film/crystalline silicon diode for neutron detection application, Solid-State Electronics, 78 (2012) 156-158.

[163] S. Sveen, J. Andersson, R. M'Saoubi, M. Olsson, Scratch adhesion characteristics of PVD TiAlN deposited on high speed steel, cemented carbide and PCBN substrates, Wear, 308 (2013) 133-141.

[164] D. He, L. Shang, Z. Lu, G. Zhang, L. Wang, Q. Xue, Tailoring the mechanical and tribological properties of B4C/aC coatings by controlling the boron carbide content, Surface and Coatings Technology, 329 (2017) 11-18.

[165] K.D. Rao, D. Udupa, C. Prathap, A. Rathod, R. Balasubramaniam, N. Sahoo, Optical coherence tomography for shape and radius of curvature measurements of deeply curved machined metallic surfaces: a comparison with two-beam laser interferometry, Optics and Lasers in Engineering, 66 (2015) 204-209.

[166] S. Humphrey, Direct calculation of the optical constants for a thin film using a midpoint envelope, Applied optics, 46 (2007) 4660-4666.

[167] D. Minkov, Calculation of the optical constants of a thin layer upon a transparent substrate from the reflection spectrum, Journal of Physics D: Applied Physics, 22 (1989) 1157.

[168] H. Anders, Thin Films in Optics Focal, London, 1967.

[169] S. Jena, R. Tokas, S. Tripathi, K. Rao, D. Udupa, S. Thakur, N. Sahoo, Influence of oxygen partial pressure on microstructure, optical properties, residual stress and laser induced damage threshold of amorphous HfO2 thin films, Journal of Alloys and Compounds, 771 (2019) 373-381.

[170] S. Jena, R. Tokas, S. Thakur, D. Udupa, Study of aging effects on optical properties and residual stress of HfO2 thin film, Optik, 185 (2019) 71-81.

[171] S. Jena, R. Tokas, J. Misal, K. Rao, D. Udupa, S. Thakur, N. Sahoo, Effect of O2/Ar gas flow ratio on the optical properties and mechanical stress of sputtered HfO2 thin films, Thin Solid Films, 592 (2015) 135-142.

[172] D. Malacara, Optical shop testing, John Wiley & Sons2007.

[173] A.K. Rumaiz, B. Ali, A. Ceylan, M. Boggs, T. Beebe, S.I. Shah, Experimental studies on vacancy induced ferromagnetism in undoped TiO2, Solid State Communications, 144 (2007) 334-338.

[174] C. Lu, Y. Fu, J. Jia, G. Yi, E. Xie, H. Guo, Effect of substrate temperatures on the properties of PLD Mo–V–Ag–O nanocomposite thin films, Vacuum, 167 (2019) 357-363.

[175] Z. Lei, J.-s. Lian, Effect of substrate temperature on structural properties and photocatalytic activity of TiO2 thin films, Transactions of Nonferrous metals society of China, 17 (2007) 772-776.

[176] H.-U. Krebs, M. Weisheit, J. Faupel, E. Süske, T. Scharf, C. Fuhse, M. Störmer, K. Sturm, M. Seibt, H. Kijewski, Pulsed laser deposition (PLD)--a versatile thin film technique, Advances in Solid State Physics, Springer2003, pp. 505-518.

[177] S.-i. Aoqui, H. Miyata, T. Ohshima, T. Ikegami, K. Ebihara, Preparation of boron carbide thin film by pulsed KrF excimer laser deposition process, Thin Solid Films, 407 (2002) 126-131.

[178] G.J. Rijnders, G. Koster, D.H. Blank, H. Rogalla, In-situ growth monitoring during PLD of oxides using RHEED at high oxygen pressure, Materials Science and Engineering: B, 56 (1998) 223-227.

[179] S. Bull, Failure mode maps in the thin film scratch adhesion test, Tribology international, 30 (1997) 491-498.

[180] S. Bull, Failure modes in scratch adhesion testing, Surface and Coatings Technology, 50 (1991) 25-32.

[181] H. Weiss, Adhesion of advanced overlay coatings: mechanisms and quantitative assessment, Surface and Coatings Technology, 71 (1995) 201-207.

[182] Y. Hamedani, P. Macha, T.J. Bunning, R.R. Naik, M.C. Vasudev, Plasma-Enhanced Chemical Vapor Deposition: Where we are and the Outlook for the Future, InTech2016.

[183] J. Gottmann, E. Kreutz, Pulsed laser deposition of alumina and zirconia thin films on polymers and glass as optical and protective coatings, Surface and Coatings technology, 116 (1999) 1189-1194.

[184] S. Dole, O. Hunter Jr, C. Wooge, Elastic properties of monoclinic hafnium oxide at room temperature, Journal of the American Ceramic Society, 60 (1977) 488-490.

[185] Q.-L. Xiao, C. Xu, S.-Y. Shao, J.-D. Shao, Z.-X. Fan, Y2O3 stabilized ZrO2 thin films deposited by electron-beam evaporation: Optical properties, structure and residual stresses, Vacuum, 83 (2008) 366-371.

[186] R. Hoffman, Stresses in thin films: The relevance of grain boundaries and impurities, Thin Solid Films, 34 (1976) 185-190.

[187] G. Abadias, E. Chason, J. Keckes, M. Sebastiani, G.B. Thompson, E. Barthel, G.L. Doll, C.E. Murray, C.H. Stoessel, L. Martinu, Stress in thin films and coatings: Current status, challenges, and prospects, Journal of Vacuum Science & Technology A: Vacuum, Surfaces, and Films, 36 (2018) 020801.

[188] E. Chason, B. Sheldon, L. Freund, J. Floro, S. Hearne, Origin of compressive residual stress in polycrystalline thin films, Physical Review Letters, 88 (2002) 156103.

Reviewers' Comments and Responses:

Title: "Investigation of effect of deposition parameters on composition, structure, and properties of plasma deposited boron carbide thin films."

Name of the Student: Arundhati Bute

Enrolment Number: PHYS 01201504007

Discipline: Physical Sciences

CI: Bhabha Atomic Research Centre

We sincerely thank both the reviewers for their critical review of this thesis. We appreciate their time and sincere efforts to provide us with valuable and constructive comments and questions that have added more clarity to the presentation of our experimental results. We have addressed all the queries in our response.

Comments and Replies to Reviewer #1

1. **Query/Comment**: Did you get perfectly stoichiometric B4C films for these investigations?

Reply: The compositional analysis of our boron carbide (B_xC) thin films revealed that there is an admixture of different stoichiometric phases of boron carbide (B_xC) in the films, including B_4C. In few of these samples, some of the boron carbide phases were found to be super stoichiometric with $x > 4$, with x as high as 9.6 and some of them was sub-stoichiometric, having $x < 4$, with x reaching as low as 1. The occurrence of this multi phased thin film happened due to the very nature of the deposition mechanism in PECVD process. For our boron carbide thin film deposition, ortho-carborane was used as the precursor. When vaporized precursor reached the highly energetic plasma environment, the precursor molecules disintegrated to form various radicals and molecular fragments. These precursor fragments, upon reaching the substrate surface underwent chemical reaction, and eventually formed the thin films. In PECVD process, it is almost impossible to control these micro level chemical reactions up to the extent to ensure that the entire film will be of B_4C stoichiometry. However, controlling the deposition parameters like, partial pressure of the process gases and the substrate self-bias, we can ensure that the major phase content present in the sample will be B_5C, B_4C or some other phase as desired.

2. **Query/Comment**: As regards to environmental stability of these films what are your final recommendation?

Reply: The films were found to be stable under ambient exposure for upto 12 months on silicon substrates. Therefore, for practical applications, these films need to be periodically checked every 6-8 months.

3. **Query/Comment**: What was the obtained efficiency of neutron detection?

Reply: Neutron detection efficiency of the thin films was not measured. However a typical thin film of thickness 3.5 μm thickness showed neutron absorption of 11.54% upon neutron transmission measurement experiment.

4. **Query/Comment**: How will you enhance the efficiency of the neutron detection using these boron-carbon thin films?

Reply: There are multiple ways by which the efficiency of these boron-carbon films can be enhanced:

   a. Using ^{10}B rich precursor can increase the efficiency of the deposited thin films.

   b. If these films are being used as neutron converter layers in gas filled proportional counters, multi plate geometry can be used to significantly enhance the neutron detection efficiency.

   c. If being used as solid state neutron detector, a trench like structure of geometry can significantly enhance the detector efficacy.

   d. During thin film deposition by PECVD, the deposition parameters have to be chosen such that boron rich phases get deposited.

5. **Query/Comment**: What approach you will take to enhance the efficiency of neutron detection?

   Reply: As stated before, the methods by which the efficiency of the boron-carbon thin films can be increased are:

   a. Use of ^{10}B enriched precursor.

   b. Considering multi plate proportional counter geometry for the films to can be used to significantly enhance the neutron detection efficiency.

c. If being used as solid state neutron detector, a trench like structure of geometry can significantly enhance the detector efficacy as that will potentially increase the active vilume.

d. The deposition parameters can be fixed such that boron rich phases get deposited.

6. **Query/Comment**: Can you use these films as p-n junction diode based detectors for radiations/ neutron/ charged particles?

   Reply: Yes. Since the deposited films are inherently is p-type in nature, if we deposit them over an n-type substrate, they can form a p-n junction. Efforts needs to be made to formation of proper junction after studying junction characteristics, otherwise it will be only a p-type material, deposited over an n-type substrate.

7. **Query/Comment**: What will be the advantage/ disadvantage in using p-n junction based detector as compared to the planer detector?

   Reply: The p-n junction based detector has been reported to have higher neutron detection efficiency as compared to the planer detector.

8. **Query/Comment**: For large area deposition applications, what modifications are required in your experimental system?

   Reply: For large area deposition applications, the size of the substrate holder in the PECVD chamber should be increased accordingly. Additionally, the substrate heater should be designed in such a way that it provides uniform heating over the entire area of the substrates. This is important as the substrate temperature plays an important role in determining the stoichiometry as well as ensuring improved adhesion of the thin film with the substrate. Therefore in addition to increasing the size of the substrate holder, the design of the heating arrangement should be kept under consideration. Since the increased substrate heater size will impart significant heat load to the deposition chamber walls, arrangements needs to be made for proper cooling of the chamber walls. Additionally the design of the precursor shower ring has to be modified to ensure uniform distribution of the vapour phase precursors.

Comments and Replies to Reviewer #2

1. **Query/Comment**: In his 4th publication, Arundhati Bute explores the influence of different deposition processes on the microstructure of the coatings. Chapter 6 deals with the publication "Boron carbide thin films deposited by RF-PECVD and PLD technique: comparison of structure, optical properties, and residual stress." Unfortunately, the question, why coatings in the system B-C-(O) are nanocrystalline using RF-CVD, and amorphous using PLD, could not be answered satisfactorily.

   Reply: In our work reported in chapter 6, the boron carbide thin films were deposited at same substrate temperatures i.e. 400°C in both PECVD and PLD technique. The substrate temperature was kept same in both the cases to eliminate the effect of substrate temperature on the structure of the films. The most prominent difference in the films deposited by the two techniques in that, the PECVD deposited films have certain amount of hydrogen in them, originating from the precursor, o-carborane ($C_2B_{10}H_{12}$), whereas, the PLD deposited film does not contain any hydrogen. It has been reported earlier that atomic hydrogen significantly affects thin film growth kinetics [i] and enhances the formation of microcrystalline phases of boron carbide [ii]. During thin film deposition, when the atomic hydrogen diffuses through the layers of the films, it leaves a vacant location. This hydrogen diffusion allows various atoms in the thin films to arrange themselves in positions of minimum Gibb's energy and form bonds with bond lengths closer to the equilibrium bond length of the crystal structure [iii].

   This might be the reason that the boron carbide thin films deposited by PECVD technique are nanocrystalline, and amorphous using PLD, at the same substrate temperature.

2. **Query/Comment:** All layers have a very high oxygen content, which is due to the high bases pressure. This could have been prevented either by longer pumping times or by a cold trap with liquid nitrogen. Instead of describing the coatings as boron carbide coatings with oxygen impurities, it is better describe the film as coatings in the B-C-O system, because the oxygen content is often in the same order of magnitude as the carbon content.

Reply: We agree with the reviewer for the fact that the films have very high oxygen content. As per his suggestion we would use cold trap with the help of liquid nitrogen for improvement of base pressure in our further experiments. Although the films contain a considerable amount of oxygen, it does not play a dominant role in determining the properties of the boron carbide thin films. For Example, the hardness of the deposited films is similar to that of boron carbide thin films, not boron oxide thin films. The optical bandgap and other film properties of the films also indicate the same. Hence in our opinion, it will be befitting to refer the films as ^{nat}boron carbide thin films.

References:

[i] R. Bao, D. B. Chrisey, D. J. Cherniak, Kinetics of hydrogen in preparing amorphous B_5C:H thin films, J. Mater. Res., 26(7) (2011).

[ii] S. Lee, J. Mazurowski, W. L. O'Brien, Q. Y. Dong, J. J. Jia, T. A. Callcott, Yexin Tan, K. E. Miyano, D. L.Ederer, D. R. Mueller, and P. A. Dowben, The structural homogeneity of boroncarbide thin films fabricated usingplasma-enhanced chemical vapordeposition from B_5H_9+CH_4, J. Appl. Phys. 74, 6919 (1993).

[iii] Mayur S. Valipa**,** Hydrogen-induced crystallization of amorphous Si thin films. II. Mechanisms and energetics of hydrogen insertion into Si–Si bonds**,** Journal of Applied Physics 100 (4), 053514 (2006).